Magnetic tunneling junctions with the Heusler compound $Co_2Cr_{0.6}Fe_{0.4}Al$

Dissertation
zur Erlangung des Grades
Doktor der Naturwissenschaften (Dr. rer. nat.)
am Fachbereich Physik
der Johannes Gutenberg-Universität Mainz

von
Andrés Conca Parra
geboren in Biar, Alicante, Spanien

Mainz, 2007

Tag der mündliche Prüfung: 20.07.2007

Keep an open mind, but no so open that your brain falls out.
Richard P. Feynman

Contents

1 Theoretical background of TMR **5**

1.1 Interfaces and barrier influence 5

1.1.1 Diffusive and coherent regime 5

1.1.2 Relation between SP of the tunneling current and SP of electrodes. Validity of Jullière model 7

1.1.3 Interfaces 9

1.2 Spectroscopy 10

1.3 Applications of magnetic tunneling junctions. 11

2 Half metallic Heusler compounds **17**

2.1 General considerations 17

2.1.1 Origin of the gap in heusler alloys 18

2.2 Co_2CrAl and $Co_2Cr_{0.6}Fe_{0.4}Al$ 20

2.2.1 Disorder effects 21

2.2.2 Spin-orbit interaction and SP 22

2.2.3 Is the surface/interface also half-metallic? 23

2.2.4 Temperature dependence of the SP in half-metals 24

3 Preparation of the samples **27**

3.1 Deposition system 27

3.2 Deposition of the samples 28

3.2.1 Substrates preparation 28

3.2.2 Cr and Fe buffer layer deposition 29

3.2.3 $Co_2Cr_{0.6}Fe_{0.4}Al$ and MTJ's deposition 30

3.3 Preparation of mesa structures 33

3.3.1 Etching angle dependence 37

4 CCFA thin films **39**
4.1 Crystallographic properties 39
4.1.1 General considerations 39
4.1.2 Polycrystalline samples 40
4.1.3 Epitaxial films with buffer layer 43
4.1.4 Epitaxial films without buffer layer 49
4.1.5 Estimation of the degree of disorder 54
4.2 Magnetic properties 57
4.2.1 Polycrystalline samples 57
4.2.2 Epitaxial samples 58
4.2.3 XMCD and XAS results 61
4.3 Transport properties 63
4.4 Surface ordering and topology 65

5 Magnetic tunneling junctions **75**
5.1 Exchange bias 75
5.2 TMR of polycrystalline samples 78
5.3 TMR in epitaxial samples 81
5.3.1 Annealing temperature dependence 81
5.3.2 Correlation between surface order and topology and TMR 84
5.3.3 Surface tailoring 86
5.3.4 Oxidation time dependence 88
5.3.5 TEM 89

6 Tunneling spectroscopy **91**
6.1 Measurements of the differential conductivity 92
6.2 Interpretation of the dI/dV (V_{BIAS}) and 101
6.2.1 Zero bias anomaly 101
6.2.2 Change in the TMR sign 103
6.2.3 Additional structures 106
6.3 IET measurements 110

A **121**
A.1 Patterning of mesa structures 121
A.2 Sputtering and oxidation parameters 123

Bibliography **125**

List of Figures

1.1 Calculations of the $k_{\parallel}$-dependent conductance of the minority channel of MTJ's with ordered ZnSe barrier 6

1.2 Calculations of the $k_{\parallel}$-dependent conductance of the minority channel of MTJ's with ordered ZnSe barrier 8

1.3 Simple model of a tunneling barrier 10

1.4 Simple scheme of a MRAM array. 12

1.5 Realization of a AND and a OR gate with a MTJ. 14

2.1 $L2_1$ structure. 18

2.2 DOS of Co_2CrAl. 19

2.3 Calculation of the band structure for Co_2CrAl (from [58]) 20

2.4 SP of Co_2CrAl versus Fe content. 21

2.5 Calculation of the band structure for $Co_2Cr_{0.6}Fe_{0.4}Al$ 23

3.1 Deposition system. 28

3.2 Exchange biased Co film. 31

3.3 Structure of a MTJ stack. 33

3.4 Realization of a mesa structure. 34

3.5 Picture of a mesa structure with a diameter of 200 μm. 36

3.6 Resistance versus temperature for two mesa structures etched perpendicular and with an angle of 70 ^{o} respect to the normal to the film surface. 37

4.1 PowderCell simulation of a $\theta/2\theta$ scan with the Bragg-Bentano geometry for the different kinds of possible structures of $Co_2Cr_{0.6}Fe_{0.4}Al$ 40

4.2 Top: TEM image of a polycrystalline sample deposited on Al_2O_3 at room temperature. The circles mark crystallites with different crystalline orientation. Bottom: Electron diffraction pattern of the same sample. Reflections corresponding to the B2 structure can be identified. Both figures are courtesy of Christian Herbort. . . . 41

4.3 Schematic representation of the epitaxial relationship of a CCFA thin film on an Fe or Cr buffer layer on a MgO (100) substrate. . 43

4.4 $\theta/2\theta$ scan and rocking curve of the (400) reflection of a 100 nm thick CCFA film deposited at 100 °C on a 50 Å thick Cr buffer layer on a MgO (100) substrate. 44

4.5 $\theta/2\theta$ scan and rocking curve of the (400) reflection of a 100 nm thick CCFA film deposited at 100 °C on a 100 Å thick Fe buffer layer on a MgO (100) substrate. 45

4.6 X-ray ϕ-scan of the (220) equivalent reflections of a CCFA film deposited at 100 °C (filled symbols) and of the MgO substrate (open symbols, peaks labeled in italics). A Fe buffer layer was used in this sample. 47

4.7 X-ray ϕ-scan of the (220) equivalent reflections of a CCFA film deposited at 100 °C (filled symbols) and of the MgO substrate (open symbols, peaks labeled in italics). A Fe buffer layer was used in this sample. 48

4.8 $\theta/2\theta$ scan and rocking curve of a 100 nm thick CCFA film deposited at 100 °C on a $MgAl_2O_4$ (100) substrate and annealed at 600 °C . 50

4.9 $\theta/2\theta$ scan and rocking curve of a 100 nm thick CCFA film deposited at 100 °C on an Al_2O_3 $(11\bar{2}0)$ substrate and annealed at 600 °C . . 51

4.10 Schematic representation of the epitaxial relation between CCFA and Al_2O_3 $(11\bar{2}0)$ substrates. 53

4.11 Schematic explanation of the origin of geometrical effects in measured scattering intensities in thin film diffraction experiments. . . 55

4.12 Hysteresis loops at 300 and 4 K of a polycrystalline $Co_2Cr_{0.6}Fe_{0.4}Al$ thin film deposited on Al_2O_3 at 300 °C and annealed at 450 °C for 60min. The thickness of the film is 100 nm. 57

4.13 Top: Hysteresis curves at 300 and 4 K of a 100 nm thick CCFA sample deposited at 100 °C on Fe buffer layer on MgO (100) without annealing. Bottom: Dependence of the magnetization at 20 mT on the temperature. The grey line is a fit with a power law with $\beta = 1.72$ (see text). 59

4.14 $\theta/2\theta$ scan and rocking curve of the (400) reflection of a 100 nm thick CCFA film deposited at 100 °C on a 50 Å thick Cr buffer layer on a MgO (100) substrate. 60

4.15 Resistance versus temperature measured for a $Co_2Cr_{0.6}Fe_{0.4}Al$ thin film with a thickness of 100 nm deposited on a $MgAl_2O_4$ (100) substrate. 63

4.16 Specific resistivity at 4 K versus magnetic field measured for a $Co_2Cr_{0.6}Fe_{0.4}Al$ thin film with a thickness of 100 nm deposited on a $MgAl_2O_4$ (100) substrate. 64

4.17 Schematic representation of a RHEED experiment. For a 2D lattice, the reciprocal lattice degenerates in infinite rods perpendicular to the film surface (black lines). The sphere represents the Ewald sphere. The projection of the intersection of the Ewald sphere with the infinite rods on the phosphorescent screen gives the RHEED pattern (yellow points in the green screen). 66

4.18 Top: RHEED diffraction pattern for an as-deposited $Co_2Cr_{0.6}Fe_{0.4}Al$ thin film on a 100 nm thick Fe buffer layer. Bottom: RHEED pattern from a similar sample after annealing at 550 °C for 5 min. . . 67

4.19 Top: RHEED pattern of a CCFA thin film deposited on a $MgAl_2O_4$ (100) substrate at 100 °C and annealed at 600 °C. Bottom: RHEED pattern of a CCFA thin film deposited on an Al_2O_3 $(11\bar{2}0)$ substrate and annealed at 600 °C. 68

4.20 LEED diffraction pattern for a $Co_2Cr_{0.6}Fe_{0.4}Al$ film deposited on Fe buffer layer and annealed at 550 °C for 5 min. 70

4.21 STM images of 100 nm thin $Co_2Cr_{0.6}Fe_{0.4}Al$ films deposited at 100 °C (top) and 400 °C (bottom) on Fe buffer layer on a MgO (100) substrate. 71

4.22 STM image of 100 nm thin $Co_2Cr_{0.6}Fe_{0.4}Al$ film deposited at 550 °C on Fe buffer layer on a MgO (100) substrate. 72

4.23 STM images of 100 nm thin $Co_2Cr_{0.6}Fe_{0.4}Al$ films deposited at 100 °C on Fe buffer layer on a MgO (100) substrate and annealed at 550 °C (top) and 600 °C (bottom). 73

5.1 Top: Hysteresis curve at 4 K of a CCFA/AlO_x/Co multilayer sample. Bottom: Hysteresis curve at 4 K of a CCFA/AlO_x/Co/CoO multilayer sample. 76
5.2 Major magnetoresistance loops for a MTJ pinned with 10 nm of FeMn (top) and CoO formed by oxidation of the previously deposited Co electrode (bottom). 77
5.3 Minor loop magnetoresistance curve of a CCFA/AlO_x/Co/CoO polycrystalline sample. 78
5.4 Dependence of the TMR ratio on the Al thickness for polycrystalline samples. 80
5.5 Dependence of the TMR ratio on the annealing temperature for samples deposited on Fe buffer layer on MgO(100) substrates. . . 82
5.6 Maximal measured TMR ratio at 4 K of a MTJ with epitaxial $Co_2Cr_{0.6}Fe_{0.4}Al$ electrode deposited on Fe buffer layer on MgO (100) and annealed at 550 °C for 5 min. 83
5.7 RHEED diffraction patterns of samples annealed at different temperatures. All the samples were deposited on Fe buffer layers and annealed for 5 min. 85
5.8 Dependence of the TMR ratio on the thickness of the Cr tailoring layer deposited on the $Co_2Cr_{0.6}Fe_{0.4}Al$ film. 87
5.9 Dependence of the TMR ratio on the oxidation time for samples deposited on Fe buffer layer and annealed at 550 °C for 5 min. . . 88
5.10 Top: TEM image of a Fe/CCFA/AlO_x/Co/CoO MTJ deposited on MgO. Clearly it is observed that the barrier is smooth and defect-free on large scales. Bottom: Detail of a tunneling barrier. Both figures are courtesy of Christian Herbort. 90

6.1 Schematic representation of the experimental setup used to measure the differential conductivity dI/dV. 92
6.2 Differential conductivity dI/dV versus bias voltage for a non-annealed Fe/CCFA/AlO_x/Co/CoO/Pt sample measured at room temperature(top) and 4 K (bottom). 93

6.3 Schematic representation of the potential barrier of a tunneling junction. 95
6.4 Differential conductivity dI/dV versus bias voltage for annealed Fe/CCFA/AlO_x/Co/CoO/Pt samples measured at 4 K. The red line represents a fit using Brinkman's model. The inset shows a comparison between the measurements by the antiparallel and parallel configuration. 96
6.5 TMR dependence on the bias voltage for as deposited (top) and annealed (bottom) Fe/CCFA/AlO_x/Co/CoO/Pt samples measured at 4 K. For negative voltages the electrons tunnel into CCFA. . . . 98
6.6 TMR measured at 4 K and with 920 mV bias voltage for the same sample of as the bottom panel of fig. 6.5. 99
6.7 Predicted bias voltage values for a sign change in the spin polarisation of the alloy $Co_2Cr_{1-x}Fe_xAl$, for different Fe doping concentrations X. Top (bottom) panel shows the case for the occupied (empty) DOS. The plotted values are from band structure calculation by G. Fecher [142]. 104
6.8 Measurements from [144] of the differential conductivity G=dI/dV (left) and of the TMR(V_{BIAS}) (right) for Co/Al_2O_3/Co junctions with Cu dusting layers. The control Cu-free junctions are also shown. 106
6.9 Differential conductivity (dI/dV) measurements for a sample series with varying oxidation times. The data is normalized to the value of dI/dV at zero bias. The $Co_2Cr_{0.6}Fe_{0.4}Al$ electrode was annealed at 550 °C for 5 min. The nominal barrier thickness is 3 nm and the oxidation took place in an Ar-O_2 mixture. 107
6.10 Estimated spin polarisation for $Co_2Cr_{1-x}Fe_xAl$ for the cases X=1/2 and X=1/4 from calculations by Fecher [142]. 109
6.11 IET spectra measured at 4 K for a Fe/$Co_2Cr_{0.6}Fe_{0.4}Al$/Al_2O_3/Co junction. The $Co_2Cr_{0.6}Fe_{0.4}Al$ electrode was annealed at 550 °C for 5 min. The nominal barrier thickness is 3 nm and the oxidation took place in an Ar-O_2 mixture. The sharp peaks at 16 mV are due to inelastic electron-magnon scattering processes during the tunneling process. The structure at ∼220 mV (solid arrow) is related to the Co counter electrode feature observed in the dI/dV measurements. An additional overlapping structure (dashed arrow) is also observed. 110

6.12 Top: Comparison of the IET spectra for the parallel and the antiparallel magnetization configuration. Bottom: IET spectra for the same junction measured at different temperatures. The broadening and the voltage shift of the peaks at low voltages are due to thermal smearing and to an increase of the low energy wavelength cutoff for magnons with increasing temperature. The structure at ∼220 mV is only modified by thermal smearing. For comparison, the different curves are normalized to the value at +500 mV. The nominal barrier thickness is 3 nm. 112
6.13 Subtraction of the negative bias voltage side from the positive bias voltage side of the IET spectra for different temperatures. The overlapping structure observed in the IET spectra (fig. 6.11) is now visible as a peak centered at ∼85 mV. This peak is tentatively identified as a phonon generated at the interface barrier/electrode (see text for explanation). The $Co_2Cr_{0.6}Fe_{0.4}Al$ electrode was annealed at 550 °C for 5 min. The nominal barrier thickness is 3 nm. The TMR ratio for this sample is 40.2%. 114
6.14 Difference of the negative bias voltage side from the positive bias voltage side of the IET spectra at 4 K for samples with different oxidation times. The dashed line is a guide to the eye and indicates $V_{BIAS} = 85$ mV. The increased noise level is a consequence of the non-direct measurement of d^2I/dV^2. The peak position shifts slightly toward lower voltages with increasing oxidation times. For oxidation times of 90 s this tendency can not be confirmed due to the small size of the peak. The $Co_2Cr_{0.6}Fe_{0.4}Al$ electrode was annealed at 550 °C for 5 min. The nominal barrier thickness is 2 nm. 115

List of Tables

1.1 Comparison beetween memories. 13

3.1 Comparison between FeMn and CoO exchange bias properties. . . 32

4.1 Lattice constants and misfits (in absolute value) between the different materials of interest for this work. 42

4.2 Survey of results for the estimation of the Co-Cr degree of disorder and the coherence length L for different kinds of CCFA samples. . 56

Introduction

In 1983, De Groot *et al.* [1] predicted the existence of a new kind of materials. The band structure calculations performed by De Groot *et al.* for the Heusler alloy NiMnSb showed a new and interesting feature. In the density of states for this compound, a gap at E_F for the minority electrons is observed. NiMnSb behaves as a metal for one spin direction while for the other it is a semiconductor. This new kind of materials received the name *half metals*.

This discovery triggered a major research effort in order to understand the properties of the half metals and confirm the theoretical predictions experimentally. Later on, half metallic character was predicted for a large number of systems such as many other Heusler compounds as for instance Co_2CrAl [56, 58] or Co_2MnSi [53], some oxides like CrO_2 [2] and some double Perovskites like Sr_2FeMoO_6 [3].

As a direct consequence of the electronic structure at the Fermi level, a current flowing in a half metallic material is fully spin polarised. This property is of enormous interest in the fast developing field of spintronics[1]. In spintronic devices such as spin valves, widely used nowadays as read heads for hard disks or in general as magnetic sensors, the size of the magnetoresistive effect increases with the spin polarisation of the current.

An alternative kind of spintronic devices are magnetic tunneling junctions (MTJ's). A MTJ consists basically in two ferromagnetic films acting as electrodes separated by a thin insulating barrier layer with typical thicknesses of a few nanometers. The barrier material is typically an oxide. A tunnel current can flow through the device resulting in a huge magnetoresistive effect depending on the relative orientation of the magnetization of the ferromagnetic electrodes. This effect, called tunneling magnetoresistance (TMR), increases with the spin polarisation of the tunneling current as well. In the simple model of Jullière,

[1] Also called spinelectronics or magnetoelectronics.

the magnitude of the TMR effect is directly related to the spin polarisation of the ferromagnetic electrodes. Though the pioneering experiments of Jullière were already reported in the 1970's, the lack of reliability and reproducibility in the preparation of MTJ's stacks with conventional ferromagnetic electrodes like CoFe slowed the development in this field until the 1990's. New deposition techniques evolved allowing the until today constant increase of the TMR ratios with the time.

Nowadays, the size of the magnetoresistive effect in MTJ's is one or two orders of magnitude larger than for spin valves. For this reason, TMR elements have been postulated as a successor of spin valves. However, the larger resistance values for MTJ's stacks compared to spin valves has limited its introduction in the field of hard disk read heads due to incompatibilities with the current technology. Nevertheless, the recent introduction of the first TMR-based read heads indicate that these problems have been solved [29, 30].

Notwithstanding with the previous considerations, an alternative and even more promising application possibility for MTJ's is feasible. Systems consisting of arrays of TMR elements can be used as recording media. These systems form non-volatile magnetic RAM memories (MRAM). With write/read speeds comparable (or better) to some of the currently used RAM memories and with lower power consumption ans non-volatility, this technology is very promising and created great research and development efforts in industry.

For all these potential applications to become true, a large TMR ratio is required for a single MTJ elements. Therefore, the scientific and industrial interest in materials with high spin polarisation and specifically in half-metals is justified.

This work is focused on the study of the properties of thin films of the theoretically predicted half metal $Co_2Cr_{0.6}Fe_{0.4}Al$ and their implementation in tunneling junctions. Amorphous Al_2O_3 is used as a barrier material of all the junctions in this thesis. Recently, higher TMR ratios with ordered MgO barrier have been achieved in MTJ's with conventional [11, 12, 13, 14] and half metallic electrodes [15, 16]. However, due to the presence of coherent tunneling effects in ordered barriers, the TMR values can not be correlated to the spin polarisation of the electrodes. Therefore, MgO barriers can not be used to prove high spin polarisation of the electrodes.

The effect of the different substrates and metallic buffer layers on the crystalline and magnetic properties of the films is discussed. The influence of different deposition parameters such as substrate, annealing conditions, barrier thickness

and oxidation time are discussed as well.

Tunneling is very sensitive to the interfaces electrode/barrier. Therefore the surface crystalline quality of the films and its morphology play a crucial role for the measured TMR. In consequence, the surface crystalline properties were studied with Reflection High Energy Electron Diffraction (RHEED) and Low Energy Diffraction (LEED) systems and the surface topology was measured with in-situ scanning tunneling microscopy (STM). Correlations between the surface properties and TMR ratios are discussed.

Chapter 1 gives a theoretical introduction in the various phenomena presented in tunneling junctions with emphasis on the differences between ordered and amorphous barriers and the role of the interfaces. Potential applications of MTJ's are discussed as well.

Chapter 2 is a short introduction to the physical origin of the half metallic gap in Heusler alloys. The effect of the different kinds of atomic disorder in $Co_2Cr_{0.6}Fe_{0.4}Al$ on the spin polarisation are considered. A discussion about possible influences of the surface on the half metallic character is conducted.

Chapter 3 describes the deposition system and techniques as well as patterning of tunnel structures (MESAs).

Chapter 4 shows the results concerning the crystalline, magnetic and transport properties of the $Co_2Cr_{0.6}Fe_{0.4}Al$ films with a section corresponding to the surface properties.

In Chapter 5 the results concerning TMR ratios of MTJ's are presented and correlations between surface properties and TMR are discussed.

Chapter 6 present the spectroscopic measurements performed on the junctions of this work and their interpretation.

Chapter 1

Theoretical background of the tunneling magnetoresistance

A magnetic tunneling junction (MTJ) consists in two ferromagnetic thin films separated by a thin (∼1-3 nm) insulating barrier, typically an oxide. Due to the tunnel effect, a current can flow from one ferromagnet (FM) to the other if a voltage is applied. The measured resistance of the junction depends on the relative orientation of the magnetization of the electrodes as first observed by Jullière [4]. The change of the resistance depends on the spin polarisation (SP) of the tunneling current. In this chapter, the relation between the SP of the tunneling current and the SP of the ferromagnetic electrodes is discussed.

1.1 Interfaces and barrier influence

1.1.1 Diffusive and coherent regime

In order to describe the behavior of a MTJ, the crystalline order of the barrier is of major importance. Nowadays, Al_2O_3 and MgO are the most often used barrier materials. Al_2O_3 barriers are always amorphous while with MgO it is possible to deposit singlecrystalline barriers. In both cases the electronic states of the electrodes are able to penetrate into the barrier as evanescent states, the so-called metal induced gap states (MIGS's). The wave vector of the MIGS's has a complex part and they build complex bands in the insulator [5, 6]. We can separate the wave vector in two parts, $k_{\|}$ includes the components k_x and k_y parallel to the FM/barrier interface, k_z is the component perpendicular or transversal. The $k_{\|}$

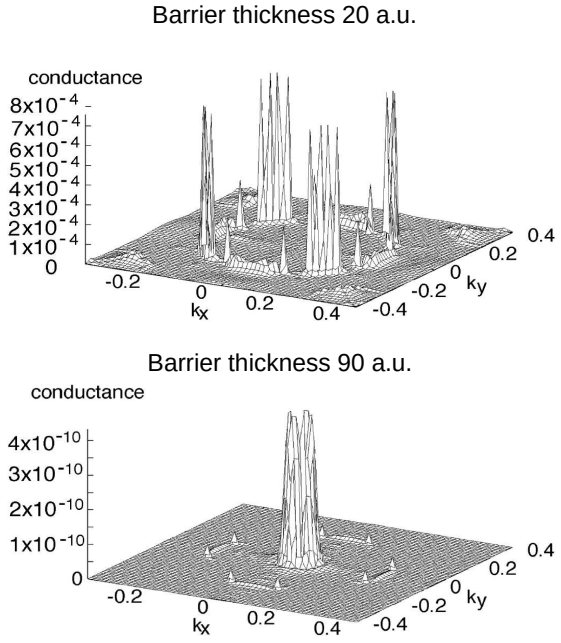

Figure 1.1: Calculations from [8] of the $k_{\|}$-dependent conductance of the minority channel of two MTJ's with ordered ZnSe barrier with different thicknesses. Here, only the results for the parallel configuration are shown.

components are real numbers while k_z is a complex number, thus k_z=q+iκ where κ is the attenuation length of the evanescent wave in the barrier. In the case of a perfectly ordered barrier and smooth interface we can assume that $k_{\|}$ is conserved by tunneling (specular approximation). It is clear that the MIGS's with a larger κ decay faster in the barrier regions and the tunneling current is dominated by a few states with the smallest κ and energies near E_F. In the limit of very thick barriers only the state with the smallest decay parameter κ_{min} contributes to the tunneling current.

Intuitively, the states with the smallest decay parameters should be the ones around $k_{\|}$=0. However, symmetry matching considerations between the electronic bands of the electrodes and of the electrodes and the complex bands in the insulator result in new effects. One of them is the formation of resonant interface states or hot spots [7, 8, 9], for certain $k_{\|}$ values different than zero there is a very small attenuation. These hot spots appear mainly in the minority channel and dominate the conductance in this channel for all intermediate thicknesses. The upper plot in fig. 1.1 show the presence of resonant states as peaks in the $k_{\|}$-dependent conductance . Only at the limit of very large barrier thickness

the conductance for large $k_{\parallel}$ is suppressed and only the values near $k_{\parallel}$=0 are important, as shown in the bottom plot in fig. 1.1.

All the previous considerations show that a detailed knowledge of $\kappa(k_{\parallel})$, i.e. band structure at the interface, is necessary to understand MTJ's with epitaxial barriers. In the case of amorphous barriers like Al_2O_3 , the presence of disorder at the boundary electrode/barrier generates a diffusive scattering that mixes all the incoming electronic states with the same energy. Details in the conductance plots as seen in fig. 1.1 are blurred out. It must be pointed out that this diffusive elastic scattering keeps the total density of states invariant since this is a property summed over states in some energy interval dE. Scattering processes leading to energy changes or spin flips are not included in these considerations.

1.1.2 Relation between SP of the tunneling current and SP of electrodes. Validity of Jullière model

Following the Jullière model [4], the TMR ratio is related to the spin polarisation of the electrodes, P_n. In the optimistic definition:

$$TMR = \frac{\Delta R}{R_P} = \frac{2P_1P_2}{1 - P_1P_2} \tag{1.1}$$

The model assumes that the spin is conserved during the tunneling process and that the tunneling probability is proportional to the density of states of the electrodes. The barrier is treated only as a passive element with no influence in the SP of the tunneling current. In this model, the SP of the tunneling current is directly related to the SP of the electrodes.

The Jullière model is not able to explain certain properties of the MTJ's such as the temperature and bias voltage dependence of the TMR ratio but it is widely used to correlate measured TMR ratios with spin polarisation. All junctions with Al_2O_3 barrier provide consistent Jullière values for the SP. Furthermore the values of the SP provided by the model are in concordance with the SP measurements using ferromagnet/insulator/superconductor tunneling junctions (Meservey-Tedrow contacts). Theoretical support for the validity of the model was given by Tsymbal and Pettifor [10], who made calculations for very disordered barriers which show that the TMR is in agreement with Jullière's formula.

For epitaxial smooth barriers, other kinds of consideration are necessary. In the last few years, very high TMR ratios have been reported for fully epitaxial MTJ's with MgO barriers using conventional ferromagnets. Values at

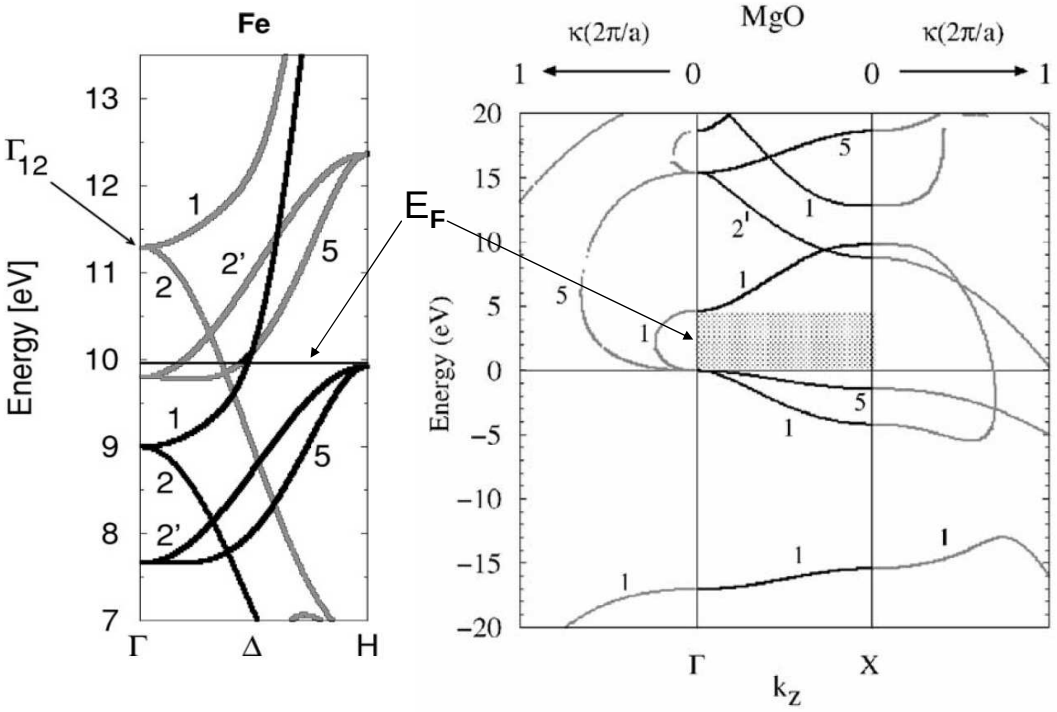

Figure 1.2: Left: Band structure of Fe from [17] along k_z. Black lines represent majority-spin bands and gray lines the minority ones. Right: Central panel shows the real bands for the insulator MgO, right and left panel show the E(κ) complex bands for Re(k_z)=0 and Re(k_z)=2π/a. Numbers represent the symmetries in the group of rotations around the (001)-Δ direction which is C_{4v} for Fe and C_{4h} for MgO.

room temperature as high as 180% for Fe/MgO/Fe [11, 12], 120 to 220% for CoFe/MgO/CoFe [13] or 230% for CoFeB/MgO/CoFeB [14] have been measured. The Jullière model applied to these systems produces very high SP values, for instance, for the CoFe/MgO/CoFe the concluded SP is 85%. This value does not correspond to the bulk DOS of CoFe, but to the effective SP of the tunneling current, i. e. to the SP of the states with high transmission probability.

To understand these high TMR values we have to go back to the description of the tunnel conductance in term of MIGS's and complex electronic bands. In the left plot of fig. 1.2 the band structure for Fe is shown [17]. On the left the the real and complex bands of MgO for $k_{\|}$=0 are shown [7]. The central panel of the right plot shows the real bands, the left and right panel show the complex bands for Re(k_z)=0 and Re(k_z)=2π/a, respectively. As it can be seen in this figure, in the complex band structure of MgO there are three bands that intersect the

Fermi level, with symmetries Δ_1, Δ_5 and $\Delta_{2'}$. It is clear that the band with smaller decay parameter κ is the small Δ_1 loop that connects both real bands above and below the gap[1]. This band has the lowest attenuation and dominates the tunneling current for thick barriers.

Let us now consider the band structure of Fe. The first case is the parallel alignment of the magnetization of both electrodes. The majority Δ_1 band of Fe couples with the complex Δ_1 band in MgO and matches the same band of the other electrode.. All the other possible majority states and the minority bands couple only with complex bands like Δ_5 which decay much faster.

If the magnetization of the second electrode is now reversed, the junction is in the antiparallel configuration. Now all the majority Δ_1 bandsof the first electrode face bands of incompatible symmetry $\Delta_{2'}$ and Δ_5 in the second one and the electrons are blocked in the second interface. The transmission probability in now much smaller than in the parallel alignment case. As a result, the conductivity is much smaller in the antiparallel configuration and the TMR ratio is increased.

Thus, the presence of a highly ordered barrier generates a *spin filtering* effect since only some electronic band are selected to take part in the tunneling process. The spin polarisation of the tunneling current in completely ordered systems does not reflect the total spin polarisation of the DOS of the ferromagnet. In order to measure the interface SP of a ferromagnetic material with a MTJ an amorphous barrier like Al_2O_3 is the only possible choice.

1.1.3 Interfaces

The first atomic layers adjacent to the barrier play a crucial role for the value of the TMR ratio of a MTJ. Already in 1975, first experiments of Meservey and Tedrow using ultrathin ferromagnetic electrodes showed that only a few atomic layers are needed to achieve a full SP [18]. Additional experiments introducing very thin dusting layers between the ferromagnet and the barrier have given further insight in the importance of the first layers at the interface. These experiments show that the TMR ratio falls exponentially with the thickness of the dusting layer for the first atomic layers. However, the decay for additional dust-

[1]The band structure plotted in fig. 1.2 is valid only for the $k_{\parallel}$=0 case. To see if this loop really corresponds to κ_{min} we have to scan all the other $k_{\parallel}$ vectors in order to prove if this is really the absolute minimum. For MgO barriers this is the case [7], but there is no reason to be the same in other materials.

ing layers with larger thickness is much slower [19, 20, 21]. Early calculations by Appelbaum and Brinkman [22] showed that the characteristic length of the exponential decay should be of the order of k_F^{-1} at the interface. This is in good agreement with some experimental observations [21, 23] but the decay may be faster in other systems.

All these tests confirm the importance of the first monolayers at the electrode/barrier interface. In this context, the adequate oxidation conditions of the barrier are of major significance. An overoxidation of the barrier may lead to the oxidation of the first atomic layers of the electrode resulting in a reduction of the TMR ratio. Additionally, the degree of crystallographic order of the last atomic layers has a great influence on the TMR and the use of surface sensitive analysis devices like RHEED or LEED are required.

1.2 Spectroscopy

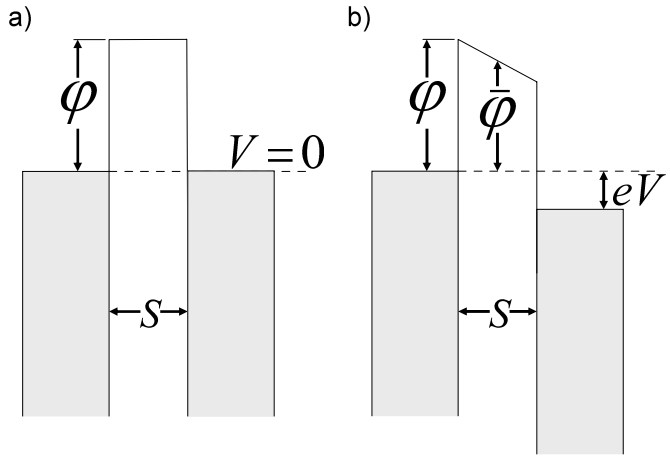

Figure 1.3: Simple model of a tunneling barrier. Left: No bias voltage applied. Right: A bias voltage V is applied. The Fermi energy is shifted by eV.

The resistance of a tunneling junction has a non ohmic behaviour. In general the I(V) curve has terms of second and third order in V. Commonly, the differential conductivity dI/dV is measured since the current lock-in technique allows a very sensitive and low-noise determination of this magnitude.

Simmons developed a model [24] to explain the $dI/dV(V_{bias})$ curve using a trapezoidal shape for the potential barrier. The model assumes a symmetric barrier as shown in fig. 1.3a. The current flowing from one electrode to the other

decreases exponentially with the barrier heigth φ. The total net current is the sum of two currents flowing in opposite directions. When a bias voltage is applied, the barrier potential is deformed (fig. 1.3b). By calculating the total current for a given bias voltage Simmons arrived to the following expression (see also [26]):

$$\frac{dI/dV(V)}{dI/dV(0)} = 1 + 3\gamma V^2 \tag{1.2}$$

where $\gamma \approx \frac{0.0115}{\bar{\varphi}} S^2$ when S and φ are given in Ångström and Volt, respectively.

Further considerations by Brinkman *et al.* [25] included the possibility of asymmetrical barriers. This is a most realistic description, especially when the barrier is formed by the oxidation of a previously deposited metallic film. Additionally, the presence of different electrodes on both sides of the barrier may also result in an asymmetrical shape of the barrier potential even for the case of a direct deposition of an oxide barrier.

The bias voltage dependence of the differential conductivity in the Brinkman's model takes the following form:

$$\frac{dI/dV(V)}{dI/dV(0)} = 1 - \left(\frac{A_0 \Delta\varphi}{16\varphi^{3/2}}\right) eV + \left(\frac{9\, A_0^2}{128\, \varphi}\right) (eV)^2 \tag{1.3}$$

with $A_0 = 4(2m)^{1/2} S/3\hbar$ and dI/dV(0)=$3.16 \cdot 10^{10}\, \frac{\bar{\varphi}^{1/2}}{S}\, exp(-1.025\, S\bar{\varphi}^{1/2})$. The value of the conductance for zero bias is the same as given in the Simmons model. The γ parameter of the Simmons model is related with A_0:

$$\gamma = \frac{3\, A_0^2}{128\, \varphi} \tag{1.4}$$

It is important to note that the parameters S and φ are related to the potential barrier and not to the width of the physical barrier. Both models are not valid for very high voltages (eV $> \bar{\varphi}$). Furthermore, the validity may be even more limited by heating effects due to the current generated at medium voltages already.

1.3 Applications of magnetic tunneling junctions.

One of the first conceived applications for MTJ's was as a substitution of the GMR sensors (spin valves) in read heads for hard discs. Unfortunately, the resistance of the junction and the capacitance of the read head combine to form a low-pass

filter, resulting in a limit for the reading rate. A low resistance surface product RS [2] is needed to avoid this problem. Additional noise considerations reduce the upper limit for RS to 4 $\Omega\mu m^2$. This low RS product must be achieved while keeping the TMR ratio over 20%. The obvious strategy of using ultrathin barriers to reduce the RS product may lead easily to an oxidation of the bottom electrode. Furthermore, the probability of defects in very thin barriers is very high which reduces reproducibility. Other techniques as two-step oxidation [27, 28] or new barrier materials with low band gap have been also studied.

In the last few years great progress concerning the reduction of the RS product while keeping a high TMR ratio was achieved. Kobayashi and Akimoto [29] from Fujitsu Laboratories reported recently TMR read heads with alumina barrier with a RS product of 4 $\Omega\mu m^2$ and a TMR ratio of 25% suitable for recording densities up to 100 Gbit/in^2 . With MgO barrier the read head TMR ratio achieves 40-50% for RS = 2-3 $\Omega\mu m^2$ for 200 Gbit/in^2 densities.

The development of TMR devices for HDD read heads applications has become mature enough to go to market. In 2005 first Seagate introduced a 400 Gb hard disc drives with a TMR read head device. They were followed by Samsung and Toshiba [30].

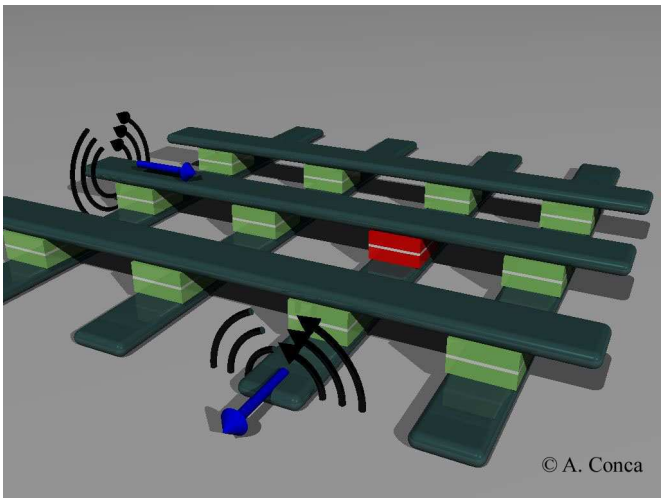

Figure 1.4: Simple scheme of a MRAM array. In order to write a bit in a certain MTJ (in red), currents (in blue) are sent through two different pads. The addition of the resulting magnetic fields rotates the free layer of the junction.

An alternative and also very promissory application of MTJ's is the con-

[2]Or resistance-area product RA.

Parameter	SRAM	DRAM	FLASH	MRAM
Cell Area	3.7 μm^2	0.56 μm^2	0.5 μm^2	0.7-1.4 μm^2
Read access	3.3 ns	13 ns	13 ns	5-20 ns
Write cycle	3.4 ns	20 ns	5 μs	5-20 ns
Data retention power	yes	yes	no	no
Read power per bit	15 pC	7 pC	30 pC	7 pC
Write power per bit	15 pC	7 pC	30 nC	45 pC

Table 1.1: Comparison of different memory parameters of MRAM. Adapted from [36].

struction of magnetic random access memories (MRAM). In this case an array of MTJ's is built. Each single junction can store a bit since the two possible magnetic states (parallel and antiparallel) can codify a logic '0' or '1'.

In fig. 1.4 we can see a simple scheme of such an array. One of the FM layers is pinned with an antiferromagnet. If currents are sent through two conductor paths, the combined magnetic field generated by these currents rotates the magnetization of the free layer. Another current can be sent through a junction to measure in which state it is. However, there are interferences produced by leaking currents through neighboring MTJ's. A transistor can be connected to each MTJ to eliminate this problem at a cost of a smaller storage density, but other strategies are possible as well (see [32]).

With reduced MTJ size, larger fields are needed to rotate the pinned layer and it becomes unpracticable to send the necessary currents through the conductor paths. For this reason, great efforts are endeavored studying the current induced switching or spin torque [33, 34, 35].

One on the main features of a MRAM memory lays in its non-volatility. Since no refreshing is needed, the power consumption can be reduced in comparison with DRAM or SRAM memories [3]. This feature becomes of high importance in mobile devices where the total available energy is limited by the battery.

In Table 1.1 a comparison between some parameters of different available memory systems is shown. For each kind of memory, the parameters in which MRAM has a clear advantage are marked with a grey shadow. A non-volatile memory (FLASH) has already been present in the market for some years. The

[3]Technically speaking, SRAM does not need refreshing. But a standby voltage is required which generates power loses.

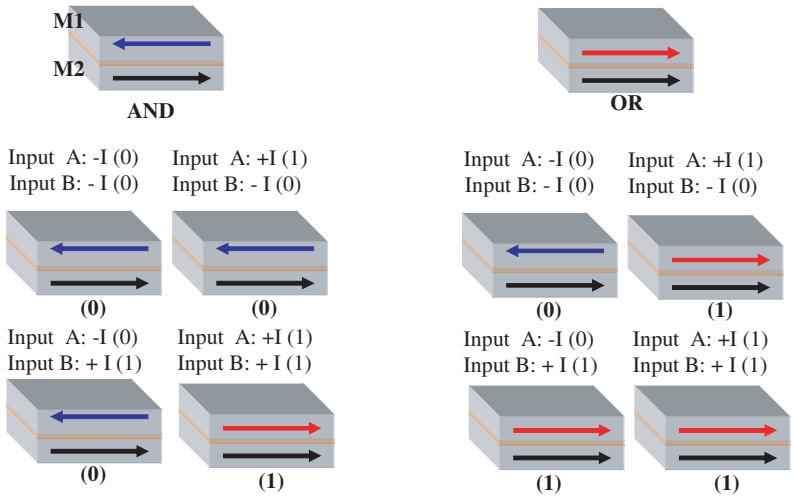

Figure 1.5: Realization of a AND and a OR gate with a MTJ. The magnetization of the bottom layer (M2) is pinned.

main drawback of FLASH is the very large write time and power. Since price and cell size of MRAM is similar to FLASH (and therefore packing density) MRAM may substitute FLASH in the future. MRAM can not compete with the high speed of SRAM memories or with the high densities achieved by DRAM systems but it can substite SRAM in battery-dependent devices where power saving considerations can compensate speed reduction.

However, some important issues remain to be solved. Since the resistance of a tunnel element depends exponentially on the barrier thickness, a very high uniformity is required in order to have a small resistance distribution. An increased TMR ratio as provided by high SP materials would be very helpful here. Similar problems are present with the coercive fields of the free layers. Nevertheless, recent reports show that these complications can be neutralized. In 2006, Freescale started the marketing of a 4 Mbit MRAM chip [39] and NEC and its partner Toshiba announced a 16 Mbit chip with 34 ns cycle time [37]. Up to now, this is still the fastest time for a MRAM chip. A review of different array schemes and reading and writing strategies can be found in [38].

Arrays of MTJ's may also have alternative uses. It has been proposed to

use them as programmable logic gate arrays or *morphware* [40, 41]. Again, two currents (inputs) are needed to rotate the magnetization of the free layer. The end state of the junction is the output bit. Fig. 1.5 shows how a logic AND or OR can be realized with a single MTJ depending on the initial magnetic configuration. The NAND(NOR) gates can be realized by reversing the direction of the current for the OR(AND) gates, by rotating the magnetization of the pinned layer or by bringing the junction to a state with *negative* TMR[4]. XOR can be built with 2 MTJ's and a full-adder with 3. The main advantage is the high flexibility achievable by re-programming of the gates. Additionally, no clock is needed and parallel processing is possible. The re-programming is as fast as the gate itself, that means as low as 5-20 ns. The future of programmable logic with MTJ'S is tied to MRAM memories since both will confront the same problems.

Further applications of MTJ's are as biosensor [42] and as magnetic sensor in general.

[4]In the negative TMR the resistance is smaller for the antiparallel configuration

Chapter 2

Half metallic Heusler compounds

2.1 General considerations

A half metal is a material whose band structure is metallic for one spin direction while for the other direction there is a gap in the density of states (DOS) at the Fermi level. Thus, a half metal has 100 % spin polarisation at E_F. The implementation of such a material in a MTJ would result in a huge increase in the TMR ratio.

Full-Heusler compounds are intermetallic alloys with the general formula X_2YZ and a $L2_1$ structure, as shown in fig. 2.1, left. Z is normally a main group element while X and Y are transition metals. The $L2_1$ structure is composed by four interpenetrating fcc lattices. The two lattices of the X atoms combine to a single cubic lattice. Half-Heusler compounds have the formula XYZ. The structure can be obtained from the $L2_1$ by substituting the X at (3/4, 3/4, 3/4) in Wyckoff coordinates by void. For this family, the structure is formed by 3 fcc interpenetrating lattices.

Many compounds from both Heusler families have been predicted to be ferromagnetic half metals. In the last years big efforts in research have been directed to implement these alloys in MTJ's to obtain the predicted large TMR. For Al_2O_3 barriers, the highest reported TMR in a MTJ with a single full-Heusler alloy electrode is 159% at 2 K for Co_2MnSi [43, 44]. For the same compound, nearly 100% TMR values have been reported by other groups [45, 46]. Similar results have been achieved for $Co_2FeAl_{0.5}Si_{0.5}$ based MTJ's [47]. For other compounds, more modest results can be found in the literature, for Co_2FeSi and Co_2FeAl TMR values of 67.5% [48] and 50% [49], respectively, are reported. All these experiments

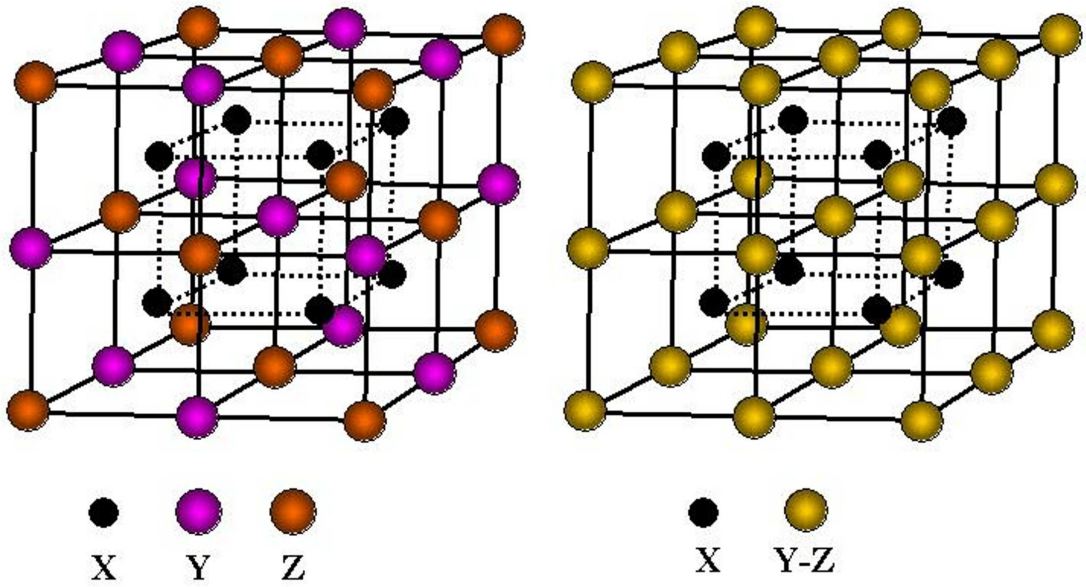

Figure 2.1: Left: $L2_1$ structure for a full-Heusler alloy. It consists in four interpenetrating fcc lattices. For the X atoms this results in a single cubic cell. Right: B2 structure, with a complete mixing between Y and Z atoms.

used CoFe as counter electrode. For half-Heusler alloys the development is much slower. Only for NiMnSb TMR values of 8.1% [50] at 4K with CoFe electrodes and 19.5% [51] at 4K with NiFe electrodes are published. Additionally, junctions using Co_2MnSi as bottom *and* top electrode show a TMR as high as 570% which is, until now, the highest value for a MTJ with amorphous barrier [52].

2.1.1 Origin of the gap in Heusler alloys

The gap in the minority DOS in Heusler compounds results from the hybridization of *d*-states of the transition metals with other transition atoms. The details differ for the case of half- and full-Heusler alloys.

Let us consider the compound NiMnSb as an example for the half-Heusler case. The situation is shown in fig. 2.2a. The strong hybridization between the

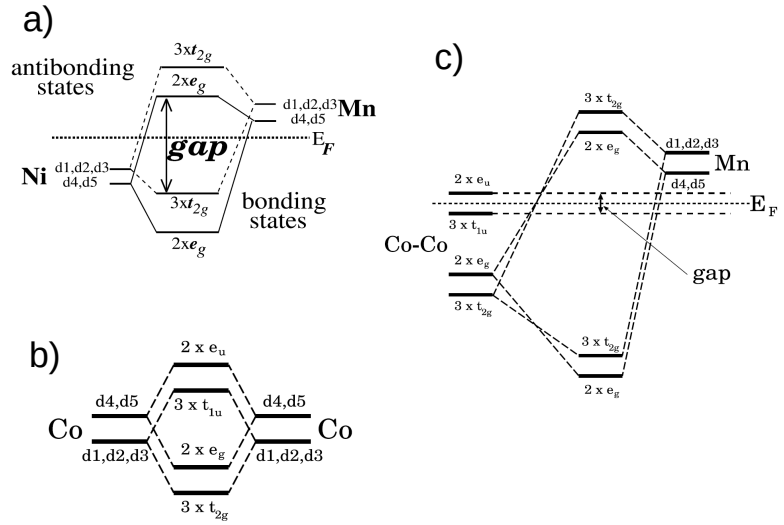

Figure 2.2: Schematic representation of the hybridization of states resulting in a gap in the minority DOS in half-(a) and full-Heusler alloys (b,c), from [53]. The notation d1, d2, d3 states for d_{xy}, d_{yx} and d_{zx} t_{2g} orbitals while d4 and d5 correspond to the d_{z^2} and $d_{x^2-y^2}$ e_g orbitals. The number before each orbital denotes the degeneracy.

d-states of Ni and Mn generates bonding and antibonding states separated by an energy gap. The *sp*-states from Sb lay energetically deeper and do not influence the DOS at the Fermi level. It must be pointed out that the hybridization by itself is always able to generate a gap in the minority DOS[1] but in order to have a half-metal E_F must lay in the gap. In this sense the Sb contribution is important. Calculations show that the substitution of Sb by another *sp*-element can shift E_F out of the gap [54]. Furthermore, the *sp*-elements play an important role by giving stability to the crystalline structure and by providing deeper lying *sp*-bands to accommodate electrons.

In the case of the full-Heusler family let us focuse only on the alloys containing Co. The situation is shown in fig. 2.2b,c for the case of Co_2MnZ compounds. Now the Co atoms are closer to each other than in the case of a half-Heusler alloys and the hybridization between them is very important although they are only second nearest neighbours. The states resulting from the Co-Co interaction hybridize

[1]In principle, the hybridization of the states would also open a gap in the majority channel. However, as pointed out by Galanakis [53], this is energetically unfavorable because E_F would lay in the middle of an antibonding band and the Mn atom would form a magnetic moment with the consequent exchange energy gain. Therefore, Mn *d* bands are shifted and join the Ni ones to form a common band.

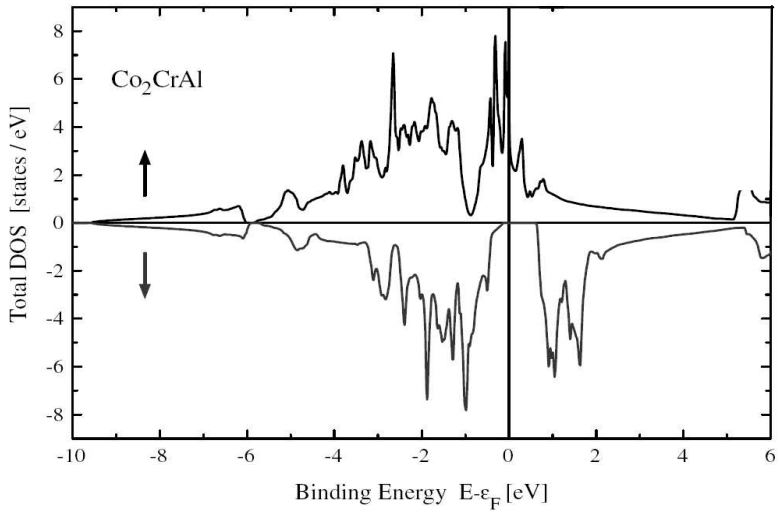

Figure 2.3: Calculation of the band structure for Co_2CrAl (from [58]). The upper (lower) part show the DOS for majority (minority) electrons. The gap in the minority channel results in a full polarisation at E_F.

with the Mn states and the gap appears in the minority DOS. The role played by the *sp*-elements is the same as in the half-heusler case. It must be noticed that the size of the gap is determined now by the Co-Co interaction.

2.2 Co_2CrAl and $Co_2Cr_{0.6}Fe_{0.4}Al$

Band structure calculations [55, 56, 57, 58] predict a half metallic character for Co_2CrAl. In fig. 2.3 the DOS for this compound is plotted, showing a gap for the minority spin channel. Crystalline and magnetic properties of bulk samples were already measured in 1981 by Buschow and Engen [59], they observed that Co_2CrAl crystallizes in the $L2_1$ structure. The Curie temperature for this compound in relatively low, 334K, which reduces the possibility of potential application.

T_C can be increased by doping with Fe atoms. Since for Co_2CrAl and Co_2FeAl the lattice constant differs only by $\sim$0.1%, in principle it is possible to tune the electronic and magnetic properties without changing the lattice parameters. With the inclusion of Fe, a family of compounds $Co_2Cr_{1-x}Fe_xAl$ can be realized and the most convenient doping concentration must be found. Calculations show that the gap closes and the spin polarisation decreases with increasing Fe content [57, 60].

The alloy $Co_2Cr_{0.6}Fe_{0.4}Al$ has attracted interest especially since the observa-

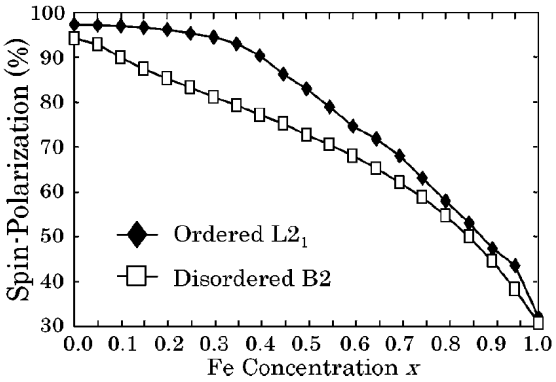

Figure 2.4: Calculation of the spin polarisation of Co_2CrAl (from [60]) versus Fe content for both $L2_1$ and B2 structures.

tion of a high magnetoresistance of 30% at room temperature for compressed powder samples [61]. The effect was observed in a small magnetic field of 0.1 T. The authors tentatively explained it as a spin polarized tunneling through grain boundaries in the sample. However, the high observed anisotropy of the effect is not compatible with polarized tunneling and alternative explanations are possible. Recently, new measurements from the same group on compact powder mixtures of $Co_2Cr_{0.6}Fe_{0.4}Al$ -Al_2O_3 showed larger magnetoresistances up to 88% [62] at room temperature. SEM investigations show an intergranular distance of 50nm, which rules out the tunneling hypothesis.

There are additional reasons to choose x= 0.4 as an optimal doping concentration. The Fe content in $Co_2Cr_{0.6}Fe_{0.4}Al$ increases the Curie temperature well above 700K. The dependence of the calculated spin polarisation on the Fe doping is most important reason. As seen in the calculations by Miura *et al.* [60] (fig. 2.4), for the $L2_1$ structure the spin polarisation stays very high until x = 0.4 where it starts to decrease faster.

2.2.1 Disorder effects

Unfortunately, the $L2_1$ structure is not the most stable for $Co_2Cr_{0.6}Fe_{0.4}Al$. This compound tends to grow in the B2 structure because the formation enthalpy for the non magnetic state is favorable to the B2 [60]. This structure represents a complete disorder between the CrFe and the Al positions (fig. 2.1, right). In fig. 2.4 we can see that the SP for B2 in smaller than for $L2_1$ but the values are still well above ($\sim$ 80%) the ones of conventional ferromagnets. The CrFe-Al

disorder has, thus, only a small effect on the spin polarisation.

Concerning the spin polarisarion (SP), the presence of disorder on the Co-Cr positions is much more disadvantageous. A disorder level of 20% would reduce the SP below 40% [60]. This kind of disorder is extremely difficult to quantify via x-ray diffraction because the scattering form factors for Co and Cr are very similar. Since Cr atoms in Co position would couple antiferromagnetically with the cobalt atoms or with themselves, a reduction in the total magnetic moment is expected. An analysis of the magnetic moments of the samples could help to estimate the degree of disorder.

2.2.2 Spin-orbit interaction and SP

In most of the early band structure calculations for half-metals the effect of the spin-orbit interaction was neglected. However, as pointed out by Mavropoulos *et al.* [63, 64], since the spin-orbit interaction couples the majority and minority states a true half-metallic gap can not exist. There is always a non-vanishing DOS in the gap which is a weak reflection of the DOS of the majority band. As a consequence a 100% spin polarisation can not exist even for perfectly ordered samples.

It must be noted that even taking into account the spin-orbit interaction the SP at the Fermi edge can still be very high. For instance, following again Mavropoulos, the introduction of the spin-orbit interaction in NiMnSb calculations reduces the SP at E_F from 100% to 99%. For other systems the reduction can be stronger, for instance, for the zinc-blende MnBi the SP falls to 77%. In the family of full Heusler alloys, for Co_2FeSi the SP reduces to 95% when spin-orbit interaction is included in the calculations [65]. In general, compounds with heavier elements, which generate stronger spin-orbit scattering, would have smaller SP.

In this context, it becomes also important how deep the Fermi level lies in the gap. The majority states near the gap edges suffer higher spin flips scattering than the states situated in the inner part of the gap.

Experimental confirmation of the effect of the spin-orbit interaction on the gap has been obtained with polarized neutron diffraction experiments. The data on Co_2MnSi and other full-Heusler alloys can only be explained assuming a small DOS in the gap [66].

Recently, calculations for Co_2CrAl and $Co_2Cr_{0.6}Fe_{0.4}Al$ including spin-orbit

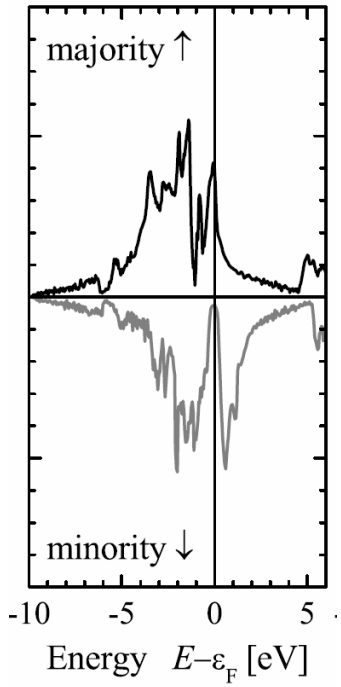

Figure 2.5: Calculation of the band structure for $Co_2Cr_{0.6}Fe_{0.4}Al$ (from [67]). The upper (lower) part show the DOS for majority (minority) electrons.

interaction have been published [67]. A non-vanishing density of states is visible in the minority gap of $Co_2Cr_{0.6}Fe_{0.4}Al$ (see fig. 2.5). Unfortunately, these calculations are valid only for the $L2_1$ structure. A calculation of the combined effects of B2 type disorder and spin-orbit scattering on the spin polarisation of $Co_2Cr_{0.6}Fe_{0.4}Al$ is still missing.

2.2.3 Is the surface/interface also half-metallic?

As already commented in Chapter 1, tunneling is interface sensitive. As a consequence, knowing if the prediction of half-metallicity in the bulk is also valid at the surface becomes of critical importance.

Even in the case of perfectly ordered surfaces with the same stoichiometry as the bulk, the prediction of half-metallicity may not be valid for the very last atomic layers. For Co_2CrAl it is possible to think is two scenarios: Co-terminated surfaces and CrAl-terminated surfaces.

For Co-terminated surfaces, Galanakis [68] argues that the low coordination number of the Co atoms at the surface would result in a smaller hybridization of

the minority bands with the Cr atoms. As a result, the minority bands move to higher energies and E_F is at the edge of a peak of Co minority states. The SP would differ strongly from the bulk value.

The situation is not so pessimistic for CrAl-terminated surfaces. The gap is preserved for this surface and a relatively high SP could be achieved. Galanakis calculates a SP of 78% for the last atomic layer, this value increases to 84% when also the subsurface layer is included.

For real samples, disorder and segregation effects at the surfaces would play a very important role. The relatively poor TMR values for NiMnSb may be explained by Mn and Sb segregation on the surface and in regions near the surface [69, 70, 71]. Such segregation effects have been also observed in full-Heusler compounds [72].

Additional complications appear if localized interface states are present in the MTJ. The problem arises when these states are in the minority channel. They can be filled or emptied from the minority bands of the electrode via inelastic scattering (electron-phonon, electron-magnon or electron-electron processes). They are also coupled to the majority band via spin-flips processes generated by the spin-orbit interaction. Since all these processes occur very fast in comparison with the tunnel process itself, the interface states act as electron reservoirs with large influence on the junction conductivity in both parallel and antiparallel configuration and consequently also on the TMR ratio [73].

2.2.4 Temperature dependence of the SP in half-metals

Even for compounds like $Co_2Cr_{0.6}Fe_{0.4}Al$ with T_C above 700K, *a priori* it is not possible to assure that the high SP will be present also at room temperature. Normally, it is assumed that the temperature dependence of the spin polarisation for HM will be the same that the magnetization, $P(T) \propto M(T)/M(0)$ [74]. However, the relation between P and M may be different and the study of this dependence is not straightforward.

For conventional ferromagnets, as long as we consider temperatures well below T_C, the only expected change in the electronic properties is a smearing of the occupied states distribution from the one at 0K. This behaviour cannot be extrapolated to half metallic ferromagnets. At the beginning of this chapter, the crucial importance of the *d-d* hybridization for the formation of the gap was mentioned. As pointed out by Ležaić *et al.*, the hybridization strength of the orbitals

may change with increasing temperature producing a shift of the electronic bands [75]. The shift of the edges of the valence and conduction bands in the gap may contribute to destroy the half-metallicity.

Additionally, thermal fluctuations generate a certain spin disorder and non-collinearility effects appear [75, 76]. Regions with short range spin order may have a spin quantization axis not parallel to the global axis. Also the spin axis direction of individual atoms may be different to the one of the local short range spin order region. This last case is most important in many-component systems like the Heusler alloys. In both cases, local spin-up states are projected in the global minority channel and the spin polarisation is reduced. Thus, the consequence of the thermal fluctuations of the magnetic moments is a mixing of both majority and minority conduction channels.

These arguments were proved right experimentally for at least one Heusler compound, NiMnSb. Neutron diffraction and XMCD experiments provide evidence for a phase transition with vanishing of half-metallicity for this compound around 80K [77, 78].

Chapter 3

Preparation of the samples

3.1 Deposition system

The samples of this work were deposited in the deposition system shown in fig. 3.1. The system is composed of several independently pumped chambers. A transfer mechanism allows the transport of samples among the different chambers without breaking the vacuum. The substrates are loaded in a small load-lock chamber with a carousel with space for six samples.

The sputtering chamber is used for the deposition of $Co_2Cr_{0.6}Fe_{0.4}Al$, Co, Al and Pt layers. A system of two coaxial discs with independent rotation allows the deposition of multilayer samples with different shadow masks. Argon gas with 99.998% purity was used for the preparation of the samples in this work. The oxidation of the Al layer to form the tunneling barrier is done in this chamber as well. For this purpose oxygen with 99.95% purity is used. Plasma oxidation was chosen as oxidation methode. A liquid nitrogen-cooled trap was used during deposition to improve the base pressure of the chamber and to remove water and oxygen as contaminants. With the trap the base pressure is in the $5{\cdot}10^{-8}$ mbar range.

In the MBE chamber, Fe and Cr are deposited using electron beam evaporation. These metals are used as buffer layers for the growth of $Co_2Cr_{0.6}Fe_{0.4}Al$. The base pressure of this chamber is 10^{-10} mbar. The MBE chamber possesses a RHEED and a LEED system which are used to study the crystallographic order and morphology of the film surface.

The surface topology of the films is studied as well by in-situ STM. The base pressure in the STM chamber is 10^{-11} mbar. In order to keep the film surface

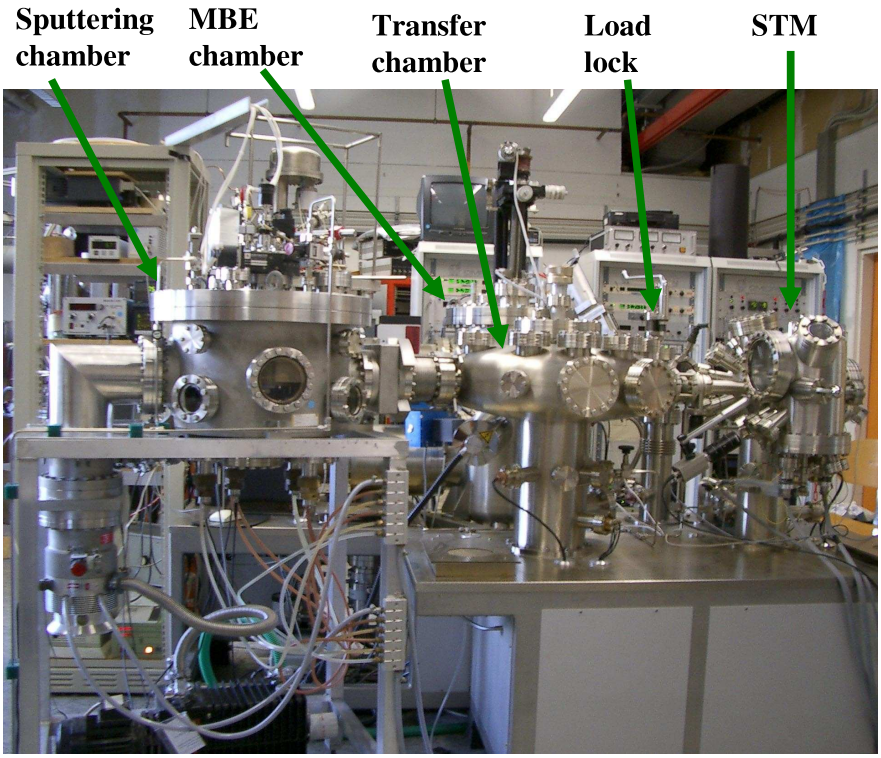

Figure 3.1: Deposition system.

as free of contaminants as possible during the transport among the different chambers, the pressure of the transfer chamber is kept in the lower 10^{-9} mbar range.

3.2 Deposition of the samples

3.2.1 Substrates preparation

In this work, Al_2O_3 $(11\bar{2}0)$, MgO (100) and $MgAl_2O_4$ (100) substrates were used. For Al_2O_3 substrates a standard wet cleaning process is performed. The substrates are cleaned in four steps in a ultrasonic bath with acetone, distilled water, acetone and isopropanol, subsequently. After loading, the substrates are heated up to 300 °C in vacuum to evaporate water and volatile organic compounds from the surface.

In order to get a clean surface of the MgO substrates, the wet process described above is not convenient. It has been observed that in the presence of humidity the

MgO surface in covered by reaction products, mainly magnesium hydroxide [79]. Only an annealing process at very high temperatures (∼1000 °C) can efficiently remove these contaminants from a MgO surface [80, 81].

For deposition of $Co_2Cr_{0.6}Fe_{0.4}Al$ films, the MgO substrates are annealed for 2 h at 950 °C in an oxygen atmosphere to prevent the loss of O atoms from the surface. After the anneal process the substrates are glued with silver glue to a metallic sample holder. After drying of the glue the substrates are exposed to a microwave oxygen plasma with a power of 100 W for 10 min. This step is intented to clean possible contaminants from the solvents present in the glue. After loading, the substrates are again annealed in vacuum in the MBE chamber for 30 min at 650 °C. The substrates adopt a slightly darker, metallic color after this last step, probably due to oxygen loss.

No information was found in literature about $MgAl_2O_4$ substrates cleaning processes. Since Mg is also present it is possible that the formation of magnesium hydroxide represents again a problem. The same cleaning process as with MgO was followed through.

3.2.2 Cr and Fe buffer layer deposition

Fe and Cr thin films are deposited in the MBE chamber using electron beam evaporation. The purity level for the pieces of metal used in this work was 99.99% for Fe and 99.97% for Cr. When a electron beam with the sufficient energy is directed to the Cr and Fe pieces, the metal starts to sublimate directly without melting. Since both Fe and Cr react with oxygen, it is usual that the surface of the pieces provided by the supplier is completely oxidized. For this reason the aspect ratio of the pieces plays a critical role for the reproducibility of the results.

In our first experiments with small pieces (∼2-3 mm diameter) a poor reproducibility of the growth of $Co_2Cr_{0.6}Fe_{0.4}Al$ was observed. A high reproducibility was only achieved when bigger (∼2-3 cm) peaces of metal were used. Before using a new piece of Cr or Fe the oxide surface must be removed. This is done in the MBE chamber by evaporating the surface of the pieces. In order to avoid the effect of additional contamination of the pieces in the chamber between different depositions, the surface is again evaporated before each deposition.

The buffer layer for the samples in this work was deposited at 130 °C and was not annealed.

3.2.3 $Co_2Cr_{0.6}Fe_{0.4}Al$ and MTJ's deposition

A buffer layer is used to grow $Co_2Cr_{0.6}Fe_{0.4}Al$ on MgO substrates while on Al_2O_3 and $MgAl_2O_4$, it is directly deposited. The films were deposited by magnetron dc sputtering with a wide range of deposition temperatures. The deposition parameters can be found in Appendix A.2. Annealing temperature and duration were also varied in order to investigate the effect in bulk and surface crystallographic order, surface topology, magnetic properties and TMR ratio of the samples. In the case of films deposited on buffer layers, the time between deposition of the Fe or Cr film and of the $Co_2Cr_{0.6}Fe_{0.4}Al$ film was kept under 30 min to prevent a possible contamination of the interface buffer/$Co_2Cr_{0.6}Fe_{0.4}Al$.

After the deposition of the $Co_2Cr_{0.6}Fe_{0.4}Al$ films the Al layer is immediately deposited in the case of non-annealed samples or transferred to the MBE chamber for annealing. The annealing of the $Co_2Cr_{0.6}Fe_{0.4}Al$ films is done in this chamber because of the lower base pressure. After annealing, the surface is studied with the RHEED or LEED system and then the sample is again transferred to the sputtering chamber for Al deposition. For some selected samples a STM image is generated additionally.

The time between Al deposition and the oxidation is also minimized. The oxidation is done by plasma oxidation in the sputtering chamber. Two kinds of gas composition for oxidation were used in this work: pure oxygen and Ar-O_2 mixture. See details in Appendix A.2. Since the chamber is contaminated with oxygen after oxidation, the top Co electrode is not immediately deposited. A minimal waiting time of 3 h is used before depositing Co.

For technical reasons concerning the lithographic process, a 11 nm Pt capping layer was deposited on top of the MTJ's. These reasons will be explained in the following section.

Materials for electrode magnetization pinning

In order to observe the maximum TMR effect, it is necessary to realize an antiparallel configuration of the magnetization of the two electrodes. Due to the similarity of coercive fields of Co and $Co_2Cr_{0.6}Fe_{0.4}Al$, this is not possible without pinning the magnetization of one of the electrodes. When a antiferromagnetic layer is in contact with a ferromagnetic layer, the hysteresis loop of the ferromagnet can be shifted and the coercive field increased [82, 83]. This effect is called *exchange bias*.

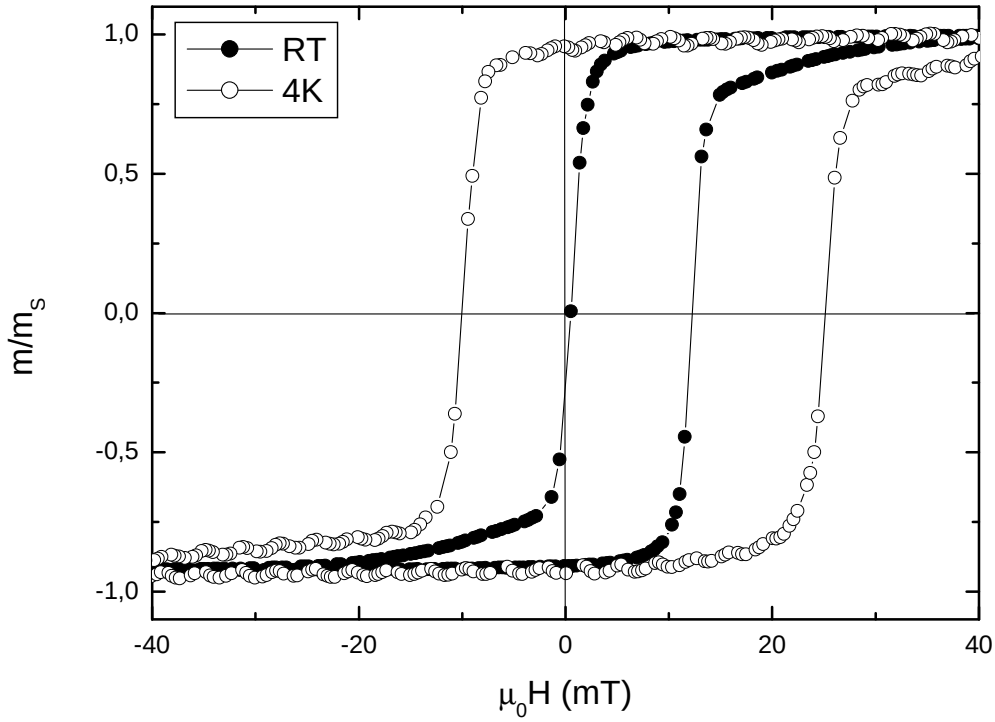

Figure 3.2: Hysteresis loops at RT and 4 K of a Co(100nm)/FeMn(13nm) sample.

The effect depends on the thickness of the AFM layer. Typically, a minimal thickness is necessary to observe the effect. After a steep increase with AFM layer thickness, the strength of the exhange bias saturates [84, 85]

A special procedure must be performed to generate the exchange bias. The sample must be heated at a temperature above T_N of the AFM but below T_C of the FM. A magnetic field is now introduced to define the axis and direction of the exchange bias. The sample is then cooled below T_N in the presence of the magnetic field. The hysteresis loop is now shifted in the opposite direction of the magnetic field. In fig. 3.2, the exchange biased hysteresis loops of a 100 nm Co thin film at room temperature and 4 K are shown. An AFM layer of FeMn with a thickness of 13 nm was used in this sample. T_N for FeMn is 490 K, the field cooling procedure was done in the sputtering chamber. A permanent magnet was used to generate the magnetic field, for this reason the value of the magnetic field is below 20 mT.

Alternatively, CoO is also used as AFM layer. The CoO layer is created by oxidizing the last layers of the Co top electrode. The oxidation time is very short to prevent a reduction of the SP in the bulk Co. The use of CoO has advantages

Material	**ΔE (erg/cm^2)**	**T_B (K)**	**T_N (K)**
CoO(oxid) (10K)	0.4-3.5	200-290	
CoO(oxid) (77K)	0.16-0.4	200-290	
CoO(poly) (10K)	0.03-0.12	290	290
CoO(111) (77K)	0.14-0.48	290	
FeMn(poly)	0.02-0.2	390-470	490(111)

Table 3.1: Comparison between FeMn and CoO exchange bias properties. The label (oxid) indicates a formation by oxidation of a previous deposited Co layer. Labels (poly) and (111) indicate direct CoO deposited polycrystalline and (111)-oriented single crystalline layers, respectively. The values of ΔE are measured at room temperature. To see the origin of the data refer to [82].

to the use of FeMn. First, it is not necessary to have an additional cathode for the deposition of CoO. Since T_N for CoO is 290 K, the field cooling procedure can be done in the same cryostat used to measure the TMR curve at low temperatures. There, higher fields can be applied. As shown in Chapter 6, the exchange bias in MTJ's was stronger using CoO than FeMn. The reason may not be explained only by the higher field but also by the nature of the Co/CoO interface. During the oxidation process, the oxidation can take place between the grain structure of the Co and therefore the effective surface of the interface is larger than in the case of deposited FeMn. Therefore, the interaction between FM and AFM is larger for Co/CoO interface. This issue was not investigated because it escapes from the main objectives of this work.

An additional temperature parameter is of importance in this discussion. When the field cooling procedure is done, the exchange bias effect does not appear immediately below T_N. The system must be further cooled below a so called blocking temperature T_B. This parameter depends strongly in the crystallographic order of the AFM material.

In Table 3.1, some parameters from the literature for FeMn and CoO deposited in different ways are shown. The parameter ΔE is the interaction energy between FM and AFM and is given per area unit and it is directly related with the strength of the exchange bias. This energy is larger when the CoO layer is formed by oxidation of a Co layer than when it is directly deposited. As commented before, the intergrain oxidation may be the reason for this behavior. On the other hand, while for directly deposited CoO samples T_B equals T_N, for oxydized samples T_B

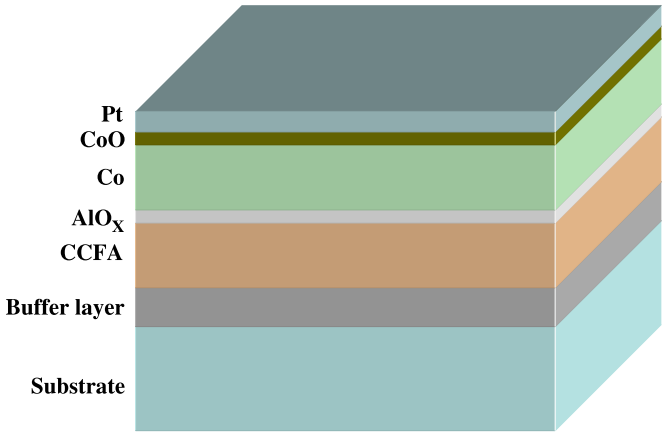

Figure 3.3: Structure of a MTJ stack. The buffer layer is only present for MgO substrates.

can be much smaller depending of the preparation conditions. This is also the case for polycrystalline FeMn.

With the introduction of a AFM layer, the final structure of a MTJ stack looks like fig. 3.3.

3.3 Preparation of mesa structures

The multilayer samples are structured to form circular mesas by means of optical lithography. The circular shape is chosen to avoid the presence of sharp edges in the structure which may not be well defined and correctly etched. The steps followed to structure a mesa are shown in fig. 3.4. Exact parameters for the different photoresists can be found in Appendix A.1.

In picture 3.4a, an as-deposited stack is shown schematically. First step consists in covering the stack with a positive photoresist (red layer in fig. 3.4b). The liquid photoresist is dropped on the sample which is situated on a spinner to achieve height homogeneity. A soft annealing step is necessary to dry the photoresist. After cooling again to room temperature, the photoresist is selectively illuminate with UV light. For this purpose, a glass mask with the desired structure is used (fig. 3.4c). The UV light exposure induces a change in the chemical properties of the photoresist and the illuminated areas can be removed with an appropriate liquid developer. In this way, the shape of the mask is translated to the photoresist (fig. 3.4d).

Now, the photoresist-free area can be etched and removed. In general, this can

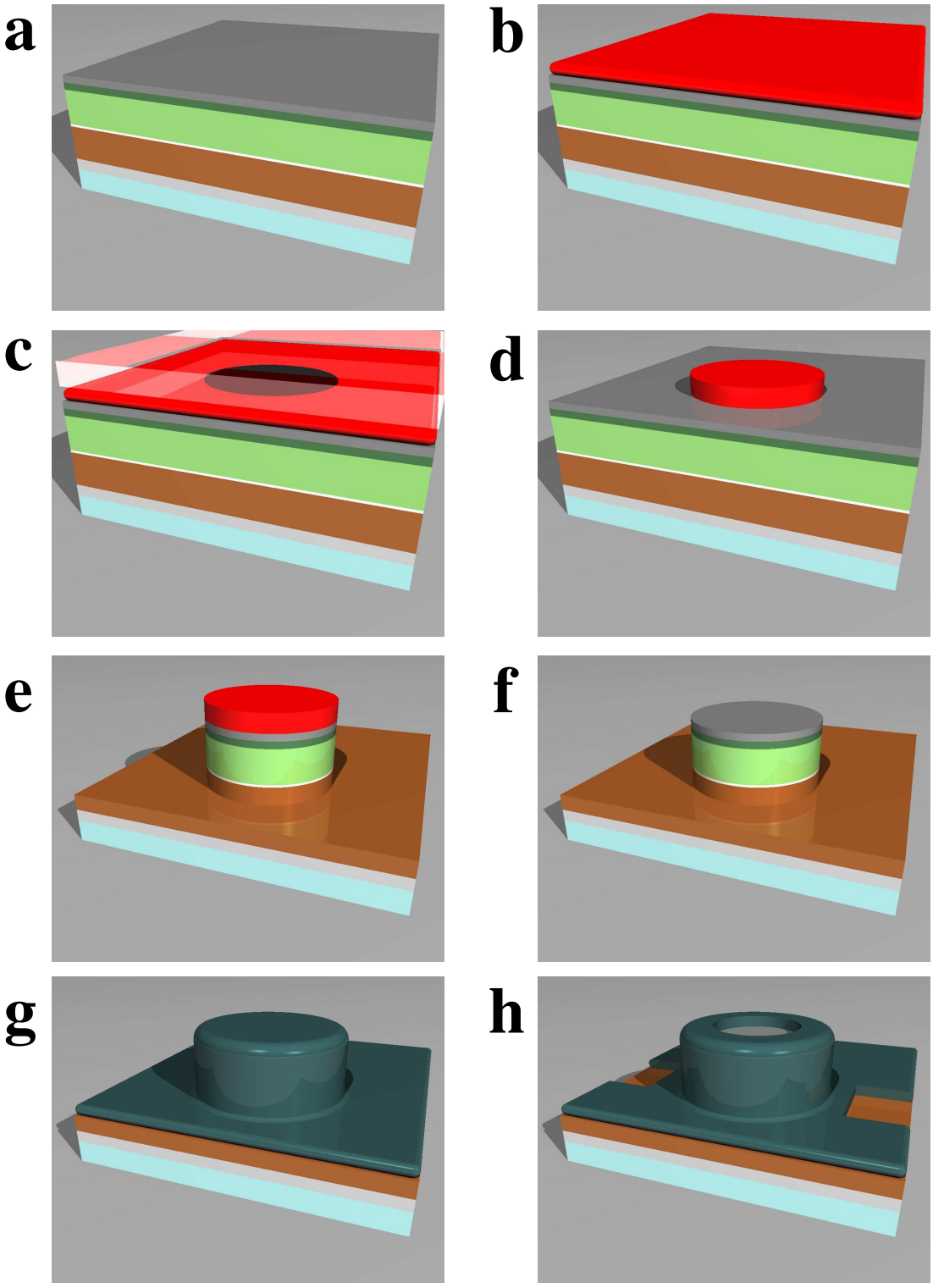

Figure 3.4: Realization of a mesa structure.

be done by chemical etching or ion beam etching. In the case of chemical etching, the sample is typically exposed to an acid which dissolves the metal. The main disadvantage with this method is that it is very difficult to control how deep the sample is etched. It must be noticed that a metallic layer must remain to send a current through the mesa. Additionally, it is not clear if the acid also affects the layers under the photoresist. For these reasons, the ion beam option was chosen. The samples are etched in an argon ion etching chamber situated inside the clean room where the lithography is carried out. The quantity of material removed from the sample is proportional to the bombardment time. A *dummy* sample with the same thickness as the top electrode can be etched simultaneously, when the substrate of the dummy sample is visible the top electrode is etched. The etching process is continued until a part of the bottom electrode is also etched. After the etching process, the sample is in the situation shown in fig. 3.4e. The sample rotates during the etching process around an axis centered on the sample surface and perpendicular to it. The rotation axis can be tilted with respect to the direction of the incoming ions.

The positive resist can be now removed with acetone (fig. 3.4f). The capping layer acquires importance at this point. In first samples deposited without Pt capping layer it was observed that the positive photoresist was not efficiently removed by the acetone. We believe that this is due to a reaction between the photoresist itself and the CoO layer or surface contaminants mediated by humidity. The samples are always exposed for at least one hour to air before setting them inside the clean room. On humid summer days, the problem with the photoresist is more evident. The problem disappears with the use of a Pt capping layer.

The presence of rests of photoresist may be difficult to observe with the microscope due to low colour contrast. It is always possible to identify the presence of photoresist by observing the temperature dependence of the mesa resistance. In the presence of photoresist, the resistance exhibits a nearly exponential increase with reducing temperature.

A second photoresist is now put on the sample (fig. 3.4g). As before, the spinner is used. A special photoresist, with very good insulating properties is chosen (see Appendix). This photoresist is of the negative type, i.e. the illuminated areas are now removed by the developer. The same procedure as before is used to open a window on top of the mesa structure (fig. 3.4h). Additional windows are open to contact the bottom layer. The copper cables used to perform the

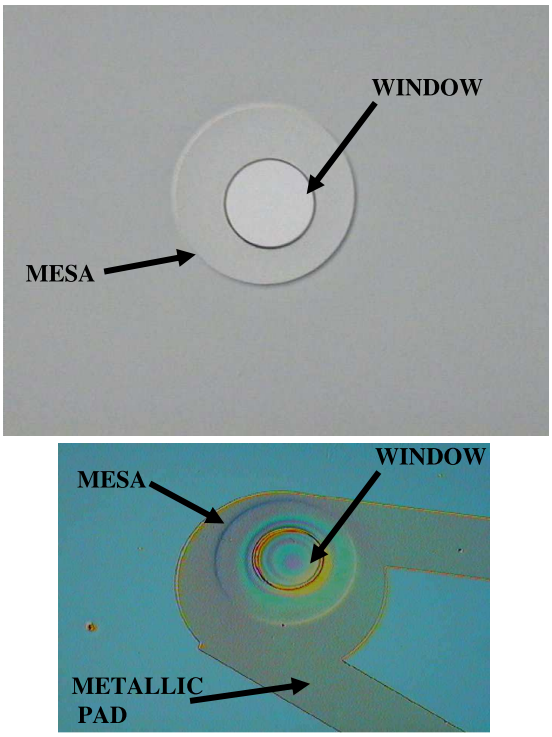

Figure 3.5: Top: photograph of a mesa structure with a diameter of 200 μm. Bottom: photograph of a mesa structure with a diameter of 150 μm with a metallic contact pad.

measurements are attached to the samples with silver glue. Due to the small size of the mesa, a three-points measurement geometry is used. This is not a drawback because the contact resistances (a few Ω) are much smaller than a typical junction resistance (hundreds of Ω).

Alternatively, metallic Au and Al contacts pads deposited on the second photoresist were also tried without success. It must be pointed out that the thickness of the negative photoresist is in the order of a μm while typical thicknesses of the metallic pads are in the order of 100 nm. The sharp step of the photoresist at the windows on the mesas cannot be well covered by the metallic pad. As a consequence, there is no electrical contact between the metal on the top of the step and the metal on the bottom. In other words, the metallic pads have no contact with the Pt capping layer on top of the mesas and can not be used to measure the electrical properties of the junctions. In fig. 3.5 top a picture of a mesa structure with a diameter of 200 μm is shown. The picture was acquired with an optical microscope. The bottom picture shows a mesa with a metallic pad.

3.3.1 Etching angle dependence

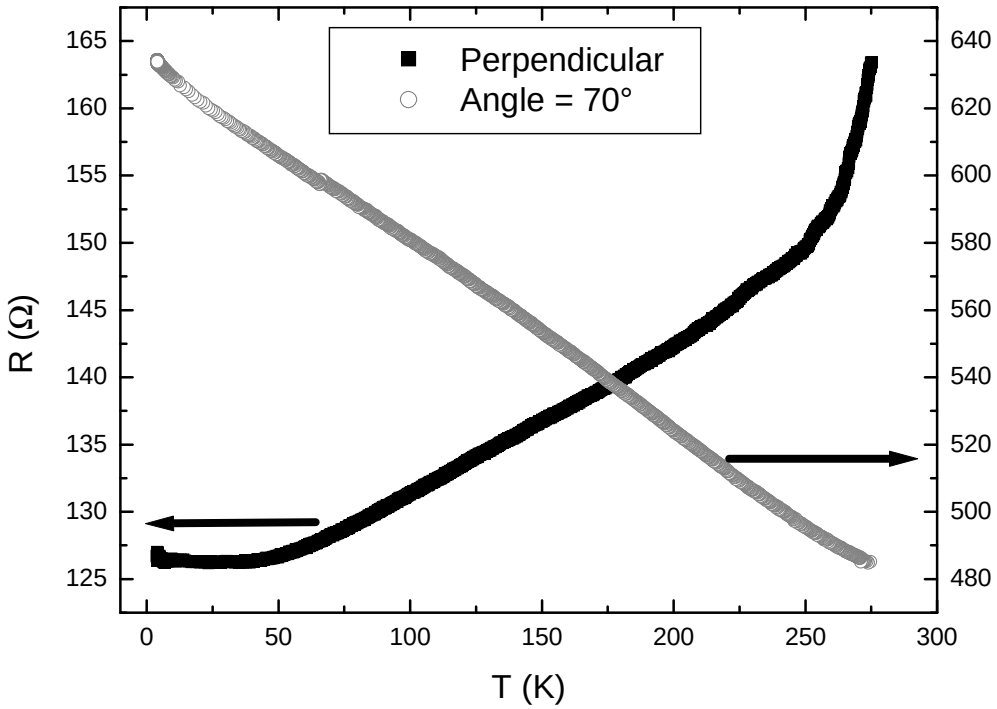

Figure 3.6: Resistance versus temperature for two mesa structures etched perpendicular and with an angle of 70° respect to the normal to the film surface.

The angle of incidence of the ion beam to the sample surface has a strong influence on the electrical properties of the mesa structures. In fig. 3.6 the temperature dependence of the resistance for two different samples is shown. Both samples were deposited with the same parameters. It was observed that when the ion bombardment is perpendicular to the surface, the resistance of the mesas show a typical metallic behavior, with resistance decreasing with temperature. The same occurs when the angle between the ion beam direction and the normal to the film surface is relatively small ($\lesssim 70\,^{\circ}$).

The situation changes when the angle reaches values around 70°. The behavior of the mesa resistance looks more than the one for an insulator (see again fig. 3.6). The resistance increases almost linearly with decreasing temperature.

Concerning TMR values, in samples showing metallic behavior the TMR value was always zero or smaller than 1%. The absolute resistance is also smaller for this kind of mesa for otherwise comparable junctions.

We conclude that the reason for this etching angle dependence lies in the

metal deposited *on the sides* of the mesa structure. During the etching process, part of the etched material deposits again on the sides causing a direct contact between top and bottom electrode. Therefore, for the case of low angle etching, the mesas are shortcircuited and the current does not flow through the barrier.

When the angle is larger, the sides of the mesa are also etched and the deposited material is removed. In this case the current flows through the barrier and the tunneling process can be studied. The importance of the rotation of the sample during the etching process must be pointed out. The rotation allows the etching of the sides from all directions.

Chapter 4

$Co_2Cr_{0.6}Fe_{0.4}Al$ thin films

4.1 Crystallographic properties

4.1.1 General considerations

In Chapter 2 it was already pointed out that different types of atomic disorder may be present in $Co_2Cr_{0.6}Fe_{0.4}Al$. The analysis of x-ray diffraction data provides valuable information about the presence of a certain type of disorder and, in some cases, it is possible to quantify the degree of disorder.

PowderCell [91] is a software intended to simulate x-ray diffraction in powder samples. The program provides the angular and relative intensity distribution of the different reflections of the desired crystalline structure.

In fig. 4.1, a simulation for the different disorder types of $Co_2Cr_{0.6}Fe_{0.4}Al$ is shown. The green line corresponds to the $L2_1$ structure shown in fig. 2.1 left. Information about the kind of degree of disorder can be obtained by analyzing the (111), (200) and (400) reflections. For the case of a complete disorder in the CrFe-Al positions (red line) the (111) reflection vanishes. This is equivalent to the B2 structure shown also in fig. 2.1. Furthermore, if additionally there is a complete disorder in the Co-Cr atomic positions, also the (200) reflection disappears (gray line). The structure resulting of the combination of these two types of disorders is called A2.

It must be noticed that the presence of the (111) reflection is characteristic of the $L2_1$ structure but its presence does not rule out the presence of CoCr-type disorder. Only in simulations with pure CoCr disorder, the (200) peak intensity is almost null.

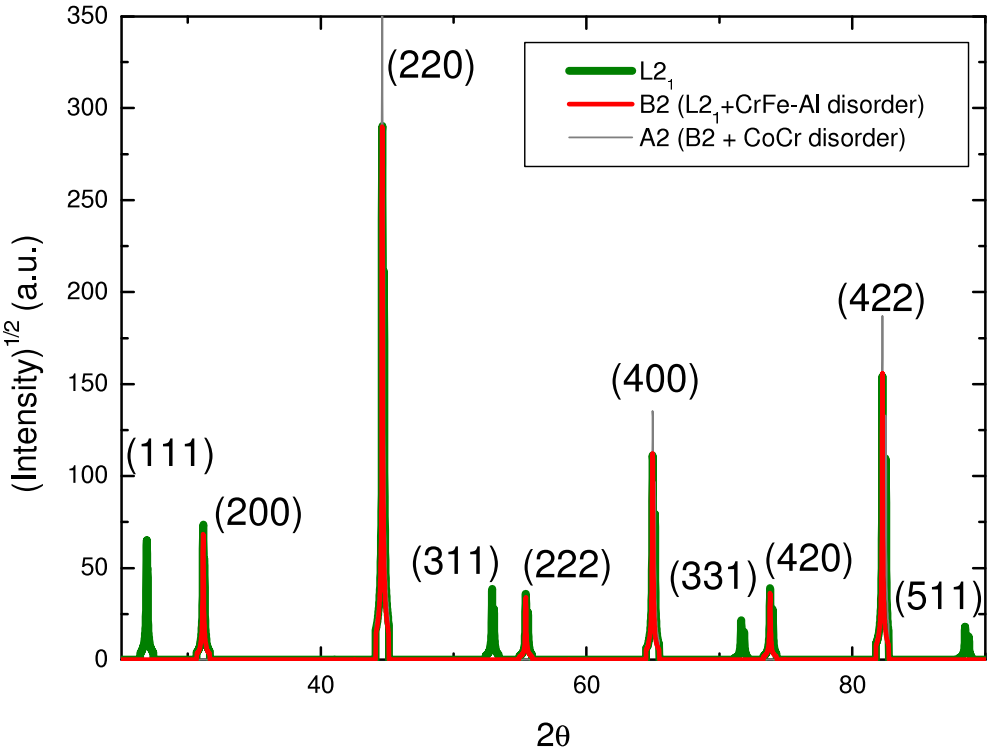

Figure 4.1: PowderCell simulation of a $\theta/2\theta$ scan with Bragg-Bentano geometry for different kinds of possible structures of $Co_2Cr_{0.6}Fe_{0.4}Al$.

The lattice constant for $Co_2Cr_{0.6}Fe_{0.4}Al$ used in these simulations is the same as in Table 4.1.

4.1.2 Polycrystalline samples

Previous work from G. Jakob *et al.* [86] on $Co_2Cr_{0.6}Fe_{0.4}Al$ deposited on Al_2O_3 $(11\bar{2}0)$ substrates showed that a deposition temperature above 400 °C is needed to induce epitaxial growth. For lower temperatures, the scattering intensity vanished in x-ray diffractograms. Growth morphology considerations allowed Jakob *et al* to suggest a nanocrystalline structure for films deposited at low temperatures.

The samples deposited for this work at low temperature on Al_2O_3 substrates showed no phase as well. A transmission electron microscope (TEM) was used to analyze the microcrystalline structure of these samples. For this purpose, a cross section of the sample must be cut and thinned up to thicknesses below 100 nm. Information about TEM imaging and interpretation can be found in [87], the sample preparation is described in [88].

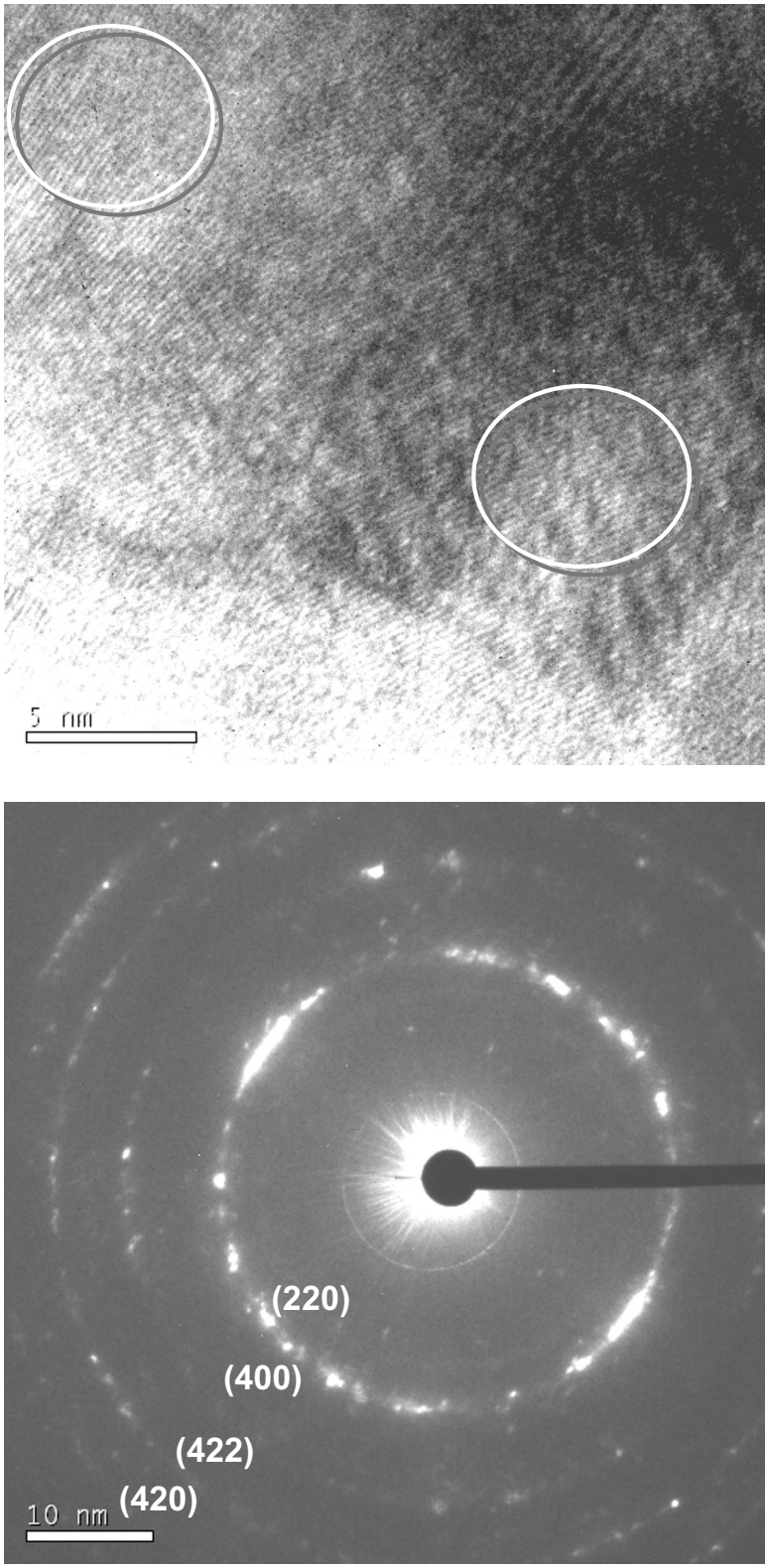

Figure 4.2: Top: TEM image of a polycrystalline sample deposited on Al_2O_3 at room temperature. The circles mark crystallites with different crystalline orientation. Bottom: Electron diffraction pattern of the same sample. Reflections corresponding to the B2 structure can be identified. Both figures are courtesy of Christian Herbort.

	a (Å)	**Parameter of interest**	**Misfit with CCFA**	**Misfit with MgO**	**Misfit with $MgAl_2O_4$**	**Misfit with Al_2O_3**
Fe	2.8665	2a	0.07	3.7	0.6	-
Cr	2.8840	2a	0.5	3.1	1.8	-
CCFA	5.7370	a or $a/\sqrt{2}$	-	3.6	0.37	1.6
MgO	4.2030	$\sqrt{2}\,a$	3.6	-	-	-
$MgAl_2O_4$	8.0830	$\sqrt{2}\,a/2$	0.37	-	-	-
Al_2O_3	4.7580	$a\cos(30^o)$	1.6	-	-	-

Table 4.1: Lattice constants and misfits (in absolute value) between the different materials of interest for this work. Misfits are given in percent values. The lattice constant for $Co_2Cr_{0.6}Fe_{0.4}Al$ is taken from [89]. Other values are from [90].

In the top picture in fig. 4.2, a TEM image of a polycrystalline $Co_2Cr_{0.6}Fe_{0.4}Al$ film deposited on Al_2O_3 at room temperature is shown. Several crystallites with different crystallographic orientation can be seen. This confirms the hypothesis of Jakob *et al.*

In order to observe which is the crystalline structure of these crystallites, electron diffraction is used. Unfortunately, due to technical limitations of the microscope, it is not possible to obtain a diffraction pattern of a single crystallite with the size of the ones observed in our samples. The resolution of the device is limited by the optics of the electron beam. The size of the smallest available aperture between incident beam and sample allows to irradiate a region with a minimal diameter of 100 nm. This area is larger by a factor of 60 than the area shown in the top picture of fig. 4.2. That means that a diffraction pattern will be a result of diffracted electrons from an area containing more than 1200 of these crystallites (assuming an average size of 5 nm for a crystallite). However, the aperture is not in direct contact with the sample, a direct projection is not realistic and the number of crystallites contributing to a diffraction pattern is indeed larger.

In fig. 4.2 bottom, the electron diffraction pattern for this sample is shown. The bar with a circular structure at the end is a mask intended to protect the electron detector from the primary beam. The observation of circles in the pattern instead of point reflections is explained by the polycrystalline nature of the sample

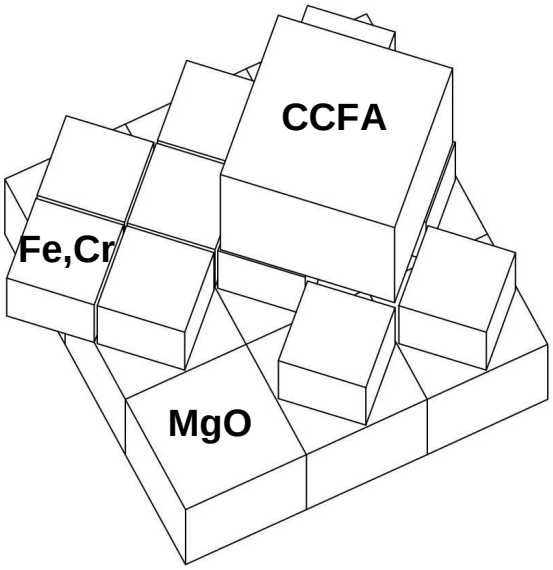

Figure 4.3: Schematic representation of the epitaxial relationship of a CCFA thin film on an Fe or Cr buffer layer on a MgO (100) substrate.

and the previous considerations. However, it is possible to identify each of these circles with a reflection of the B2 structure of $Co_2Cr_{0.6}Fe_{0.4}Al$. On the other hand, the (111) reflection, characteristic for the $L2_1$ structure, is not present. From this we conclude that the samples deposited on Al_2O_3 substrates at low temperature possesses a polycrystalline nature and the crystallites have the B2 structure.

Samples with similar polycrystalline nature were obtained when deposited on MgO and $MgAl_2O_4$ substrates without post deposition annealing.

4.1.3 Epitaxial films with buffer layer

A buffer layer is used to induce epitaxial growth of $Co_2Cr_{0.6}Fe_{0.4}Al$ on MgO substrates. In this work, Cr and Fe were used for this purpose. A schematic representation of the epitaxial growth of $Co_2Cr_{0.6}Fe_{0.4}Al$ films on Cr and Fe buffer layers is shown in fig. 4.3. The buffer layers and the $Co_2Cr_{0.6}Fe_{0.4}Al$ films grow (100) oriented but the unit cell of both layers is rotated by 45° with respect to the substrate unit cell. The lattice constant mismatch between $Co_2Cr_{0.6}Fe_{0.4}Al$ and Fe and Cr ($[2a_{Fe,Cr} - a_{CCFA}]/a_{CCFA}$) is 0.07% and 0.5%, respectively. In Table 4.1, a summary of the lattice constants and mismatches between the different materials employed in this work is shown.

In figs. 4.4 and 4.5, two-circle x-ray diffractograms of $Co_2Cr_{0.6}Fe_{0.4}Al$ films on

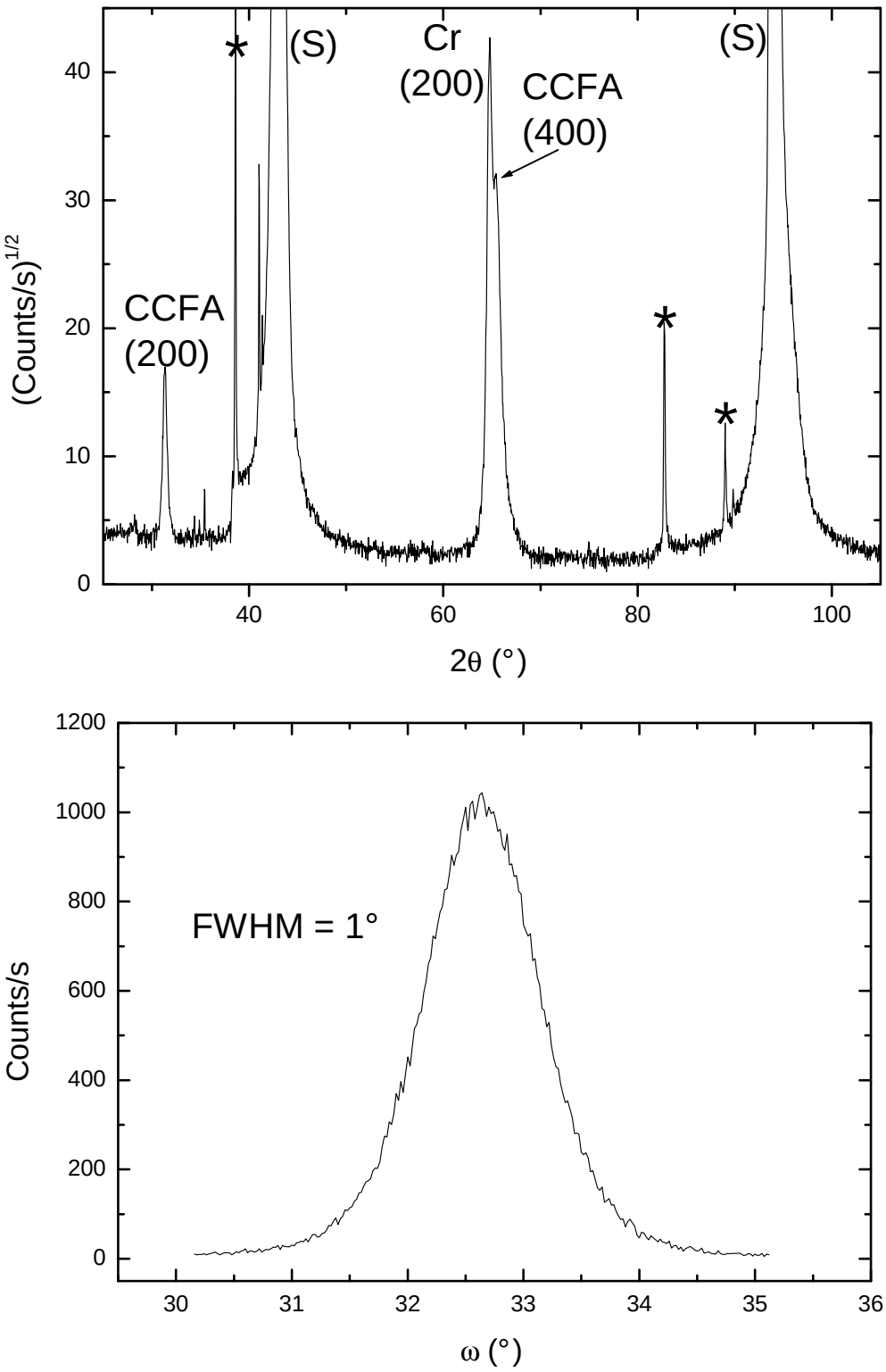

Figure 4.4: Top: $\theta/2\theta$ scan of a 100 nm thick CCFA film deposited at 100 °C on a 50 Å thick Cr buffer layer on a MgO (100) substrate. Bottom: Rocking curve of the (400) reflection.

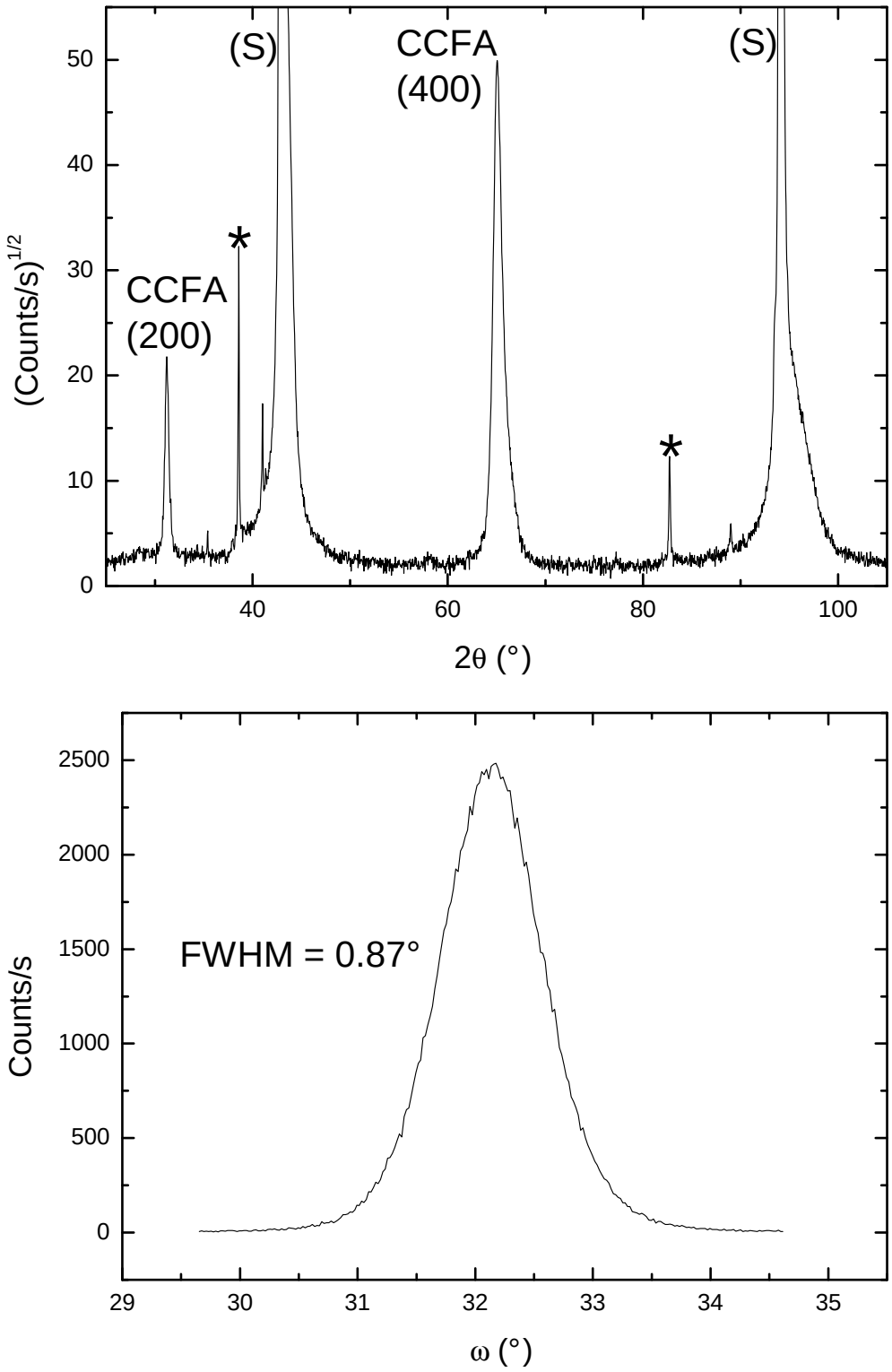

Figure 4.5: Top: $\theta/2\theta$ scan of a 100 nm thick CCFA film deposited at 100 °C on a 100 Å thick Fe buffer layer on a MgO (100) substrate. Bottom: Rocking curve of the (400) reflection.

a Cr and a Fe buffer layer are shown. The rocking curve for the (400) reflection of $Co_2Cr_{0.6}Fe_{0.4}Al$ is also shown. In the case of a Cr buffer layer it is possible to distinguish between the $Co_2Cr_{0.6}Fe_{0.4}Al$ (400) reflection and the Cr (200) reflection. In samples with Fe buffer layer, the Fe (200) reflection can not be separated. The buffer layer was deposited at 130 °C and the $Co_2Cr_{0.6}Fe_{0.4}Al$ layer at 100 °C in both cases. The thicknesses were 50 Å for Cr and 100 Å for Fe. The observation of the (200) reflection for $Co_2Cr_{0.6}Fe_{0.4}Al$ already excludes a complete disorder in the Co-Cr positions. However, a certain amount of disorder between this atomic positions may still be present. A quantification of the the disorder level can be found in section 4.1.5.

The width of the rocking curve of our samples is related to the distribution of the crystalline orientation of the crystallites in the film and to the lateral (in-plane) correlation length.

For as-deposited films on Fe and Cr buffer layer the typical values for the full width at half maximum (FWHM) lay between 0.7 ° and 1.2 °.

With a two-circle diffractometer it is only possible to study *specular* reflections, i.e., reflections for which the transferred momentum vector is perpendicular to the film surface. In order to prove in-plane order in the samples, *off-specular* reflections must be studied. For this purpose a four-circle diffractometer is employed.

Fig. 4.6 shows a ϕ-scan of the (220) equivalent reflections of a 100 nm thick $Co_2Cr_{0.6}Fe_{0.4}Al$ film deposited on a Fe buffer layer. To realize this the film must be tilted by 45 ° with respect to the scattering plane and then scanned by rotating around the film surface normal. The presence of well defined peaks proves that the film is indeed in-plane oriented. In the figure the scan for the MgO (220) equivalent reflections are also plotted and it can be seen that they are displaced by 45 ° with respect to the $Co_2Cr_{0.6}Fe_{0.4}Al$ peaks. This validates the epitaxial relation introduced in fig. 4.3. The same study was done on samples deposited on Cr buffer layers with identical results.

The (111) reflection, characteristic of the $L2_1$ structure is never observed in films deposited on either Cr or Fe buffer layers. From the observation of the (200) reflection it is concluded that the films posses the B2 structure.

The thickness of the buffer layer was varied between 20 Å and 500 Å. No differences are seen in the crystallographic properties of samples with buffer layer thickness between 100 Å and 500 Å. In samples deposited with Fe buffer layer thicknesses of 20 Å and 50 Å no phase is observed in the diffractogram. This

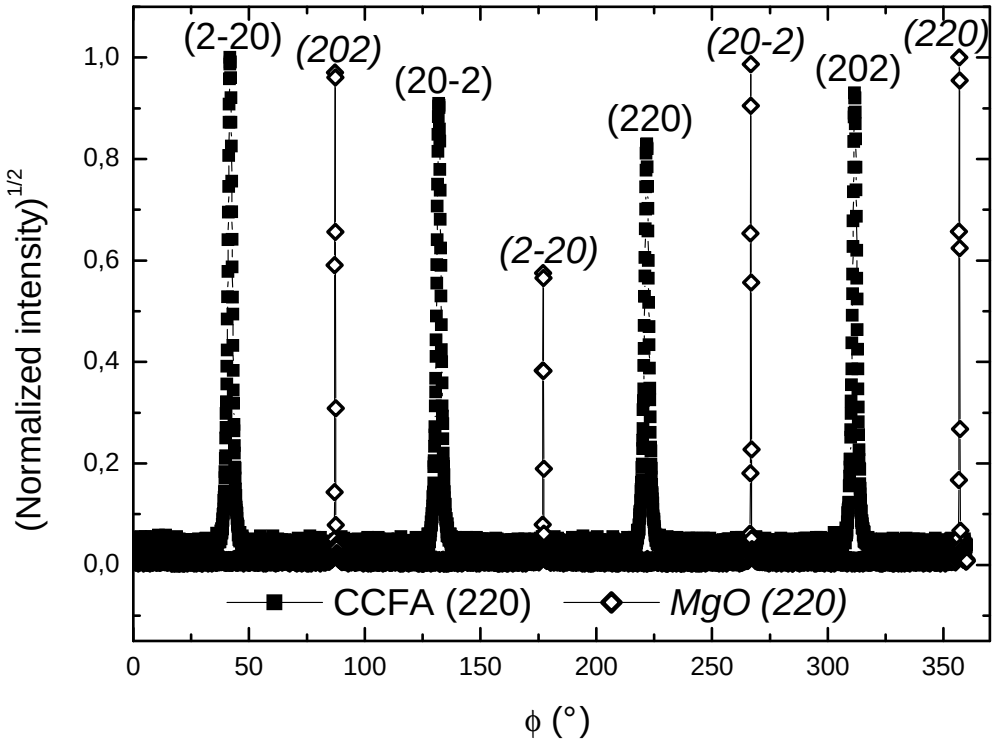

Figure 4.6: X-ray ϕ-scan of the (220) equivalent reflections of a CCFA film deposited at 100 °C (filled symbols) and of the MgO substrate (open symbols, peaks labeled in italics). A Fe buffer layer was used in this sample.

behavior can be tentatively explained by considering the lattice mismatch between Fe and MgO $(2a_{Fe} - \sqrt{2}a_{MgO})/2a_{Fe} \simeq 3.7\%$. A large stress or eventually a high number of dislocations and disorder can be expected for the first Fe layers on the MgO substrate. This stress relaxes in the subsequent atomic layers and allows an epitaxial growth of $Co_2Cr_{0.6}Fe_{0.4}Al$. For the case of Cr buffer layer, epitaxial growth was achieved already for a Cr thickness of 50 Å. The reason for this difference is not clear but it may be related to the smaller misfit between Cr and MgO compared with the misfit between Fe and MgO (see Table 4.1).

The effect of the dislocations on the buffer thickness dependence was studied with a TEM. Fig. 4.7 (top) shows a TEM image of the buffer layer area. A region with high disorder level is easily recognizable at the interface between the MgO substrate and the Fe layer. With the dislocations, the lattice mismatch between Fe and MgO is compensated in the first atomic layers. $Co_2Cr_{0.6}Fe_{0.4}Al$ can then grow epitaxially on a stress-free Fe surface as proved by the absence of distortions at the interface CCFA/Fe. The bottom panel in fig. 4.7 shows a region

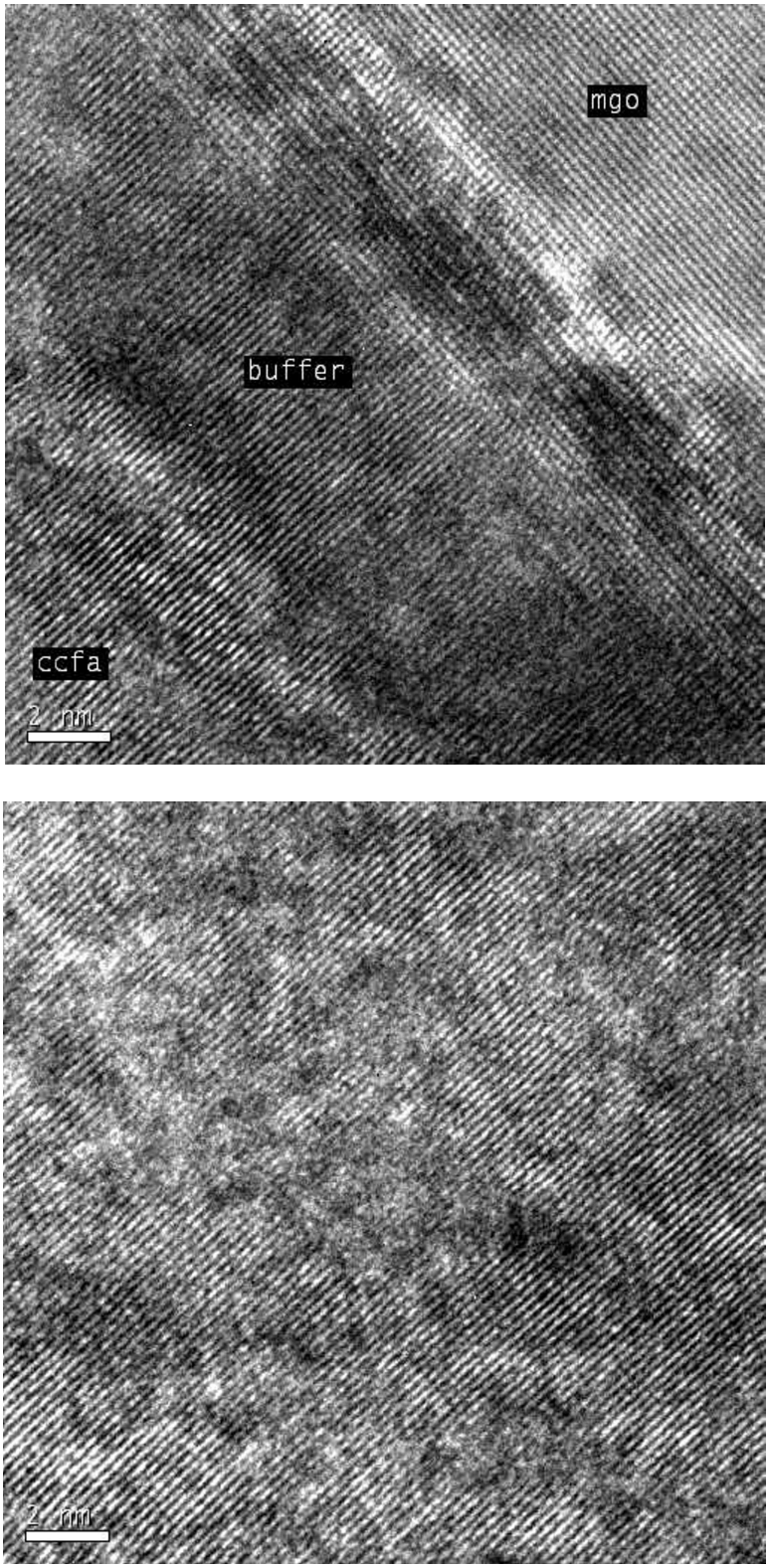

Figure 4.7: Top: TEM image of the buffer layer region of a $Co_2Cr_{0.6}Fe_{0.4}Al$ thin film on a Fe buffer on a MgO (100) substrate. Bottom: TEM image of a region situated in the bulk of the film proving single-crystallinity. Courtesy of Christian Herbort.

in the bulk of the film. The single crystalline nature of the $Co_2Cr_{0.6}Fe_{0.4}Al$ films can be recognised.

Surprisingly, the use of a buffer layer on $MgAl_2O_4$ substrates did not result in an epitaxial growth of $Co_2Cr_{0.6}Fe_{0.4}Al$. In Table 4.1, it can be seen that the lattice mismatch of Cr and Fe with $MgAl_2O_4$ is smaller than in the case of MgO. The reasons for this behavior is not understood. It may be argued that another special cleaning procedure, different from the one used for MgO substrates, must be employed. However, as explained later on in section 4.1.4, direct deposition on $MgAl_2O_4$ substrates did indeed result in epitaxial growth. This rules out the possibility of a degradated or contaminated $MgAl_2O_4$ surface.

Subsequent annealing for 5 min of the films at temperatures above 500 °C results in an improvement of the crystalline properties as seen in an increase of the scattering intensity. However, the width of the rocking curves is not smaller for annealed samples. The annealing process has a large effect on the surface crystalline order and on the atomic disorder. These points will be discussed in sections 4.4 and 4.1.5.

4.1.4 Epitaxial films without buffer layer

Alternatively to the use of a buffer layer, experiments were done to achieve epitaxial growth directly on MgO, Al_2O_3 and $MgAl_2O_4$ substrates. There are different reasons to prefer a direct deposition. First of all, a smaller number of deposition steps for every sample reduces time and cost. The simplification of the process reduces also the number of deposition parameters and the process becomes more controllable. Furthermore, the interference of the buffer layer may complicate the realization of certain kind of measurements. For instance, transport measurements are not possible when good conducting metallic underlayers are used. Additionally, it is an open question if, during the annealing processes, diffusion from the buffer layer into the film takes place. This process would change the stoichiometry of the sample and may be difficult to detect.

Single crystalline $Co_2Cr_{0.6}Fe_{0.4}Al$ samples were realized on Al_2O_3 $(11\bar{2}0)$ and $MgAl_2O_4$ (100) substrates upon annealing at temperatures over 500 °C . In contrast with the samples deposited on a buffer layer, the x-ray diffraction pattern for as-deposited samples does not show any peak corresponding to $Co_2Cr_{0.6}Fe_{0.4}Al$ reflections. In this case, the annealing step is needed to induce order in the films.

In fig. 4.8 the results of the two-circle diffractometry on a sample deposited on

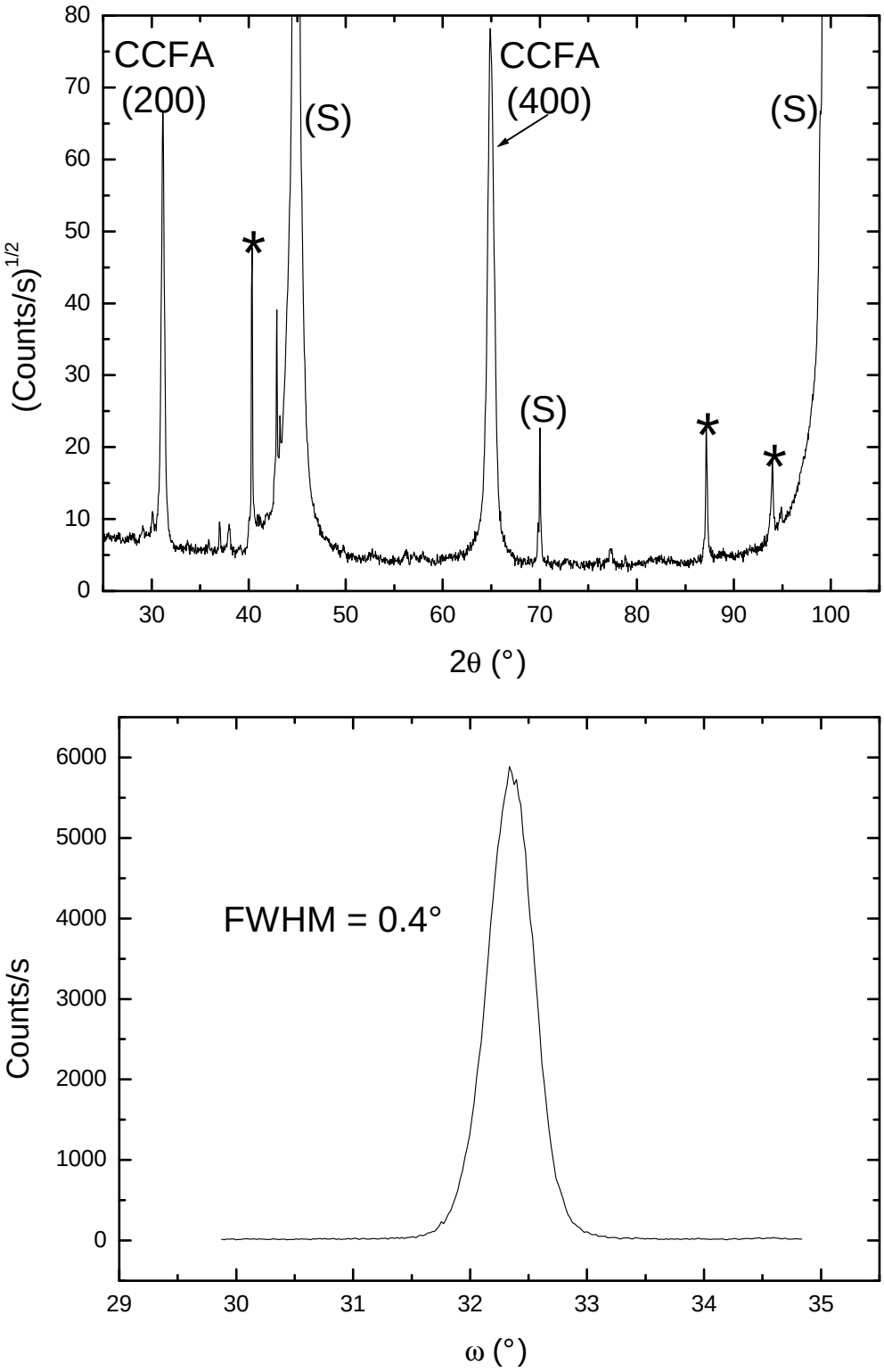

Figure 4.8: Top: $\theta/2\theta$ scan of a 100 nm thick CCFA film deposited at 100 °C on a $MgAl_2O_4$ (100) substrate and annealed at 600 °C . Bottom: Rocking curve of the (400) reflection.

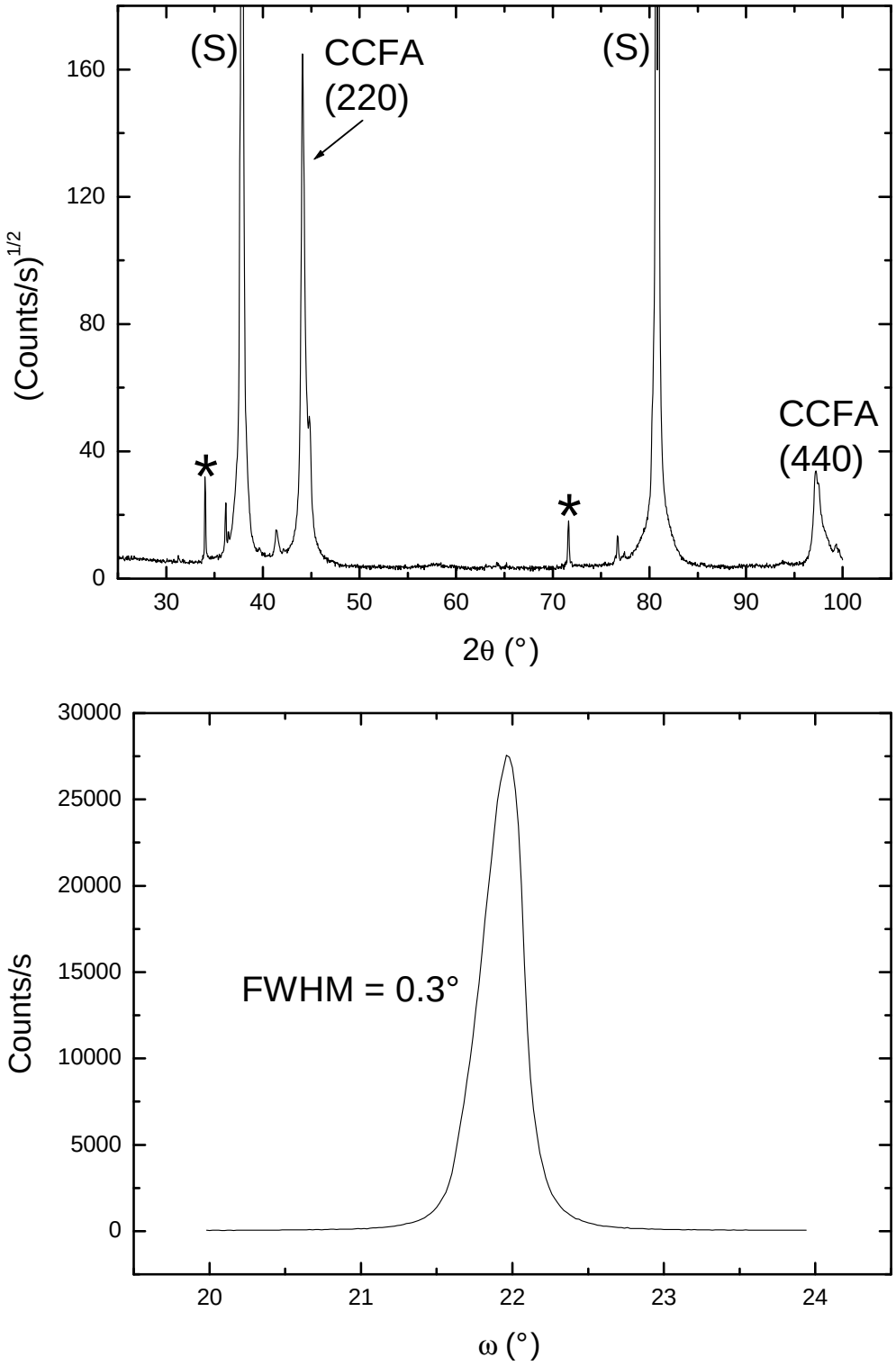

Figure 4.9: Top: $\theta/2\theta$ scan of a 100 nm thick CCFA film deposited at 100 °C on an Al_2O_3 $(11\bar{2}0)$ substrate and annealed at 600 °C . Note the small shoulder on the right side of the (220) peak. Bottom: Rocking curve of the (220) reflection.

$MgAl_2O_4$ at 100 °C and annealed at 600 °C for 5 min are shown. The top graph shows the $\theta/2\theta$ scan while the rocking curve of the (400) reflection appears at the bottom picture. The films grow with the same orientation as the films deposited on buffer layers but the widths of the rocking curve are smaller for the direct deposition case. The smaller width can not be explained in terms of lattice mismatch between $Co_2Cr_{0.6}Fe_{0.4}Al$ and $MgAl_2O_4$ $(\sqrt{2}\,a_{MgAl_2O_4}/2 - a_{ccfa})/a_{ccfa} \simeq 0.4\%$ since this is comparable to the mismatches between Fe, Cr and $Co_2Cr_{0.6}Fe_{0.4}Al$ (see Table 4.1).

Epitaxial $Co_2Cr_{0.6}Fe_{0.4}Al$ films were also deposited on Al_2O_3 $(11\bar{2}0)$ substrates. As in the case of MgO substrates, an annealing step is necessary to obtain crystalline order when the films are deposited at low temperatures. Epitaxial growth of $Co_2Cr_{0.6}Fe_{0.4}Al$ films on Al_2O_3 substrates have been already achieved by Jakob *et al.* [86]. The strategy followed by Jakob *et al* consisted in depositing at high substrates temperatures without annealing step. For deposition temperatures above 600 °C , films with good crystalline order were obtained. However, the surface morphology of these films makes them unsuitable for tunneling experiments. As observed by ex-situ atomic force microscopy, the surface exhibits a large roughness resulting from an island-type growth of the films. The surface possesses 200 nm width islands separated by deep trenches which even prevent electrical conduction for films thicknesses around 20 nm.

By depositing at low temperatures and with a short thermal treatment, epitaxial growth with smoother surfaces can be achieved. In fig. 4.9, the $\theta/2\theta$ scan (top) of a $Co_2Cr_{0.6}Fe_{0.4}Al$ films deposited on Al_2O_3 $(11\bar{2}0)$ at 100 °C and annealed at 600 °C for 5 min is shown. On this substrate the films grow (110)-oriented. Again, in-plane order was proved by four-circle diffraction by observing the (400) equivalent reflections. The (111) reflection is not observed. The bottom graph show the rocking curve of the (220) reflection. The width of the rocking curve, 0.3 °, is smaller than for samples deposited on buffer layers (∼0.6 °) and $MgAl_2O_4$ (∼0.4 °). However, on the right side on the (220) and (440) reflections in the $\theta/2\theta$ scan, a small shoulder is visible. This structure has been only observed on samples deposited on Al_2O_3 substrates. A possible explanation may lay be coexistence of strained domains in the film, most probably at the interface substrate-CCFA.

The existence of these strained domains may be related with the growth orientation of the $Co_2Cr_{0.6}Fe_{0.4}Al$ unit cell with respect to the Al_2O_3 unit cell. The misfit value between $Co_2Cr_{0.6}Fe_{0.4}Al$ and Al_2O_3 $(11\bar{2}0)$ presented in Table 4.1 is calculated assuming the situation presented in the left panel of fig. 4.10. Consid-

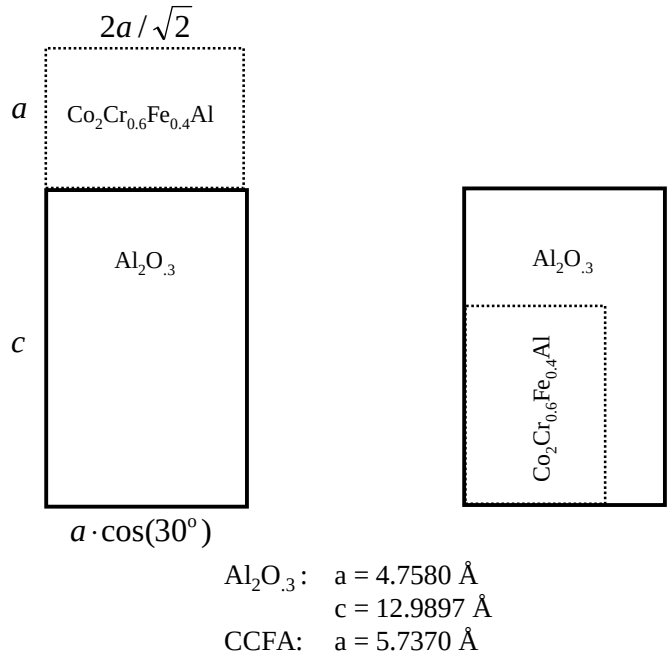

Figure 4.10: Schematic representation of the epitaxial relation between $Co_2Cr_{0.6}Fe_{0.4}Al$ and Al_2O_3 $(11\bar{2}0)$ substrate unit cells. Solid line symbolizes the projection of the Al_2O_3 unit cell, the dashed line corresponds to $Co_2Cr_{0.6}Fe_{0.4}Al$. Left panel shows the configuration with the smallest lattice mismatch. Right panel show the actually preferred growth orientation.

ering the small misfit, it was reasonable to assume this growth configuration for $Co_2Cr_{0.6}Fe_{0.4}Al$ on Al_2O_3 . However, as already observed by Jakob *et al.* by four circle diffraction, the actual growth configuration is the one presented on the right panel in fig. 4.10. Since the misfit for this configuration is much larger, interface energy reduction considerations must be adduced to explain this behavior.

The same preparation procedure was tried for direct deposition on MgO (100) substrates. Although in this case the lattice misfit is larger than in the case of Al_2O_3 or $MgAl_2O_4$, epitaxial growth was also expected. No success in this sense was achieved, $Co_2Cr_{0.6}Fe_{0.4}Al$ reflections are not present in the diffractograms. We assumed that these samples possesses a nanocrystalline nature similar to the samples deposited at low substrate temperature on Al_2O_3 (see fig. 4.2) though this point was not studied by TEM.

The difficulty to grow $Co_2Cr_{0.6}Fe_{0.4}Al$ directly on MgO substrates have been observed by other researchers as well. Matsuda, Yamamoto [93, 92] and collaborators reported epitaxial growth on MgO(100) without using metallic buffer layers. Nevertheless, in order to obtain single crystalline $Co_2Cr_{0.6}Fe_{0.4}Al$ films, a 10 nm

MgO layer is deposited using rf sputtering. Direct deposition on commercially available substrates results in films with low crystalline order. The fact that it is possible by this methode to deposite single crystalline $Co_2Cr_{0.6}Fe_{0.4}Al$ films proves that the lattice mismatch is not responsible for the lack of success in our case. The most probable reason is the presence of contaminants on the surface of the MgO substrates as already commented in section 3.2.1.

Epitaxial growth without the use of any seed layer was achieved by other groups. However, in these cases high substrate deposition temperatures were used. Kelekar and Clemens [94] deposited at temperatures above 500 °C whereas Inomata *et al.* [95] obtained epitaxial growth already at 200 °C .

4.1.5 Estimation of the degree of disorder

As pointed out in Section 2.2.1, the presence of disorder on the positions of Co and Cr atoms is detrimental to the spin polarisation. Therefore, a quantification of this kind of disorder in our films is of interest.

It has been already commented that, due to the similarity of the scattering factors of the Co and Cr atoms, an exact determination of the Co-Cr disorder level is problematic. Nevertheless, by comparing the relative intensities of the (200) and (400) reflections, $I_{(200)}$ and $I_{(400)}$ respectively, an estimation of the degree of Co-Cr disorder is possible.

The degree of the Co-Cr disorder was studied by comparing the ratio $I_{(200)}/I_{(400)}$ with the corresponding values obtained from PowderCell simulations for different degrees of disorder. However, an important difference between the simulations and the reality must be noticed. Since PowderCell is a program intended for powder samples where geometrical effects can be neglected, they are not taken into account. However, geometrical conditions have an influence on diffraction experiments on thin films. Due to the aspect ratio of a thin film, the volume of the sample contributing to the scattering intensity changes with the angle θ (angle between the incident x-ray beam and the sample surface). The situation is schematically illustrated in fig. 4.11. The red cylinder represents the profile of a circular x-ray beam. The left image shows the situation for a large incident angle. When the incident angle is smaller (right) the volume of the sample which is irradiated is larger and therefore also the scattering intensity. To compensate this effect, the scattering intensities are corrected by a factor $sin(\theta)$.

The corrected ratio $I_{(200)} \cdot sin(\theta_{(200)})/I_{(400)} \cdot sin(\theta_{(400)})$ ($R_{2/4}$ hereafter) for non-

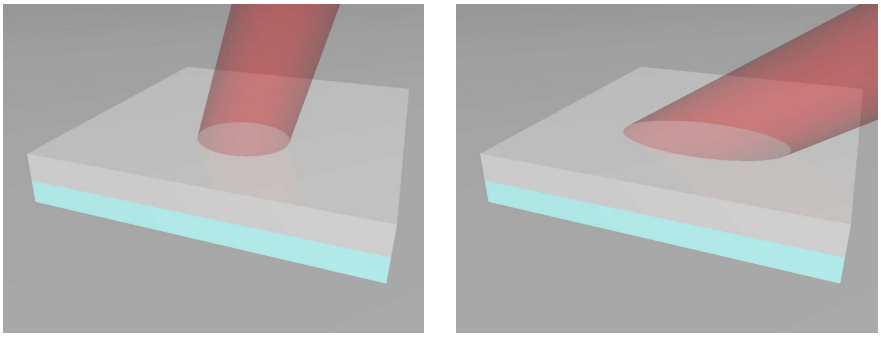

Figure 4.11: Schematic explanation of the origin of geometrical effects in measured scattering intensities in thin film diffraction experiments.

annealed samples deposited on Cr or Fe buffer layer has values around 0.06-0.09. Comparing with the simulation with PowderCell we conclude a disorder level clearly above 20% for this kind of samples. For annealed samples, $R_{2/4}$ increases up to 0.14-0.26, which is compatible with disorder levels of 20%. Thus, the annealing process has an important effect in reducing the degree of Co-Cr type disorder.

In the case of samples deposited directly on $MgAl_2O_4$, $R_{2/4}$ amounts to values near 0.25. These samples show, thus, similar level of atomic order compared with the buffered ones. Since the reflections are not visible for non annealed samples, no information about the degree of disorder before annealing is available.

For samples deposited on Al_2O_3, a comparison is not possible since the Co-Cr disorder type has no influence in the relative intensities of the (220) and (440) reflection.

Further insight in the quality of the crystalline order in the films can be gained from the width of the peaks in the $\theta/2\theta$ scans. The Debye-Scherrer equation (eq. 4.1) relates the width of the peaks with the coherence length of the films [96]. This allows to estimate the average size of the crystallites contributing to the scattering intensity.

$$L = \frac{k\,\lambda}{\Delta\theta\, cos(\theta)} \tag{4.1}$$

In the equation k is a constant (~ 0.94), λ is the x-ray wavelength and $\Delta\theta$ is the FWHM of the peak.

A real diffractometer has a finite angular resolution which is contributing also to the width of the peaks in the $\theta/2\theta$ scan. This contribution can be subtracted

	Buffer layer on MgO (100) (no annealing)	**Buffer layer on MgO (100) (+ annealing)**	**Directly on $MgAl_2O_4$ (100)**	**Directly on Al_2O_3 ($11\bar{2}0$)**
$\mathbf{R_{2/4}}$	0.06-0.09	0.14-0.26	0.24	-
Co-Cr disorder	$> 20\%$	$\sim 20\%$	$\sim 20\%$	unknown
L **(nm)**	30	50	70	50

Table 4.2: Survey of results for the estimation of the Co-Cr degree of disorder and the coherence length L for different kinds of $Co_2Cr_{0.6}Fe_{0.4}Al$ samples. The parameter $R_{2/4}$ stands for the ratio $I_{(200)} \cdot sin(\theta_{(200)})/I_{(400)} \cdot sin(\theta_{(400)})$ (see text for explanation).

by assuming that the width of the peaks from substrates reflection is a result only from this finite resolution. This is a reasonable assumption since the substrates are 10x10x1 mm single crystals and the corresponding reflections are in very good approximation a delta function. The total width of the peak can be separated in two contributions:

$$\Delta\theta = \sqrt{(\Delta\theta_{resolution})^2 + (\Delta\theta_{film})^2} \tag{4.2}$$

and $(\Delta\theta_{film})$ is what must be introduced in 4.1.

Taking into account the previous considerations, the coherence length L was calculated for some samples of each kind of them. The thickness of the selected samples is 100 nm. For samples deposited on buffer layers without thermal treatment, L amounts to values around 30 nm. This value increases with subsequent annealing up to 50 nm. Since these numbers are comparable with the thickness of the film, they are a sign of the good crystalline properties of the $Co_2Cr_{0.6}Fe_{0.4}Al$ films. On the other hand, films deposited directly on $MgAl_2O_4$ show larger coherence lengths around 70 nm. In combination with the also higher $R_{2/4}$ ratios for these films it can be concluded that the crystalline properties are better when deposited on $MgAl_2O_4$.

The coherence length can be also calculated for samples deposited on Al_2O_3, with the (110) orientation growth. As pointed out before, a small shoulder is visible on the (220) peak. Nevertheless, it is possible to use the main peak to calculate L. The obtained value is 50 nm, which is comparable with annealed

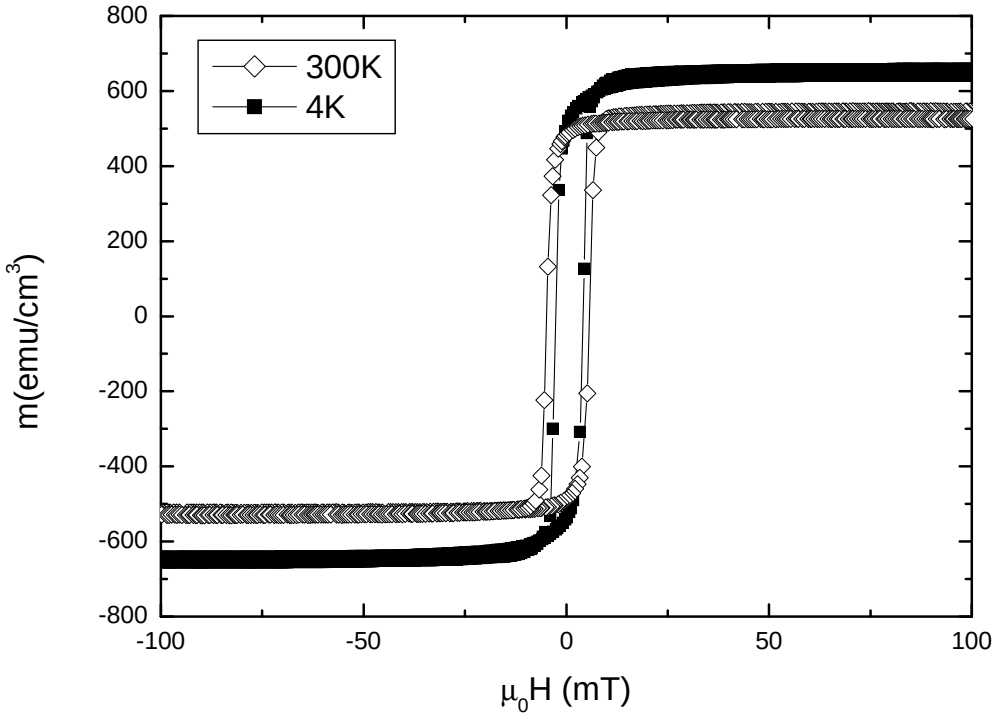

Figure 4.12: Hysteresis loops at 300 and 4 K of a polycrystalline $Co_2Cr_{0.6}Fe_{0.4}Al$ thin film deposited on Al_2O_3 at 300 °C and annealed at 450 °C for 60min. The thickness of the films is 100 nm.

samples on buffer layers. If we assume that the shoulder is a result of domains with strain at the interface CCFA/substrate, the estimated L would correspond to the strain-free top layers.

The results of the calculation of the coherence length L as well as the $R_{2/4}$ ratio and the estimated Co-Cr degree of disorder are summarized in Table 4.2.

4.2 Magnetic properties

4.2.1 Polycrystalline samples

The magnetic moment of $Co_2Cr_{0.6}Fe_{0.4}Al$ polycrystalline samples deposited at different temperatures on Al_2O_3 substrates was already measured by Jakob *et al.* [86]. They observed an increase of the magnetic moment with deposition temperature. The maximal measured magnetic moment was around $2.0\,\mu_B$/f.u. This value is smaller than the expected $3.8\,\mu_B$/f.u. for the $L2_1$ structure. This difference was attributed to the presence of Co-Cr type disorder in the films.

This disorder leads to an antiferromagnetic coupling of the Cr aroms with the Co atoms or with themselves.

The magnetic moment of the polycrystalline samples can be increased upon annealing. In fig. 4.12, the hysteresis curve of a CCFA polycrystalline thin film deposited on Al_2O_3 at 300 °C and annealed at 450 °C for 60 min is shown. The ramp speed is 2.5 °C/min. The volume magnetisation amounts to 550 emu/cm^3 at 300 K and 670 emu/cm^3 at 4 K. This values correspond to 2.8 and 3.4 μ_B/f.u., respectively. It must be pointed out that the increase in the magnetic moment is not accompanied by a change in the x-ray diffractograms, no reflection is observed after annealing. The larger magnetic moment can be tentatively explained in terms of a reduction of the degree of Co-Cr disorder inside the nanocrystallites in the film.

4.2.2 Epitaxial samples

The magnetization of the epitaxial samples on buffer layer was measured. The interference of the contribution of the buffer layer on the total magnetic moment is eliminated. For this purpose, separated samples were deposited. These samples are a Fe layer covered with 4 nm Al capping layer for protection against oxidation. The Fe buffer layer is deposited with the same parameters and thickness and the buffer layer used for $Co_2Cr_{0.6}Fe_{0.4}Al$ films. The magnetic moment of these samples, which also includes the contribution of the substrate, is subtracted from the moment of the $Co_2Cr_{0.6}Fe_{0.4}Al$ samples.

Figs. 4.13 and 4.14 show the hysteresis loops of samples deposited on Fe buffer layer without annealing and annealed at 550 °C for 5 min, respectively. For the non-annealed sample (top graph in fig. 4.13), the saturation magnetization is 2.5 μ_B/f.u. (485 emu/cm^3) at 300 K reaching 3.0 μ_B/f.u. (590 emu/cm^3) at 4 K. The correspondent values for the annealed sample are similar (fig. 4.14). The magnetization amounts to 2.5 μ_B/f.u. (495 emu/cm^3) at 300 K and 2.8 μ_B/f.u. (555 emu/cm^3) at 4 K.

In both cases, the volume magnetization is smaller than in the annealed polycrystalline samples. Since the degree of Co-Cr disorder is not known in the polycrystalline films, it is not possible to elucidate a correlation between ordering and saturation magnetization. If the largest magnetisation of the annealed polycrystalline samples is a result of a reduced Co-Cr degree of disorder and since this kind is detrimental to the spin polarisation, it could be concluded that the

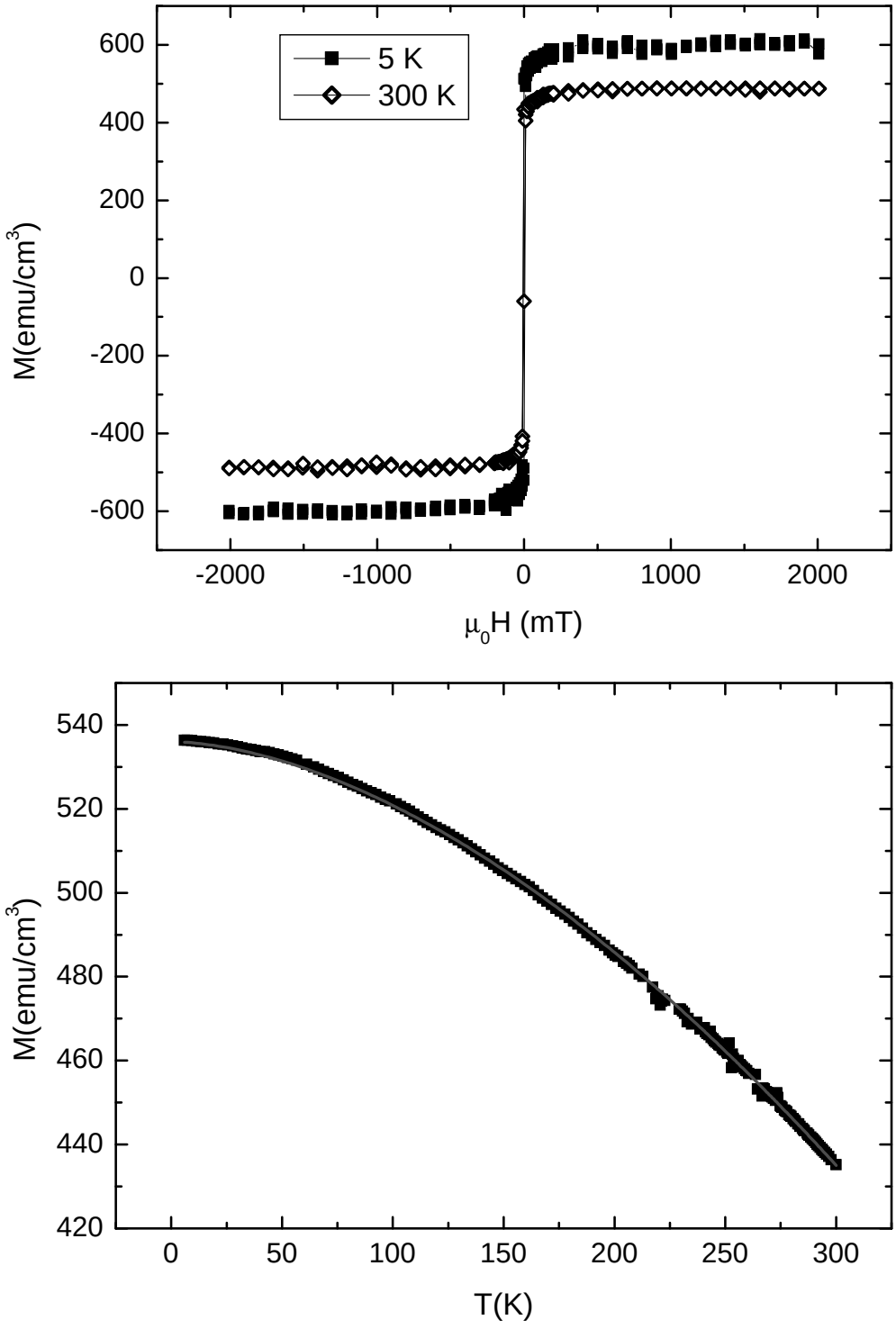

Figure 4.13: Top: Hysteresis curves at 300 and 4 K of a 100 nm thick CCFA sample deposited at 100 °C on Fe buffer layer on MgO (100) without annealing. Bottom: Dependence of the magnetization at 20 mT on the temperature. The grey line is a fit with a power law with $\beta = 1.72$ (see text).

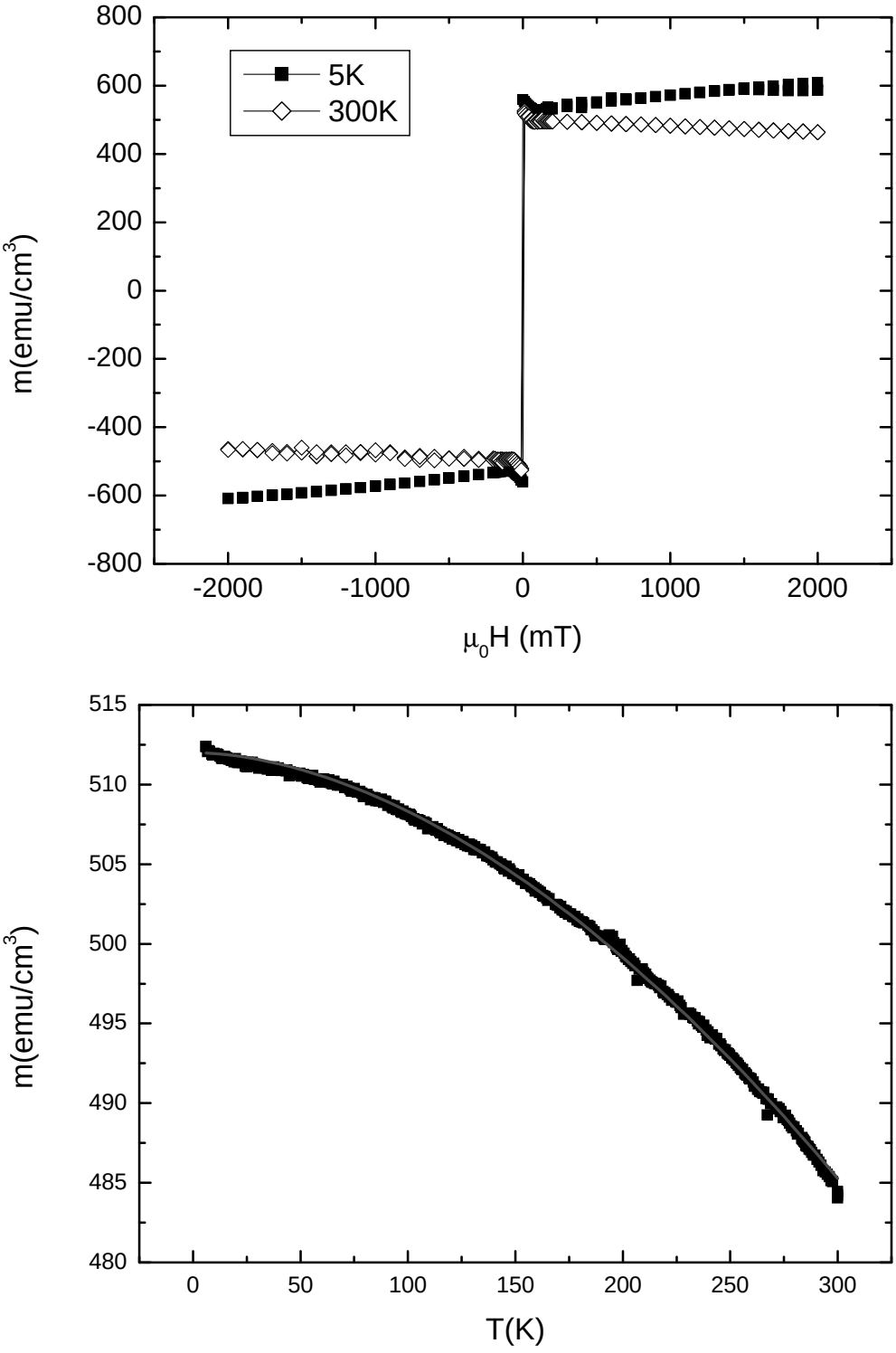

Figure 4.14: Top: Hysteresis curves at 300 and 4 K of a 100 nm thick CCFA sample deposited at 100 °C on Fe buffer layer on MgO (100) and annealed at 550 °C for 5min. Bottom: Dependence of the magnetization at 20 mT on the temperature. The grey line is a fit with a power law with $\beta = 1.80$ (see text).

polycrystalline annealed samples would be more suitable to achieve high TMR ratios. This issue will be studied in Chapter 5.

The bottom panels in figs. 4.12 and 4.14 show the dependence of the volume magnetization on the temperature at a field of 20 mT. The grey line is a fit to a power law with the form

$$m(T) = m(0)(1 - kT^{\beta}) \tag{4.3}$$

Assuming the classical spin wave picture, the Bloch law with $\beta = 3/2$ is deduced. However, for our samples, larger exponent values between 1.7 and 1.8 are measured. Similar exponent values have been reported for bulk samples of the full-Heusler compound Co_2FeSi. However, the exponent value reduces to 3/2 for thin films of the same compound [97]. Conventional ferromagnets like bcc Fe [98] or fcc Ni [99] do also not follow Bloch's law but a power law with $\beta = 2$. On the other hand, a $T^{3/2}$ law describes well the behaviour of amorphous samples of Co [100], NiFe alloys [101] and Fe [102]. As pointed out by Köbler [103], this is surprising since the Bloch spin wave theory requires a translational symmetry of the magnetic lattice which is not present in amorphous compounds. The coincidence between theory an experiment in this case can be described as accidental. These examples illustrates the limitations of the classical spin wave picture.

4.2.3 XMCD and XAS results

X-Rays magnetic circular dichroism (XMCD) and the X-Rays absorption spectroscopy (XAS) are two powerful tools for the study of element-specific magnetic moments in $Co_2Cr_{0.6}Fe_{0.4}Al$ films. Additionally, in combination with the measurement of the total electron yield (TEY), information concerning the magnetic properties of the surface of the films is gained. The TEY technique measures the photoemitted electrons from the sample, the escape depth for these low energy electrons is limited to about 25 Å, taking into account the existence of an Al capping layer in our films.

The possibility of measuring independently the magnetic moment of the different chemical constituents is of special interest for the case of the Cr atoms. The occupation of the Co atomic sites by Cr atoms results in an antiferromagnetic coupling with the other Cr atoms. Thus, a reduction of the Cr averaged magnetic moment is an indication of a large amount of Co-Cr type disorder, detrimental

to the spin polarisation.

Unfortunately, the estimation of the absolute Cr moments is not straightforward since the correspondent electronic transitions are not well separated. As a consequence, the application of the sum rules to this element generates and underestimated value. This is a general property of the light 3d transition metals [104].

Several selected samples of two different families of samples were analyzed. The first family was presented in Section 4.2.1. They are polycrystalline films deposited on Al_2O_3 substrates and annealed at 450 °C . These samples posses the highest volume magnetization. The other family consists on epitaxial films deposited at 100 °C on buffer layers without annealing. The results are reported by Kallmayer *et al.* in [105] in combination with results from bulk samples.

A correlation between the magnetic moments and the structural ordering is found. The epitaxial samples show increased magnetic moments, the increase is most pronounced in the case of the Cr atoms. This is compatible with a reduced Co-Cr disorder in these films compared with the polycrystalline ones. This corroborates also the observed decrease in the disorder by x-ray diffraction (Table 4.2).

In a previous work on annealed polycrystalline films, a reduction of the magnetic moments at the surface of the films was observed [106]. This reduction was estimated in 17% compared to the values in the bulk. Three possible explanations can be given for this behavior: a result of structural defects at the surface, termination effect or to Al interdiffusion from the capping layer. The last possibility is very improbable, since no thermal treatment is done after the deposition of the capping layer. The termination effect is a result of the missing atomic neighbours *even in ordered surfaces*.

It was pointed out that the high reactivity of Cr with oxygen may be problematic in order to deposit $Co_2Cr_{0.6}Fe_{0.4}Al$ thin films. This effect was evidenced by measurements on polished bulk samples. Elmers *et al.* [107] observed a strong selective Cr oxidation at the surface of the samples due to exposition to air. Nevertheless, the measurements from Kallmayer *et al.* indicate clearly the absence of Cr oxidation in our thin films.

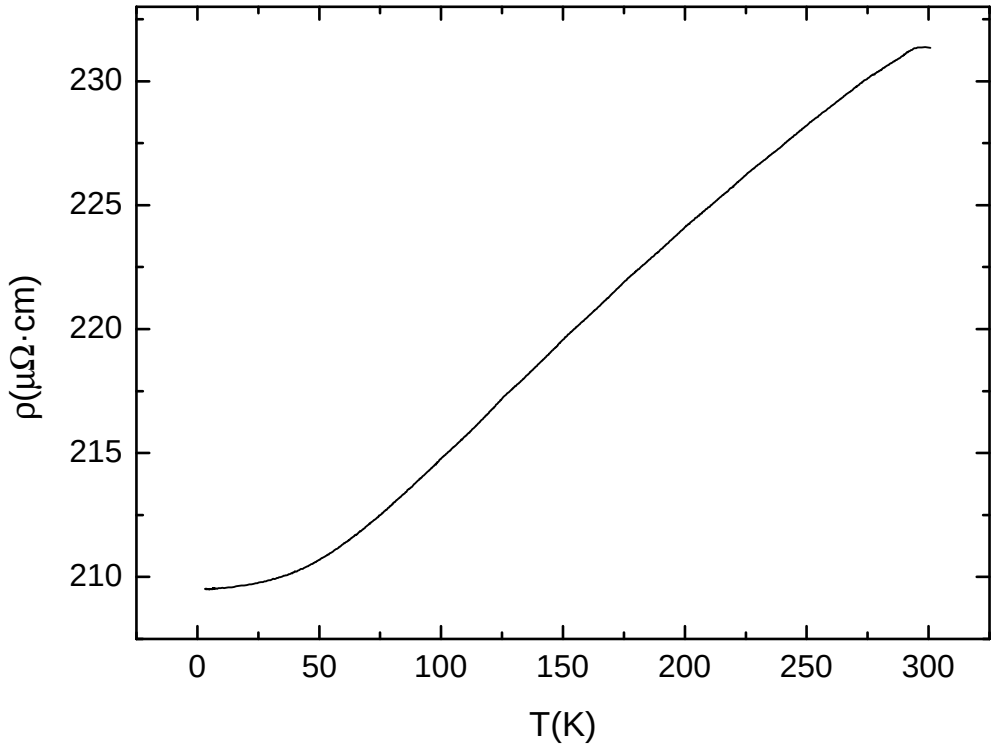

Figure 4.15: Resistance versus temperature measured for a $Co_2Cr_{0.6}Fe_{0.4}Al$ thin film with a thickness of 100 nm deposited on a $MgAl_2O_4$ (100) substrate.

4.3 Transport properties

The presence of good conducting Fe or Cr layers prevents any transport measurement on samples deposited on buffer layers. Therefore, we perform such measurements only on samples deposited on $MgAl_2O_4$, in this case the films are (100) oriented. The samples were not structured and the van der Pauw method [108] was applied to extract the specific resistivity of the film.

The dependence of the specific resistivity on the temperature is shown in fig. 4.15. In previous work of Jakob *et al.* an upturn in the resistivity below 60 K is observed for epitaxial samples. The residual resistance ratio of the films from Jakob was 1.02. In our samples, no upturn is visible and the residual resistance ratio is increased up to 1.10. In combination with the overall smaller resistivity, we conclude that these films posses an increased electronic mean free path due to better crystalline ordering. The low residual resistance ratios are a common property of many Heusler compounds.

Recently, Schneider *et al.* reported the presence of a small anisotropic mag-

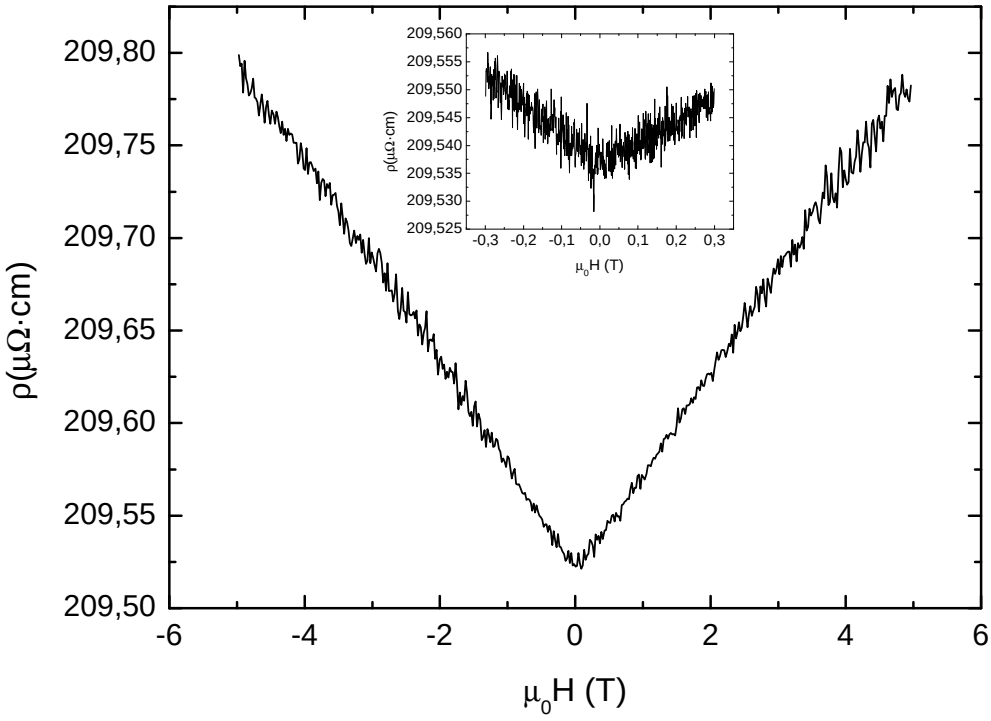

Figure 4.16: Specific resistivity at 4 K versus magnetic field measured for a $Co_2Cr_{0.6}Fe_{0.4}Al$ thin film with a thickness of 100 nm deposited on a $MgAl_2O_4$ (100) substrate.

netoresistive effect (AMR) below saturation in thin epitaxial films of Co_2FeSi [97, 109]. The presence of an AMR effect is attributed to a presence of *s-d* scattering in the films. Since *s* bands should not exist if a gap is present, the observation of the AMR effect is an indication of a loss of the half-metallicity in those films. Additionally, for larger fields a linear decrease in the resistivity is observed which may be related to a reduction of spin-flips scattering induced by damping of spin waves at high fields [110].

The same measurements were also carried out in our $Co_2Cr_{0.6}Fe_{0.4}Al$ samples. The dependence of the specific resistance on the magnetic field at 4 K show a very different behavior as shown in fig. 4.16. No AMR is visible at small magnetic fields below saturation[1]. This region is shown in detail in the inset. In contrast with results from Co_2FeSi films, an increase of the resistivity with magnetic field is observed. The increase is linear with a slope of 55 $n\Omega \cdot cm/T$.

[1]Strictly speaking, in order to estimate the AMR efffect two measurements with different orientations (I||H and I⊥H) should be performed. However, when the AMR effect is present, an abbrupt change in the resistance at very low fields is present. This change is due to the re-orientation of the magnetic domains following the magnetic field.

The increase of the specific resistivity can be tentatively explained as a *normal magnetoresistance* effect. This effect is a consequence of the Lorentz force caused by the magnetic field on the moving electrons and obeys the Kohler law [111]:

$$\frac{\Delta\rho}{\rho} = F\left(\frac{B}{\rho_0}\right) \tag{4.4}$$

where ρ_0 is the specific resistivity a zero field. When the specific resistivity is large, the normal magnetoresistance effect becomes very small. In fact, from 0 to 5 Tesla, the effect in our samples is roughly 0.1%.

In conclusion, the absence of a measurable AMR signal and the positive slope of the magnetoresistance at high fields are indications of reduced *s-d* scattering and spin-flip magnon-mediated scattering, respectively.

4.4 Surface ordering and topology

In tunneling devices, the interfaces play a crucial role in the transport properties of a junction. Therefore, information about the last atomic layers of the $Co_2Cr_{0.6}Fe_{0.4}Al$ films must be obtained. In this sense, as well the crystalline order of the surface of the film as its topology are of importance. The prediction of half-metallicity is valid only for ordered structures, thus disorder at the surface may reduce the spin polarisation of the tunneling current and consequently the TMR ratio. On the other hand, the small thickness of the insulating barrier requires a smooth surface to reduce pinholes defects which result in leaking direct currents. Additionally, increased interface roughness may raise also the number of scattering processes.

The morphology of the $Co_2Cr_{0.6}Fe_{0.4}Al$ samples is studied by in-situ STM. The crystalline order is studied by RHEED (Reflection High Energy Electron Diffraction) and LEED (Low Energy Electron Diffraction). Both methods are only surface sensitive.

In the case of RHEED, typical electron energies are between 5-100 keV and the angle between the incident electron beam direction and the film surface is smaller than 5°. On the contrary, in a LEED system the energies are below 1 keV and the beam incident direction is perpendicular to the surface. In both cases, the electron cannot penetrate deep in the volume of the film and therefore only information from the surface is obtained. Further insight in the RHEED and LEED methods can be found in [112] and [113], respectively.

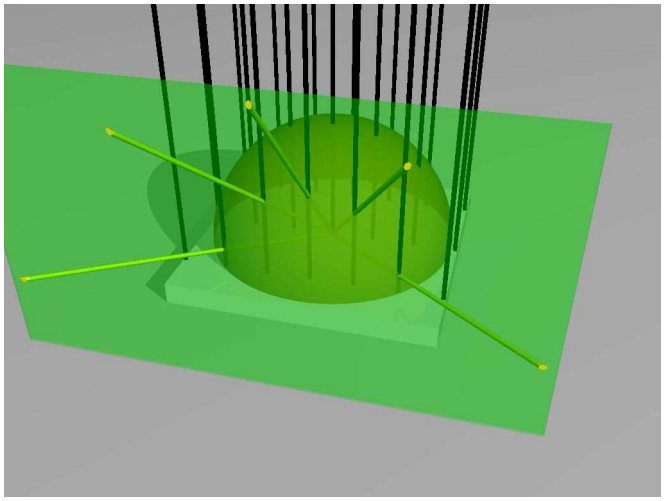

Figure 4.17: Schematic representation of a RHEED experiment. For a 2D lattice, the reciprocal lattice degenerates in infinite rods perpendicular to the film surface (black lines). The sphere represents the Ewald sphere. The projection of the intersection of the Ewald sphere with the infinite rods on the phosphorescent screen gives the RHEED pattern (yellow points in the green screen).

Since only a few atomic layers contribute to the diffraction pattern, it is possible to assume a 2-D system. In this case the reciprocal lattice degenerates in a lattice of infinite rods perpendicular to the surface (see fig. 4.17). The projection of the intersection of these rods with the Ewald sphere forms the diffraction pattern observed in a phosphorescent screen. In the case of a RHEED system, where electron gun and screen are at the sides of the sample, the resulting diffraction pattern is an array of points situated in different circumferences corresponding to the different diffraction orders. In a LEED system, the electron gun and the screen are situated above the sample and the diffraction pattern observed in the screen has the same symmetry as the film surface. The interpretation of LEED patterns is, thus, straightforward[2]. The interpretation of RHEED patterns is more complicated because, due to the grazing incidence angle, RHEED is in addition sensitive to surface roughness. On the other hand, this last property makes RHEED more interesting to characterize surface roughness. We can conclude that both systems are complementary for the study of surface properties.

In the bottom picture of fig. 4.18, a typical RHEED diffraction pattern of a $Co_2Cr_{0.6}Fe_{0.4}Al$ film deposited on Fe buffer layer and annealed at 550 °C for

[2]Actually, more information can be obtained by measuring the intensities of the different reflections. However, the available experimental setup does not allow this possibility.

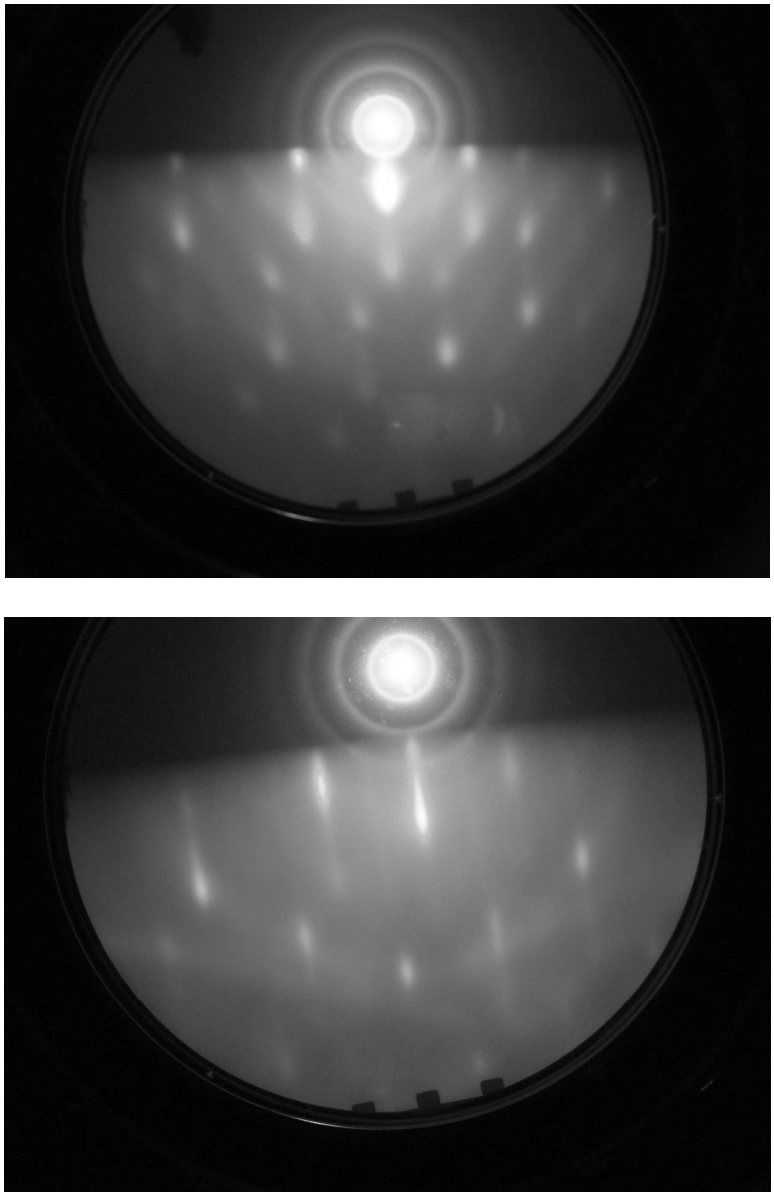

Figure 4.18: Top: RHEED diffraction pattern for an as-deposited $Co_2Cr_{0.6}Fe_{0.4}Al$ thin film on a 100 nm thick Fe buffer layer. The deposition temperature for $Co_2Cr_{0.6}Fe_{0.4}Al$ is 100 °C. The pattern is typical for a 3D lattice, indicating a relatively rough surface (see text). Bottom: RHEED pattern from a similar sample after annealing at 550 °C for 5 min. Typical 2D circular configuration of the reflections is seen. Additionally, Kikuchi lines are visible. The energy of the electron beam is 20 keV for both images.

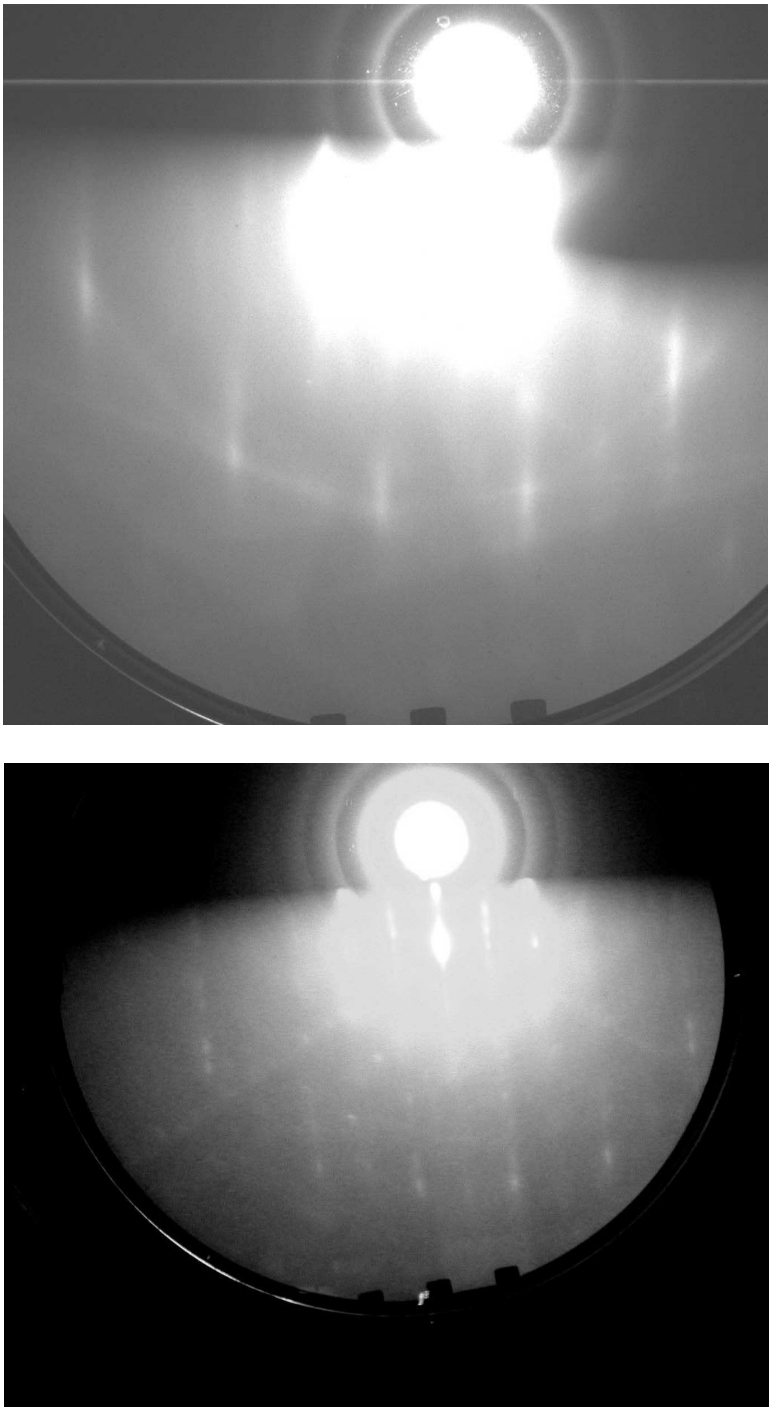

Figure 4.19: Top: RHEED pattern of a CCFA thin film deposited on a $MgAl_2O_4$ (100) substrate at 100 °C and annealed at 600 °C. Bottom: RHEED pattern of a CCFA thin film deposited on an Al_2O_3 $(11\bar{2}0)$ substrate and annealed at 600 °C. Both films have a thickness of 100 nm. The energy of the electron beam is 20 keV for both images.

5 min is shown. The bright point on top is the direct non-diffracted beam. It is possible to see the circular configuration of the reflections of the different diffraction orders (the last diffraction order is at the border of the phosphorescent screen, some points are already not visible).

A detailed inspection of the images shows that the reflections are not exactly punctual but they have a linear shape. There are two reasons for this. First of all, there is always a certain energy dispersion for the incidents electrons, i.e. the beam is not completely monochromatic. As a consequence the Ewald sphere degenerates in a spheric shell and the intersection with the rods is no more a point. Second reason lays in the mosaicity of the surface. The rods are no more unidimensional and the width increases with the distance to the surface. Again, the intersection with the Ewald sphere does not result in points.

Additional linear structures can be observed in this picture. They are the so-called Kikuchi lines [112]. They are explained by a two-step scattering model. The incident electrons suffer first a scattering process and as a result the direction of their wave vectors is isotropically randomized. At this point a quasi-elastic process is assumed so that the energy loss is minimum and we can consider that the electrons have still the initial energy. The Kikuchi line appears as a result of the diffraction generated by the isotropical radiation from the scattering points. In order to observe a well-defined line, the energy spread in the first scattering process must be very small. Since the Kikuchi lines can be interpreted as the diffraction pattern of electrons traveling on a 2D surface, their presence can be taken as an indication of a good ordered film surface.

On the top image of fig. 4.18, the pattern for an as-deposited $Co_2Cr_{0.6}Fe_{0.4}Al$ film deposited on a Fe buffer layer is shown. The pattern looks different from the one from annealed samples. The reflections points are not arranged in circles. This is the kind of diffraction pattern expected for a 3D lattice. This is interpreted as a result of an increased roughness of this surface compared to the annealed films.

In fig. 4.19, the correspondent RHEED pattern of annealed samples deposited on $MgAl_2O_4$ and Al_2O_3 are shown. In both cases, the RHEED reflections are sharper that in the case of films deposited on buffer layers. Again, Kikuchi lines are clearly visible. In contrast with the previous case, for non annealed samples deposited directly on these substrates, no diffraction pattern is observed. This points to highly disordered surfaces in the as-deposited case. This behavior is in concordance with the observations by x-ray diffraction. As already commented,

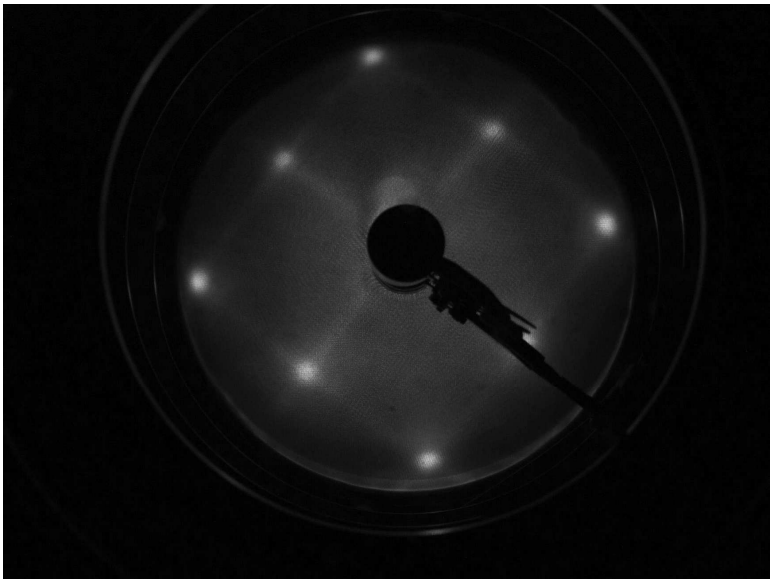

Figure 4.20: LEED diffraction pattern for a $Co_2Cr_{0.6}Fe_{0.4}Al$ film deposited on Fe buffer layer and annealed at 550 °C for 5 min. The energy of the electron is 120 eV.

the annealing step is needed to induce crystalline order in samples deposited directly on $MgAl_2O_4$ and Al_2O_3.

Alternatively, LEED diffraction patterns were measured for some selected samples. In fig. 4.20 a LEED pattern of a $Co_2Cr_{0.6}Fe_{0.4}Al$ film deposited on Fe buffer layers and annealed at 550 °C for 5 min is shown. The four-fould symmetry of the $Co_2Cr_{0.6}Fe_{0.4}Al$ (100) surface is recognized in the pattern.

The morphology of the films was analyzed by in-situ STM. In figs. 4.21 and 4.22, STM scans for three samples deposited at 100, 400 and 550 °C on Fe buffer layers are shown. These samples were not annealed. The bright spots present in the case of the sample deposited at 100 °C are probably particles present in the substrate prior to loading in the deposition chamber. These spots are not representative since they only appeared in this sample. A weak tendency to increased roughness with increasing deposition temperature can be seen but in any case the root mean square roughness (rms) is always below 1 nm. The tendency is more evident by observing the corresponding height profiles. The advantage of using a buffer layer to obtain smooth epitaxial films is here evident, especially when compared with the previous work of Jakob *et al.* [86].

The corresponding scans for annealed films are shown in fig. 4.23. The annealing temperature is 550 °C for the top image and 600 °C for the bottom one.

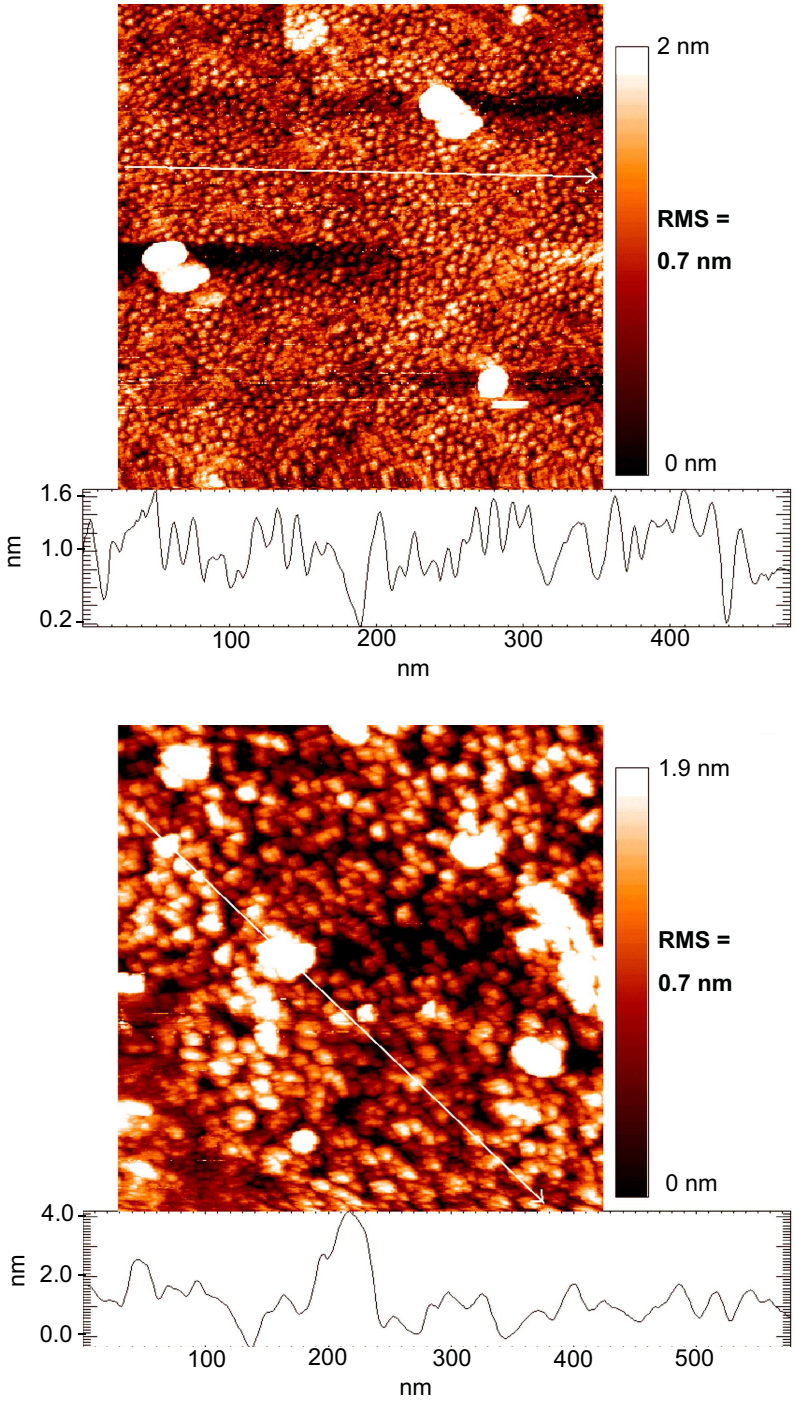

Figure 4.21: STM images of 100 nm thin $Co_2Cr_{0.6}Fe_{0.4}Al$ films deposited at 100 °C (top) and 400 °C (bottom) on Fe buffer layer on a MgO (100) substrate.

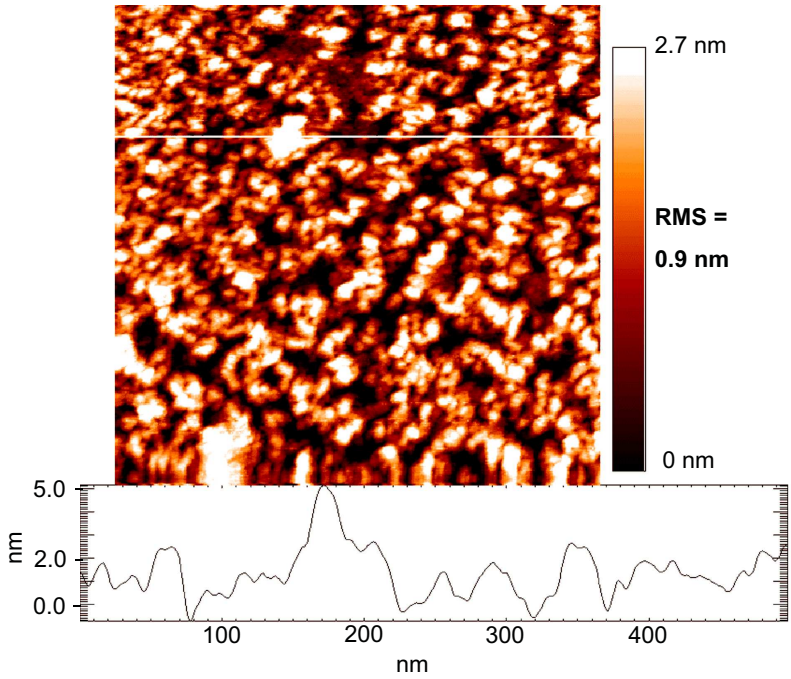

Figure 4.22: STM image of 100 nm thin $Co_2Cr_{0.6}Fe_{0.4}Al$ film deposited at 550 °C on Fe buffer layer on a MgO (100) substrate.

The annealed films show increased roughness in comparison with as-deposited ones. Nevertheless, also in this case the roughness is small enough to allow the deposition of a tunneling barrier. The differences in roughness between samples deposited at 550 and 600 °C are small. The fact that the sample annealed at lower temperatures has lower rms is probably due to the statistical deviations from sample to sample.

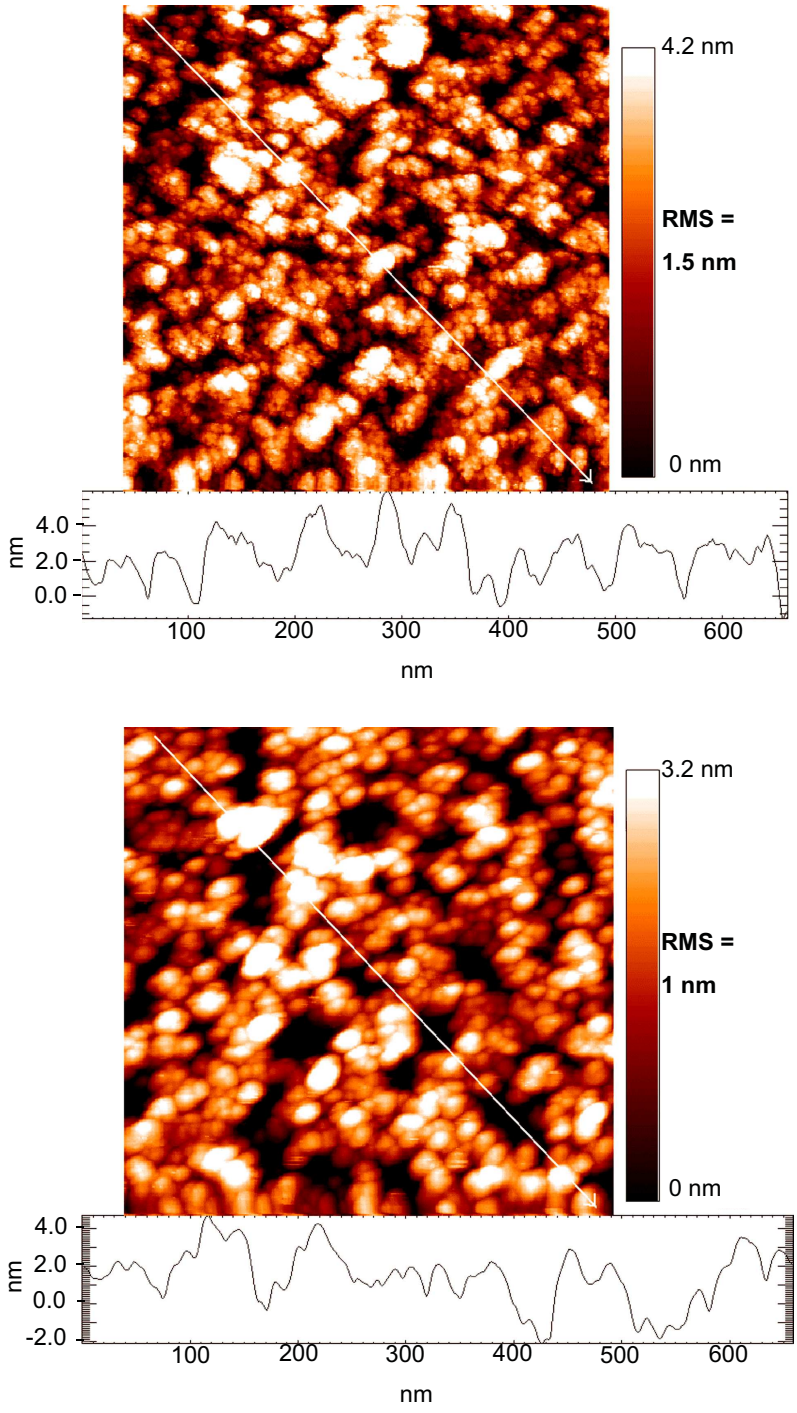

Figure 4.23: STM images of 100 nm thin $Co_2Cr_{0.6}Fe_{0.4}Al$ films deposited at 100 °C on Fe buffer layer on a MgO (100) substrate and annealed at 550 °C (top) and 600 °C (bottom).

Chapter 5

Magnetic tunneling junctions

5.1 Exchange bias

In order to measure the TMR effect, it is essential to be able to assure an antiparallel configuration of the magnetization of both electrodes. In materials with very different coercive fields, it is possible to obtain an separated rotation of both magntizations at different magnetic field values. However, this is not the case for many of the most used ferromagnets.

The low TMR values reported in our first work [114] is explained by an incomplete antiparallel configuration. The TMR amounted to a maximal value of 12% at 4 K. No antiferromagnetic layer was used to pin the magnetization in that case. In fig. 5.1, top, the magnetic hysteresis loop of a CCFA/AlO_x/Co is shown. The measurement was done with a SQUID magnetometer. It is not possible to distinguish a separated switching of the magnetization of the electrodes. By comparison with $Co_2Cr_{0.6}Fe_{0.4}Al$ thin films it was possible to conclude that the first electrode to switch is the $Co_2Cr_{0.6}Fe_{0.4}Al$ bottom electrode but the top Co electrode starts to switch before the magnetization reversal in $Co_2Cr_{0.6}Fe_{0.4}Al$ is completed.

In order to solve this problem, FeMn and CoO antiferromagnetic layers were deposited with different success. With both materials it is possible to bias the hysteresis loop of the Co top electrode to higher fields but the effect was not strong enough for the case of FeMn. This is shown in fig. 5.2. Here the TMR major loops of two MTJ pinned with FeMn and CoO are plotted. The arrows indicate the direction of the measurement starting from high positive fields. For the case of CoO a true plateau is recognized indicating the achievement of a

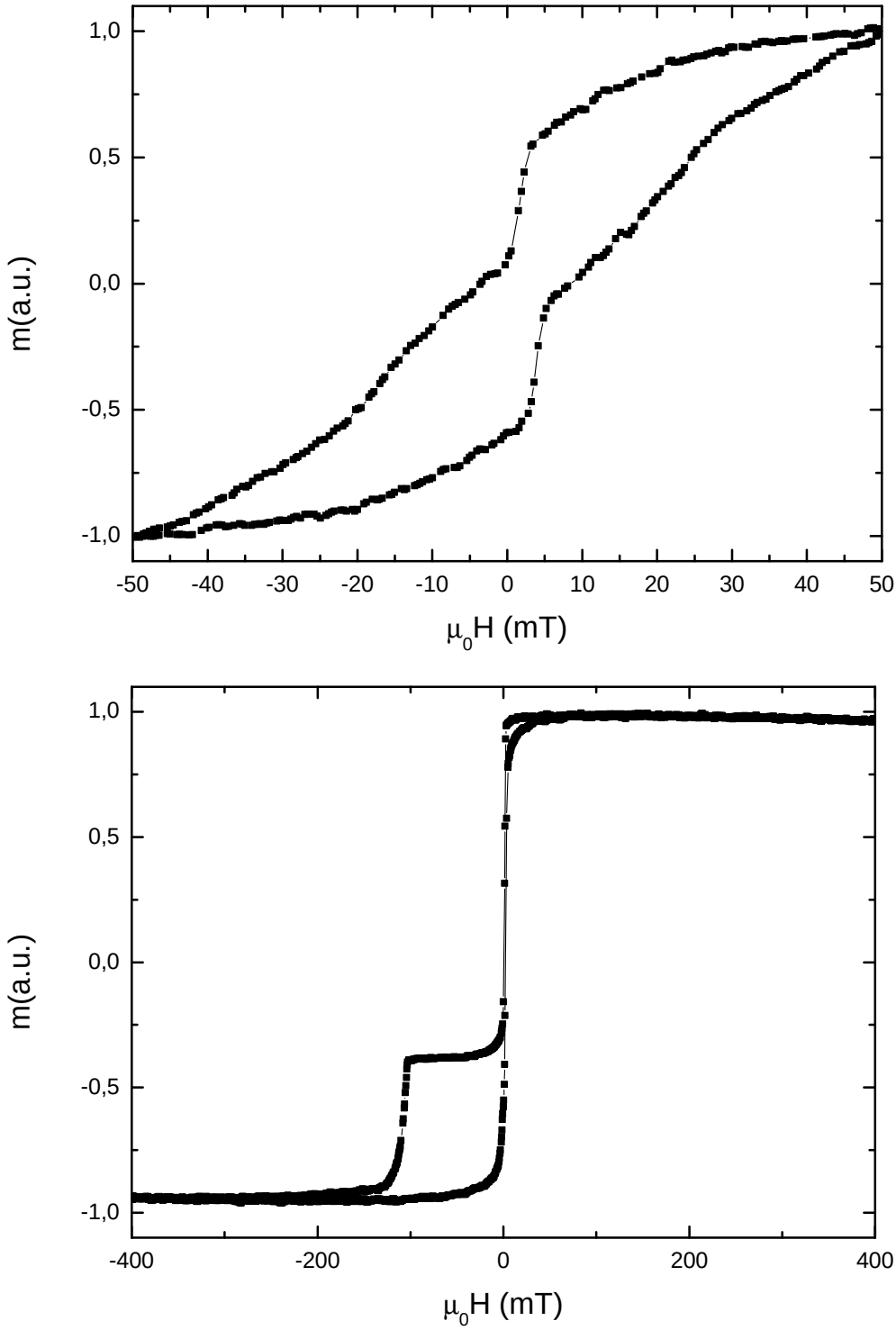

Figure 5.1: Top: Hysteresis curve at 4 K of a CCFA/AlO_x/Co multilayer sample. An independent rotation of the magnetizations is not observed. Bottom: Hysteresis curve at 4 K of a CCFA/AlO_x/Co/CoO multilayer sample. The plateau indicates a true antiparallel configuration with independent switching of the magnetization.

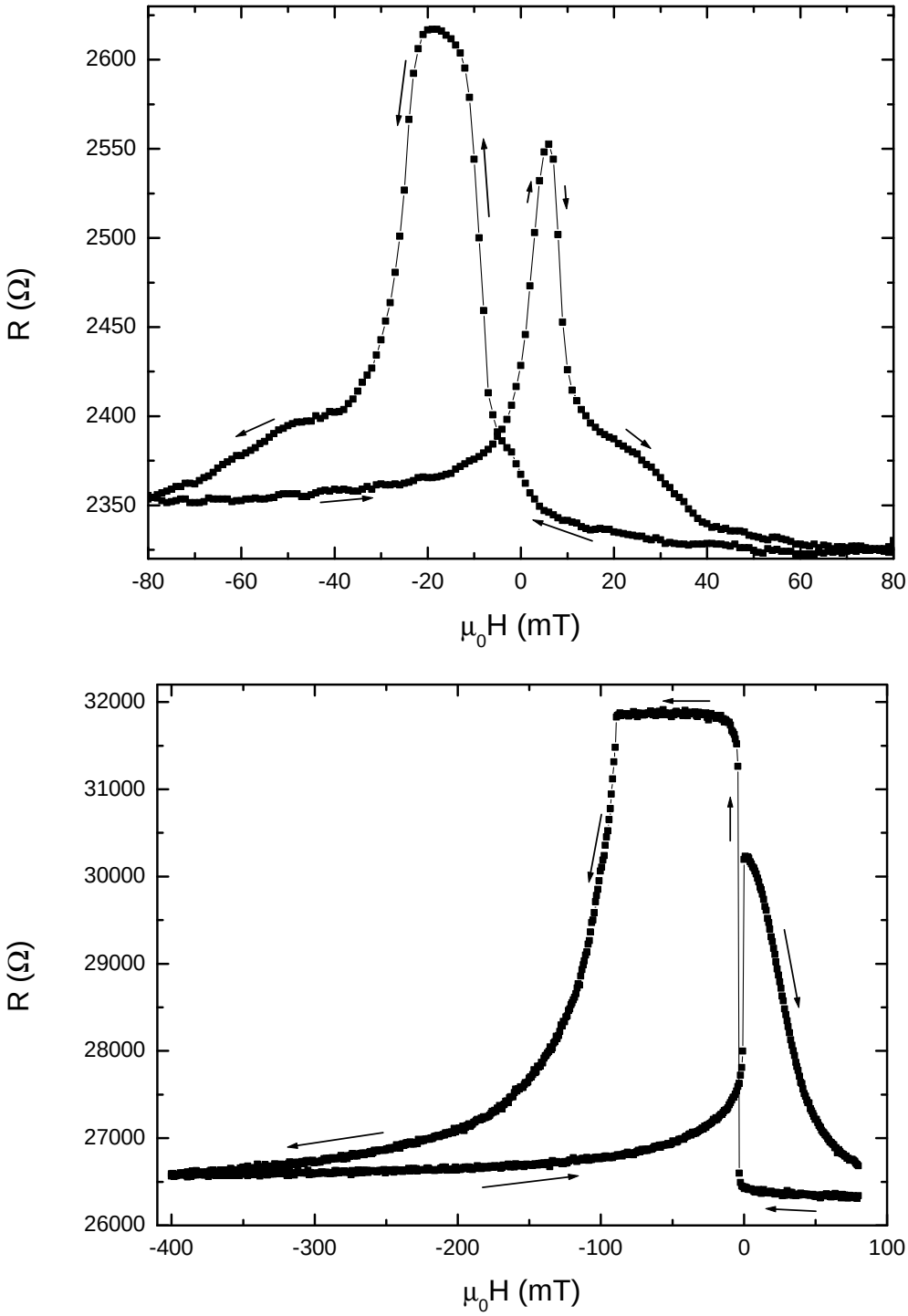

Figure 5.2: Major magnetoresistance loops for a MTJ pinned with 10 nm of FeMn (top) and CoO formed by oxidation of the previously deposited Co electrode (bottom).

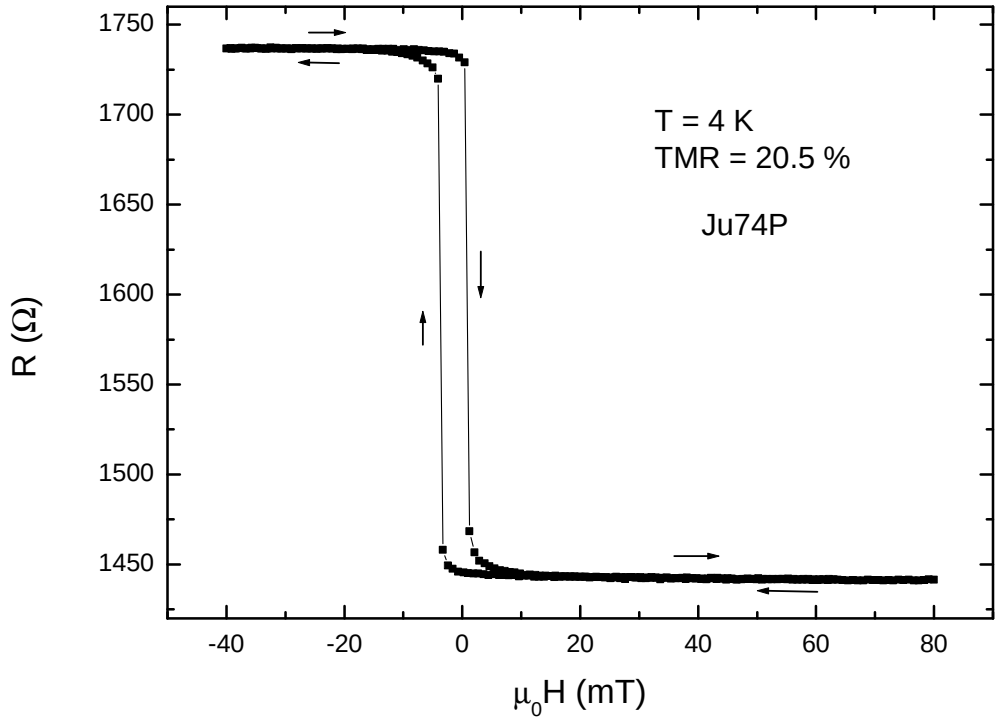

Figure 5.3: Minor loop magnetoresistance curve of a CCFA/AlO_x/Co/CoO polycrystalline sample. The Al barrier has a thickness of 1.5-2 nm and the oxidation time is 75 s in a pure oxygen atmosphere plasma.

complete antiparallel configuration. This is not the case for FeMn.

The independent rotation of the magnetization of both electrodes can be also seen in the magnetic hysteresis loops of a CCFA/AlO_x/Co/CoO sample shown in the bottom graph of fig. 5.1. A plateau is easily recognizable as a result of the different switching fields for the ferromagnetic layers.

The lack of success in the case of FeMn could be attributed to the lower interface exchange energy in comparison with CoO as shown in Table 3.1. But it may be also a result of the different field cooling procedures used for both antiferromagnets as described in Section 3.2.3. Especially, the low magnetic field applied for the case of FeMn may play an important role.

5.2 TMR of polycrystalline samples

Most of the results concerning TMR ratios of MTJ's with polycrystalline $Co_2Cr_{0.6}Fe_{0.4}Al$ films were not obtained from samples patterned with MESA structures but by

using cross-geometry junctions deposited using shadow masks.

Some remarks must be made about the values of the thickness of the barriers given in this work. The thickness of the metallic Al layers is known always once the deposition rate has been measured. However, when Al is oxidized there is an increase in the volume as result of the change in the crystalline structure. By comparing the volume per Al atom for Al and Al_2O_3 the change in the volume can be estimated. In this discussion, the parameter of interest is the change in one dimension since we are interested in the barrier thickness. The lineal change is estimated in 26% for amorph materials. However, this value corresponds to bulk stoichiometric samples. In a tunneling barrier this effect depends on the oxidation conditions and therefore there is a certain uncertainty in the final thickness of the insulating barrier. In order to compare samples, only the nominal thickness of the Al layer is given. The nominal thickness and the oxidation time are the only parameters of interest to characterize a barrier[1]. In the literature, this is the normal criterion. Only with a TEM it is possible to estimate the actual thickness of the barrier.

The TMR values of junctions with polycrystalline electrodes vary between 20 and 27%. In fig. 5.3 the minor loop of a CCFA/AlO_x/Co/CoO sample is shown. The barrier thickness is 1.5-2 nm and the oxidation time in pure oxygen is 75 s. During a minor loop measurement the fields are kept small and only the non-pinned CCFA magnetization rotates. The hysteresis in the magnetoresistance curve is thus a reflection of the magnetic hysteresis of the CCFA electrode. This measurement takes much less time than a major loop and it will be used hereafter to measure TMR ratios[2].

The TMR values of polycrystalline samples show a weak tendency to increased values with reduced oxidation times. The TMR ratios at 4 K are 20.5%, 23.7% and 27.9% for oxidation times with pure oxygen of 75, 45 and 30 s, respectively.

[1]This is of course only true if the oxygen pressure, the temperature of the sample during oxidation and the current generating the plasma are always constant. In this work the oxidation was always done at room temperature and the current was always 10 mA. The pressure was 0.2 mbar. Pure oxygen or a mixture of argon and oxygen were used. The kind of atmosphere will be indicated for each case.

[2]There is an additional important reason to use minor loops measurements. In the exchange bias a training effect is observed. That means that once the Co pinned magnetization is rotated in one measurememt (with a high field), the exchange bias is no longer as strong as before. With further measurements it may be insufficient to assure an AP configuration. By switching only the CCFA magnetization, this problem is avoid.

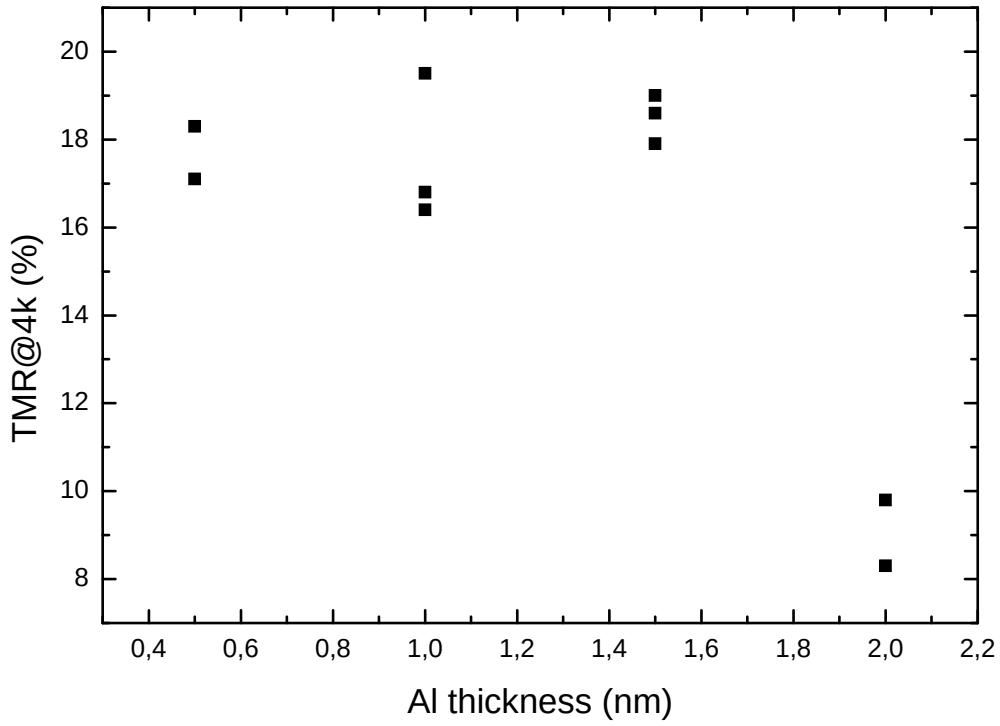

Figure 5.4: Dependence of the TMR ratio on the Al thickness for polycrystalline samples. The oxidation time for this series is 150 s in a pure oxygen atmosphere.

In order to compare the resistances for tunneling junctions with different sizes, the product resistance times area (RS or RA) is commonly used in the literature. The reduction of the oxidation times is reflected also in the value of the resistance, which becomes smaller with decreasing oxidation times. The RS products are 51, 3.2 and 0.7 $\mathrm{M}\Omega \cdot \mu\mathrm{m}^2$ for oxidation times of 75, 45 and 30 s.

An improvement of the TMR values by varying the thickness of the barrier is not possible. In fig. 5.4, the dependence of the TMR ratio at 4 K on the Al thickness is shown for an oxidation time of 150 s. A plateau where almost no changes in the TMR values can be recognized. With thicker barriers a reduction of the TMR is observed, probably due to the presence of a non-oxidized Al layer at the interface. Astonishingly, the TMR plateau holds for relative small thicknesses. A this point we must remember that the thickness of the barrier is larger than the nominal Al thickness. On the other hand, later measurements of the Al deposition rates indicated a slight underestimation of the Al thicknesses.

Further reduction in the oxidation time in cross geometry samples is not possible without the risk of geometrical enhancement of the TMR ratio. As already

pointed by van der Veerdonk and Moodera [115, 116], when the resistance of the junction becomes comparable to the longitudinal resistance of the electrode, the current distribution becomes inhomogeneous. This results in an ill-defined measurement and in a non-realistic value of the TMR. This effect is of special importance in magnetic tunneling junctions with electrode materials with large specific resistivity, as it is the case of $Co_2Cr_{0.6}Fe_{0.4}Al$ ($\rho_o = 210\,\mu$m·cm). In consequence, a further reduction of the junction area, achievable only with MESA structures, is needed. Additionally, when the oxidation time becomes smaller and smaller, it becomes difficult to adjust it exactly resulting in reduced reproducibility. For this reason, the mixture Ar-O_2 is used hereafter.

5.3 TMR in samples with epitaxial $Co_2Cr_{0.6}Fe_{0.4}Al$ electrode

5.3.1 Annealing temperature dependence

In Chapter 4, the improvement of the crystalline properties of the thin films by annealing and of the order in the surface is discussed. It is reasonable to think that this would have an effect also in the TMR values.

The TMR ratio results from samples annealed at different temperatures are plotted in fig. 5.5 for a barrier thickness of 3 nm. The points at 50 °C represent non-annealed samples. The lines are only a guide to the eye. In this graph, two different sample series with oxidation times of 120 and 90 s are shown. All the samples are oxidized in a mixture argon-oxygen and the annealing time is fixed at 5 min.

No change is observed between as deposited samples and annealed samples with annealing temperatures up to 500 °C. An abrupt increase in the TMR is observed for annealing temperatures above 500 °C reaching a maximum at 550 °C. Further increase of the annealing temperature results in a fast decrease in the TMR, already visible at 575 °C.

Some words must be said about the reproducibility of this results. Typically the TMR values obtained from different junctions prepared at the same conditions scatter in a range of ±2% around a mean value. Sporadic strongly reduced TMR values can be associated with problems in the patterning process.

A maximal TMR ratio of 40.7% at 4 K (34.6% at 77 K) is measured (see

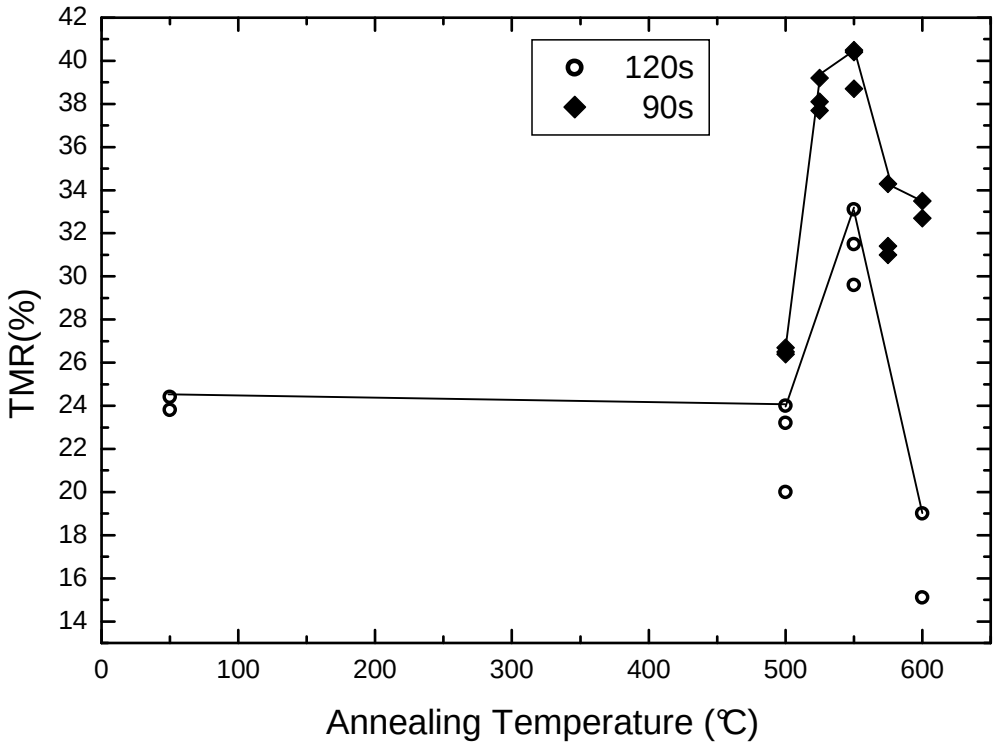

Figure 5.5: Dependence of the TMR ratio on the annealing temperature for samples deposited on Fe buffer layer on MgO(100) substrates. The lines are a guide to the eye. Two series with different oxidation times in an Ar-O_2 mixture are plotted. The annealing time is 5 min.

fig. 5.6). A spin polarisation of 31% was previously deduced for the polycrystalline top electrode from Co/AlO_x/Co test junctions. Applying the Jullière model to the Fe/CCFA/AlO_x/Co junctions, a spin polarisation of 54% is deduced for $Co_2Cr_{0.6}Fe_{0.4}Al$. This value of spin polarisation is comparable to the value reported by Inomata *et al.* [95]. They reported a spin polarisation of 52% at 5 K using CoFe as a counter electrode material.

Recently, Cinchetti *et al.* [117] measured the spin polarisation in our samples using spin-resolved photoemission. They report a spin polarisation of 45% at room temperature. Unfortunatelly, the use of a CoO layer as antiferromagnetic material for pinning in our tunneling junctions does not allow the measurement of the spin polarisation at room temperature. In this sense, a future switch to FeMn as material for the exchange bias is planned. Nevertheless, by comparison also with Co-Co test junctions, a spin polarisation of 48% at 77 K for $Co_2Cr_{0.6}Fe_{0.4}Al$ is calculated. Thus, we believe that the spin polarisation at room temperature would stay below the value reported by Cinchetti *et al.* There are different factors

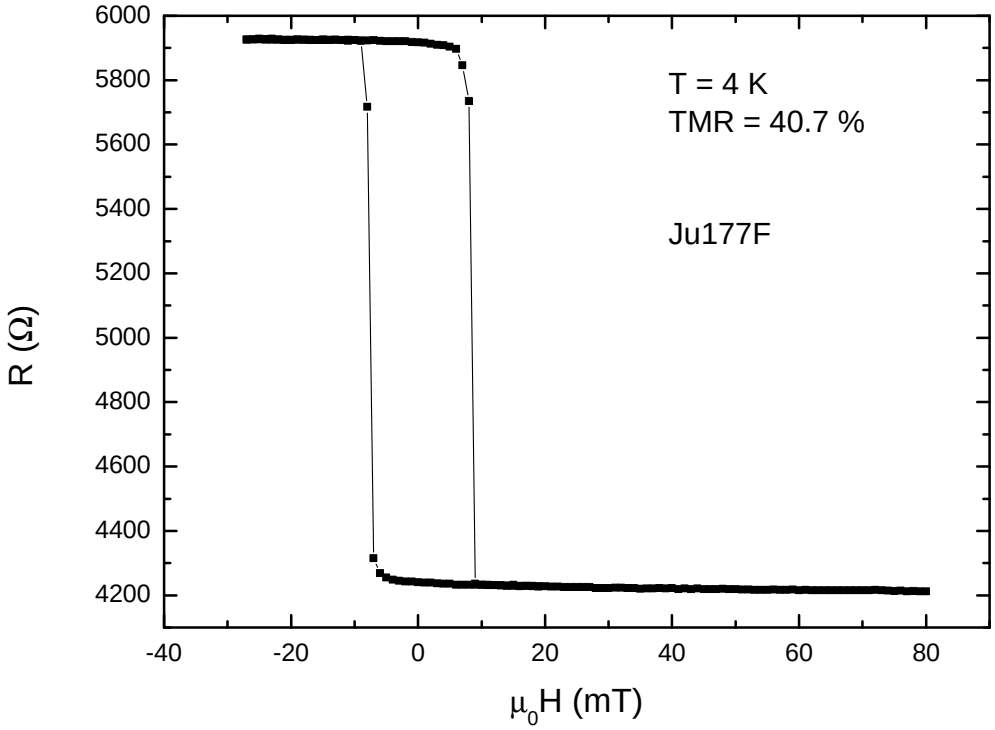

Figure 5.6: Maximal measured TMR ratio at 4 K of a MTJ with epitaxial $Co_2Cr_{0.6}Fe_{0.4}Al$ electrode deposited on Fe buffer layer on MgO (100) and annealed at 550 °C for 5 min. The bias voltage is 1 mV and the nominal barrier thickness is 3 nm.

which can explain this disceprancy. The thin films analyzed by Cinchetti suffered several *ex situ* sputter/annealing cycles to remove the Al capping layer and the top atomic layers. This process results in a reconstruction of the film surfaces. On the other hand, there may be other factors affecting the correlation between the spin polarisation of the emitted electrons and the DOS in the case of photoemission experiments and the spin polarisation of the tunneling current and the DOS in the case of MTJ's.

Additionally, point contact spectroscopy measurements have been also performed with $Co_2Cr_{0.6}Fe_{0.4}Al$ samples. Auth *et al.* [118] estimated a spin polarisation of 49% with a superconducting Sn tip whereas the group of Karthik [119] reported a value of 54% with a superconducting Nb tip. In both cases the experiments were performed on polycrystalline bulk samples. By point contact spectroscopy it is difficult to control how deep penetrates the tip into the sample and, therefore, it is probable that the measured polarisation does not correspond to the surface of the sample. Additional complications arise from the fit of the

experimental data to the theoretical models in order to extract the value of the spin polarisation. The inclusion of a parallel and a serial resistance as parameters in the model allows the fit of a determined spectrum with different combinations of the parameters and different values of the spin polarisation.

Some words must be said concerning the resistance of the junctions. For the junction series shown in fig. 5.5, the RS product varies between 23-160 $\mathrm{M\Omega \cdot \mu m^2}$ for an oxidation time of 90 s and increases to 100-240 $\mathrm{M\Omega \cdot \mu m^2}$ for an oxidation time of 120 s. The resistance of the junctions shows a linear dependence on the temperature with an increase of $\sim$30% from room temperature to 4 K. We consider this behavior as an indication of an insulating fully oxidized barrier.

As seen in Chapter 4, epitaxial growth is also achieved on $MgAl_2O_4$ and Al_2O_3 substrates. In fact, RHEED reflections and crystalline properties as observed by x-ray diffraction are even better for samples deposited on $MgAl_2O_4$. For the case of Al_2O_3 substrates, RHEED reflections are also sharper but a small shoulder is observed in the $\theta/2\theta$ scans. The TMR ratios of samples with epitaxial $Co_2Cr_{0.6}Fe_{0.4}Al$ deposited directly on these substrates are smaller. In the case of Al_2O_3 , the TMR amounts to 19% while for $MgAl_2O_4$ ratios of 31% have been measured for samples annealed at 550 °C.

5.3.2 Correlation between surface order and topology and TMR

A clear correlation between the improvement of the TMR ratio and the surface ordering as observed by RHEED is found. In fig. 5.7 the RHEED diffraction patterns for as deposited samples and for samples annealed at different temperatures are shown. The annealing time is always 5 min.

The as-deposited samples show always typical 3D RHEED. For some samples, the spots are very weak. By increasing the annealing temperature we observe a transition from the previously irregular pattern to a circular arrangement of bright spots, characteristic from a well ordered 2D system. Additionally, Kikuchi lines appear and become more defined at higher temperatures. This transition concurs with the observed increase of the TMR ratio (fig. 5.5). Thus, a correlation between the surface crystalline order and the TMR is observed. This point shows again the importance of the interface/surface quality for the spin polarisation of the tunneling current.

On the contrary, the drop of the TMR at annealing temperatures above 550 °C

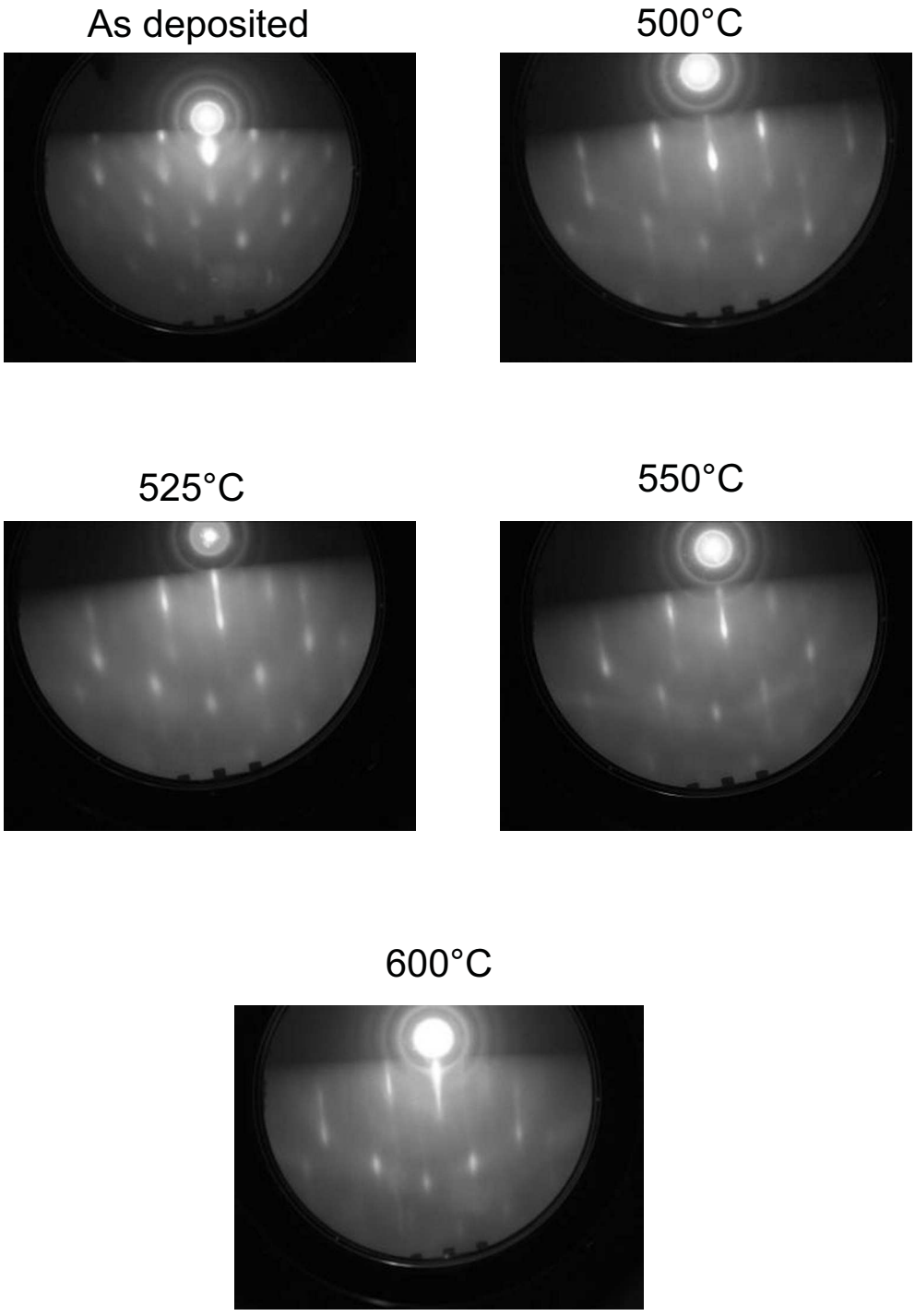

Figure 5.7: RHEED diffraction patterns of samples annealed at different temperatures. All the samples were deposited on Fe buffer layers and annealed for 5 min. The primary electron beam energy is 20 keV.

can not be correlated to the RHEED patterns. Indeed, as observed in fig. 5.5, the quality of the RHEED patterns is better for higher annealing temperatures. At this point, it may be argued that a larger surface roughness by higher annealing temperatures is the reason for the decrease in the TMR. This argument is not confirmed by STM surface imaging[3]. In fig. 4.23, no significant differences can be seen for samples annealed at 550 and 600 °C.

Recent XAS measurements seem to indicate a Fe enrichment in the annealed samples deposited on Fe buffer layers. This enrichment is explained as an interdiffusion of Fe from the buffer to the $Co_2Cr_{0.6}Fe_{0.4}Al$ film. In parallel, a Cr diffusion from $Co_2Cr_{0.6}Fe_{0.4}Al$ to the buffer layer is also plausible. Thus, an enhanced Fe interdiffusion at higher annealing temperatures may explain the decrease of the TMR annealed over 550 °C . Unfortunately, the available data does not allow to estimate if this enrichment is stronger with higher annealing temperature. Further investigations are needed to confirm this hypothesis.

5.3.3 Surface tailoring

From the correlation between the RHEED patterns and the TMR values we conclude that the interface CCFA-barrier is crucial to achieve a high spin polarisation of the tunneling current. Therefore, the selective modification of the surface of the $Co_2Cr_{0.6}Fe_{0.4}Al$ films opens new possibilities to improve the TMR ratios.

As a first experiment, we tried to confirm the hypothesis relating the drop of the TMR with higher annealing temperatures to an Fe enrichment (or equivalently Cr depletion). Very thin Cr layers were deposited on the $Co_2Cr_{0.6}Fe_{0.4}Al$ films. The deposition of these layers was done before the annealing in the hope that the temperature treatment would induce Cr to diffuse in the $Co_2Cr_{0.6}Fe_{0.4}Al$ surface. In this way we may correct the film surface composition back to the desired stoichiometry.

Two series with different Cr layer thicknesses were deposited, each with different annealing temperature: 550 °C and 600 °C. The results are plotted in fig. 5.8.

For the samples annealed at 550 °C, no relevant changes are observed between non-tailored samples and samples with Cr thicknesses up to 2.5 Å. For thicker Cr

[3] As already discussed, RHEED is sensitive to the surface roughness. However this sensitivity is limited by the width of the electron beam and the surface properties are promediated over a certain region. On the contrary, STM has a increased sensitivity and small material exclusions can be detected.

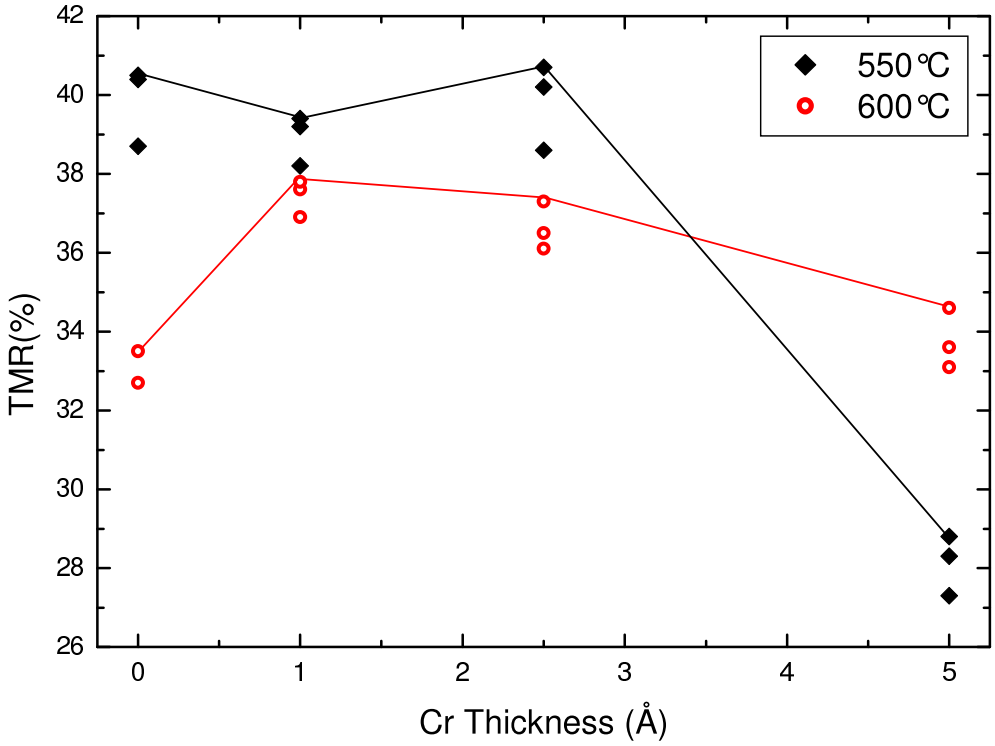

Figure 5.8: Dependence of the TMR ratio on the thickness of the Cr tailoring layer deposited on the $Co_2Cr_{0.6}Fe_{0.4}Al$ film. The Cr layer was deposited before annealing. The black (red) points represent samples from a series annealed at 550 °C (600 °C). The lines connect the highest TMR values are intended only as a visual guide. The annealing time is 5 min. In all cases the oxidation time is 90 s and the Al thickness is 3 nm.

layers, a fast drop in the TMR is observed. However, an improvement can be recognized for tailored samples annealed at 600 °C in comparison with samples without additional Cr. Again, a reduction of the TMR for Cr thicknesses larger than 2.5 Å is observed though the decrease is less pronounced for the MTJ's annealed at higher temperature.

The behavior of MTJ's annealed at 550 °C can be explained if we assume a reduced diffusion of the Cr tailoring layer into the $Co_2Cr_{0.6}Fe_{0.4}Al$. In this case, a large percentage of the deposited Cr lays on top of the CCFA and does not affect its stoichiometry and spin polarisation. Only for larger Cr thicknesses, a thick Cr layer is situated between the ferromagnet and the barrier and the TMR drops fast. In fact, this situation is exactly equivalent to the experiments with dusting layers described in Section 1.1.3 [19, 20, 21, 23].

On the other hand, for samples annealed at 600 °C an enhanced diffusion is

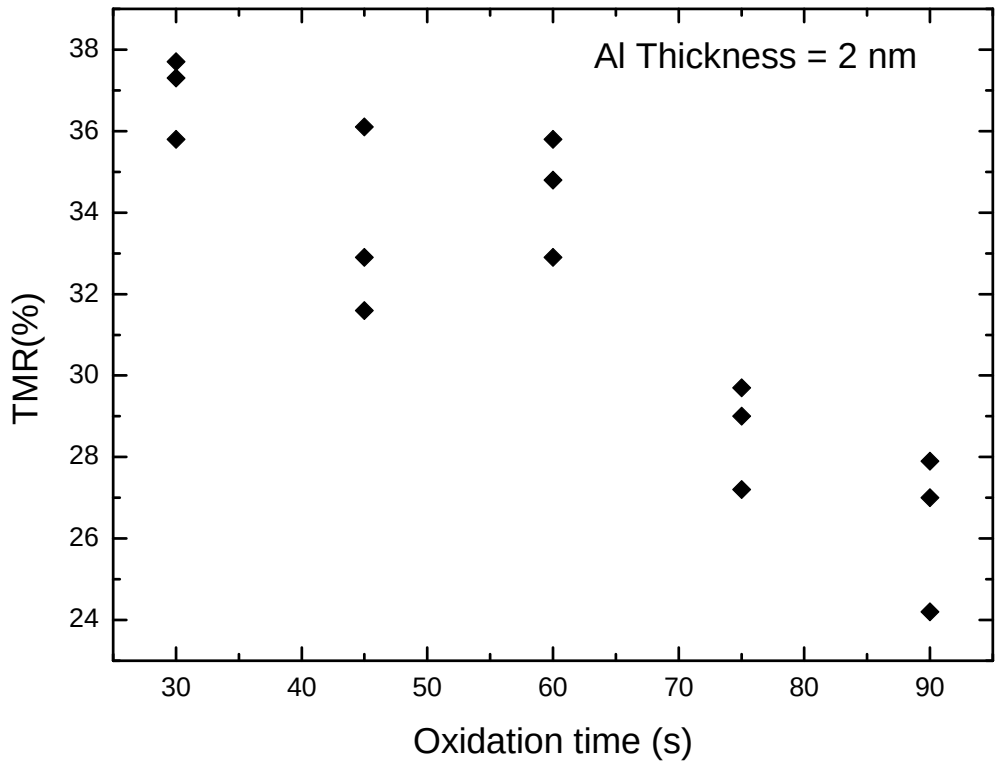

Figure 5.9: Dependence of the TMR ratio on the oxidation time for samples deposited on Fe buffer layer and annealed at 550 °C for 5 min. The nominal Al thickness for this series is 2 nm. A mixture Ar-O_2 is used.

expected. In this case, the increase in the TMR can be explained in terms of a correction of the Fe enrichment. The smaller drop in the TMR with thicker Cr layers is also in concordance with this argumentation. Since the Cr now diffuses stronger in the CCFA, the thickness of the rest Cr layer is smaller.

As a conclusion, this tailoring experiment gives an additional indication that the Fe interdiffusion from the buffer layer is the reason for the fast drop of the TMR of samples with higher annealing temperatures. Furthermore, different tailoring strategies could be successful in order to improve the TMR ratios.

5.3.4 Oxidation time dependence

The dependence of the TMR ratio on the oxidation time was investigated for a series of samples with a nominal Al thickness of 2 nm. In this case the maximal achieved TMR values are slightly smaller than for a thickness of 3 nm. The gas used for this series is a mixture argon-oxygen.

The results are plotted in fig. 5.9. We observe a strong tendency to a reduced TMR with increasing oxidation time. We believe this behavior is a consequence of an oxidation of the $Co_2Cr_{0.6}Fe_{0.4}Al$ electrode with the consequent loss in spin polarisation. This explains also the increased TMR values for 3 nm thick barriers for equal oxidation times. With decreasing oxidation time we see an increase in the TMR with a trend to stabilize near 40%.

5.3.5 TEM

Some selected junctions were studied with a transmission electron microscope (TEM) in order to investigate the quality of the barrier. In fig. 5.10 two of these images are shown. The top image shows the complete MTJ stack and covers a large area. Due to the low contrast it is not possible to distinguish the CoO layer on top of the MTJ in the top panel of fig. 5.10. For the same reason, the Fe buffer layer is hardly visible in this image. No Pt capping layer was used for this sample. The barrier is visible as a bright line separating the CCFA and Co electrode. We observed that the barrier is smooth and homogeneous on large scales. Also no pinholes or other defects can be seen.

The presence of weak points or irregularities in the barrier were studied with increased microscope magnification. An example image is given in the bottom panel of fig. 5.10. At this scale the barrier looks also smooth, homogeneous and defect-free.

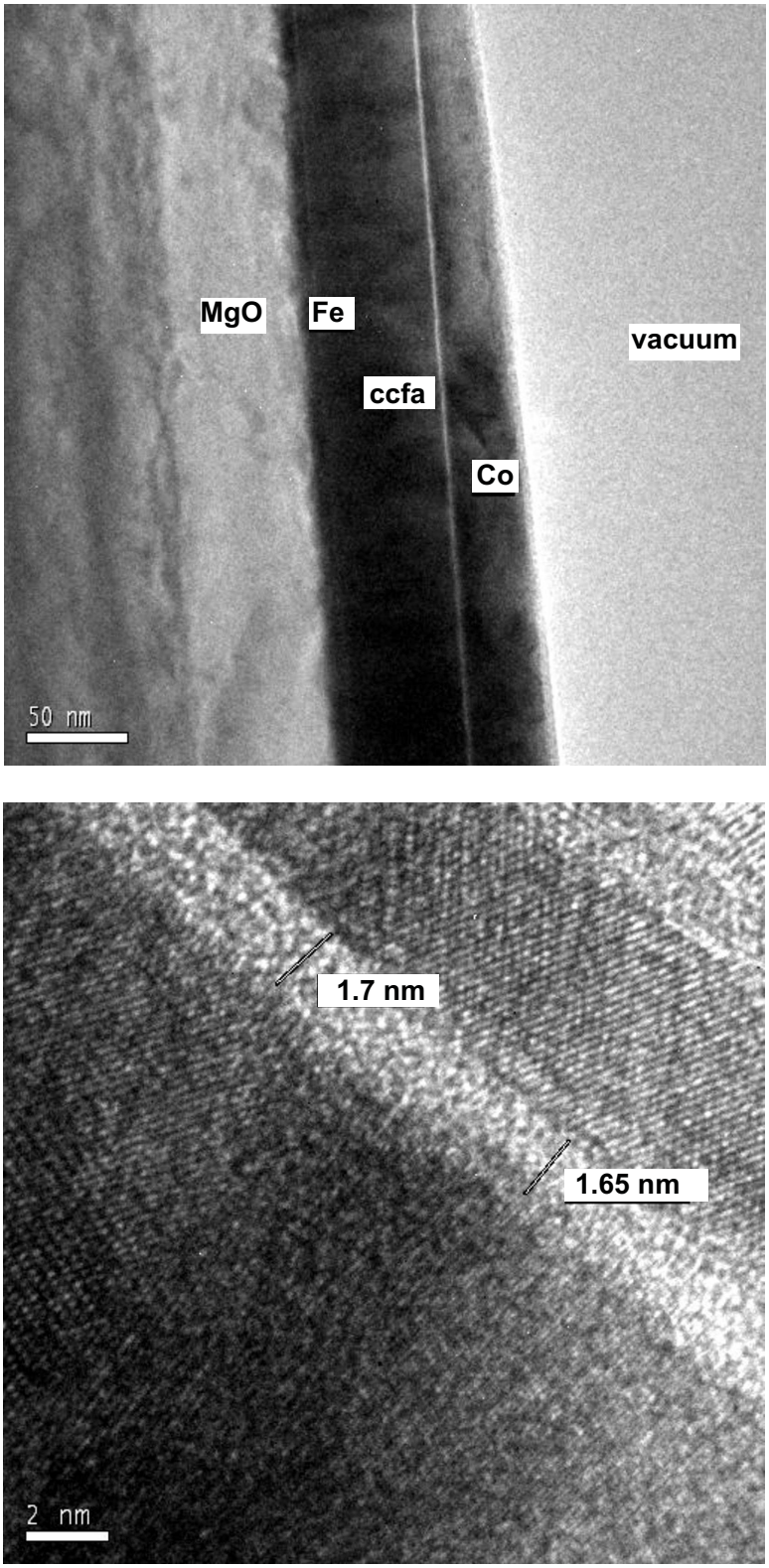

Figure 5.10: Top: TEM image of a Fe/CCFA/AlO_x/Co/CoO MTJ deposited on MgO. Clearly it is observed that the barrier is smooth and defect-free on large scales. Bottom: Detail of a tunneling barrier. Both figures are courtesy of Christian Herbort.

Chapter 6

Tunneling spectroscopy

Spectroscopic experiments in superconductor to normal metal tunnel junctions are a widespread method for the study of the coupling mechanism in superconductors. Alternatively, by substituting the normal metal by a ferromagnet (Meservey-Tedrow junctions), tunneling junctions are used to estimate the spin polarisation of ferromagnetic materials.

Spectroscopy has not attracted large attraction in magnetic tunneling junctions and only in the last years the interest has started to grow. Mainly, this situation can be attributed to two reasons. First of all, the voltage applicable to a junction is limited by breakdown processes in the barrier. In a tunneling junction the voltage drop in concentrated in the barrier and therefore, high electrical fields are generated even for low voltages. These high fields induce a degradation of the insulating barrier. This degradation can happen in a continuous or in abrupt way depending on the properties of the barrier [121, 122]. A continuous degradation is a result of a thermal-assisted growth of pre-existing pinholes due to a high local current densities[1]. On the contrary, for an originally hole-free barrier, a step-like degradation occurs as a consequence of breakdown processes which destroy locally the barrier. In this sense, the presence of weak spots, i.e. local regions with thinner barrier, increases the possibility of deterioration by reducing the breakdown electric field.

The second reason lays in the parabolic dependence of the differential conductivity dI/dV on the bias voltage V_{BIAS}, as explained in Section 1.2. The quadratic

[1]Since the current always chooses the way of smaller resistance and the pinholes open a direct connection between the two electrodes, it is not a surprise that the current density in them can be very high. The generated heat induces atom migration from the electrode to the barrier with its subsequent progressive degradation.

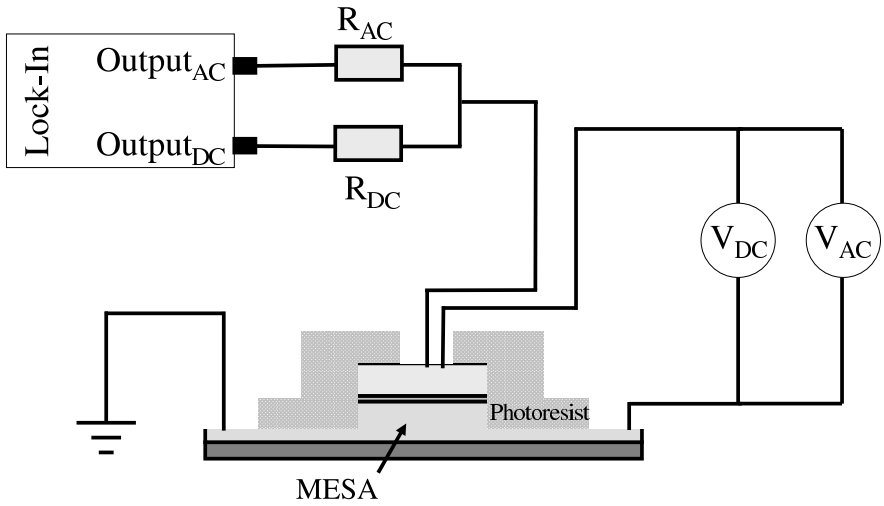

Figure 6.1: Schematic representation of the experimental setup used to measure the differential conductivity dI/dV.

change of dI/dV blurs out other effects like band structure effects and allows only very strong features to be visible.

Additionally and partially as a direct consequence of the previous point, the question of electrical noise can make spectroscopy measurements in MTJ's a challenge. Furthermore, for certain kind of measurements noise considerations plays a more important role. On example is the measurement of the dependence of the TMR on V_{BIAS} where two different measurements must be subtracted.

6.1 Measurements of the differential conductivity dI/dV

The differential conductivity dI/dV was measured directly using standard lock-in techniques. Alternatively, the dI/dV curves can be determined by differentiation of the I(V) curves. However, this method results in increased noise and it is discarded. In order to perform the measurements, two currents, *dc* and *ac*, are sent through the junction (see fig. 6.1). These currents are generated with the voltage outputs of the lock-in amplifier which are connected in serial to two independently tunable resistances. In order to obtain an ideal current source, it must be accomplished that $R_{AC}, R_{DC} \gg R_{Junction}$. The correspondent *ac* voltage signal in the junction (V_{AC}) is measured by the lock-in amplifier and a

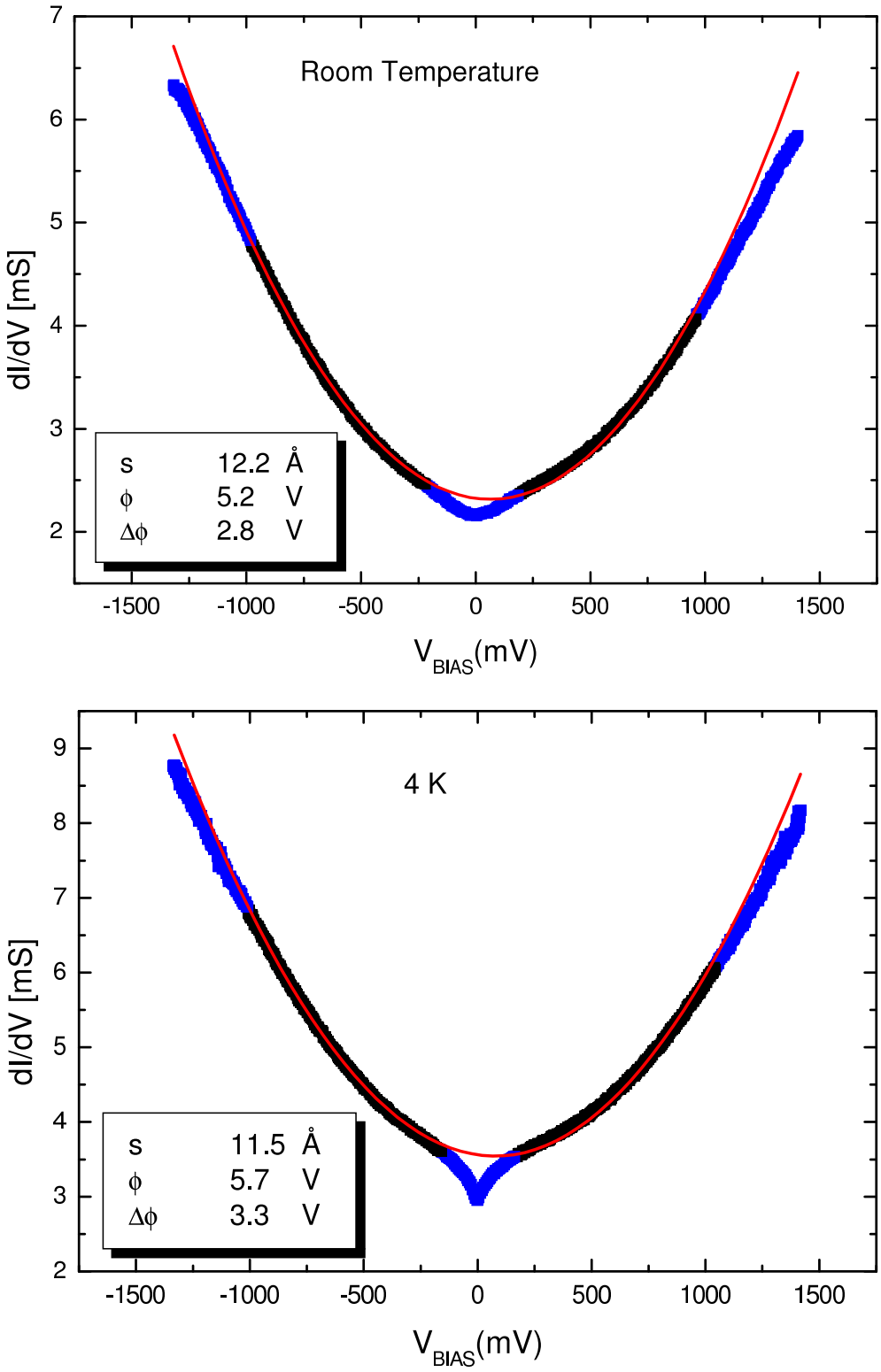

Figure 6.2: Differential conductivity dI/dV versus bias voltage for non-annealed Fe/CCFA/AlO_x/Co/CoO/Pt samples measured at room temperature (top) and 4 K (bottom). For negative voltages the electrons tunnel into $Co_2Cr_{0.6}Fe_{0.4}Al$. The red line represents a fit using Brinkman's model. Blue points are not considered for the fit. ϕ, $\Delta\phi$ are the height and asymmetry of the potential barrier, respectively. s is the width.

nanovoltmeter is used to measure the *dc* voltage (V_{DC}=V_{BIAS}). The *ac* voltage is kept small (100-500 μV) to prevent distortions in the measurement of V_{BIAS}.

In order to understand how it is possible to measure dI/dV directly it should be remembered that the total current going through the junction can be separated in two terms: a *dc* current generated by the bias voltage and a *ac* current generated by the sinus voltage output of the lock-in amplifier. Since the *ac* current is much smaller than its *dc* counterpart, it can be considered as a small perturbation allowing a Taylor expansion of $V(I)$ around I_{dc}:

$$V\left(I_{dc}+I_{ac}\,sin\left(\omega t\right)\right)=V(I_{dc})+\frac{\partial V}{\partial I}\Big|_{I_{dc}}I_{ac}\,sin\left(\omega t\right)+\frac{\partial^2 V}{\partial I^2}\Big|_{I_{dc}}I_{ac}^2\,sin^2\left(\omega t\right)+\ldots=$$
$$V(I_{dc})+\frac{\partial V}{\partial I}\Big|_{I_{dc}}I_{ac}\,sin\left(\omega t\right)+\frac{1}{4}\frac{\partial^2 V}{\partial I^2}\Big|_{I_{dc}}I_{ac}^2\,\left(1-cos\left(2\omega t\right)\right)+\ldots \quad (6.1)$$

When the lock-in amplifier is set to measure signals with a frequency ω, the measured signal is proportional to the differential conductivity dI/dV.

The dI/dV (V_{BIAS}) curves for non-annealed samples are plotted in fig. 6.2. The top panel shows typical measurements at room temperature while the bottom panel shows the situation for 4 K. The red line represents a fit using the Brinkman model presented in Section 1.2. The blue color corresponds to data points that are not considered for the fit. For negative voltages the electrons tunnel into $Co_2Cr_{0.6}Fe_{0.4}Al$.

The data points for voltages larger than 1100 mV deviate from the parabolic behavior expected from eq. 1.2. This is due to V^3 and higher order terms not included in the model. These terms are important only at high voltages. For very small voltages, additional deviations from the model are observed. These deviations are a consequence of a feature growing with decreasing temperature. This structure is the so-called *zero bias anomaly* and it characteristic for magnetic tunneling junctions, also with conventional ferromagnets. Although it is a well known effect, the origin of the anomaly is controversial and different interpretations are found in the literature. This subject will be discussed later in Section 6.2.1.

The characteristic parameters for the barrier obtained from the fit are given in the graphs. It is very important to remember at this point that these values make reference to the model barrier potential and not to the actual oxide barrier. The parameter ϕ is the height of the barrier, s is the width and $\Delta\phi$ is the asymmetry as defined in Section 1.2.

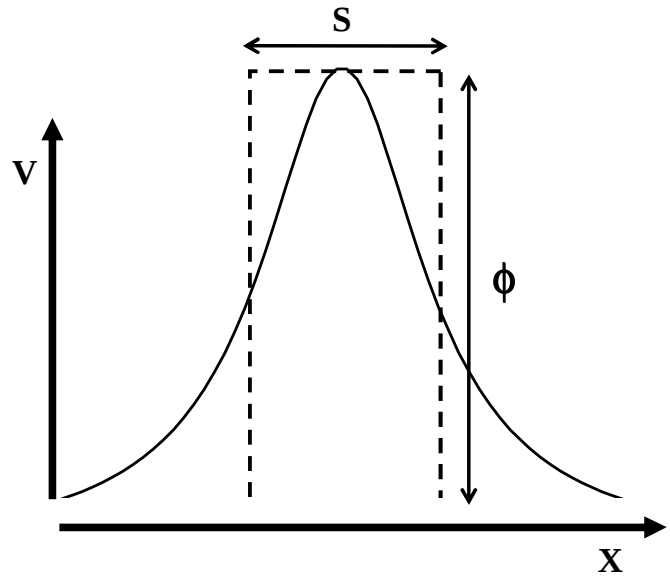

Figure 6.3: Schematic representation of the potential barrier of a tunneling junction. The solid line represents the actual barrier while the dashed line corresponds to the Brinkman's model.

In order to estimate the error of the parameters, several simulations of the dI/dV curves with small variations of the parameters from the best fitted values were performed. In each case only one parameter was varied. For ϕ and s, already small variations of $\pm 0.5\%$ result in curves which differ clearly from the experimental data. On the contrary, $\Delta\phi$ can be varied by $\pm 30\%$ and the resulting curve still follows quite well the experimental one. The explanation for this behavior is clear, the width and height of the potential barrier have a large effect in the overall conductivity and small changes shifts the parabola towards higher or lower conductivities. $\Delta\phi$ only influences slightly the shape of the parabola.

In the parameters shown in fig. 6.2 an improvement of the barrier characteristics with decreasing temperature is recognized. The barrier becomes higher and thinner at low temperatures. This a general tendency observed in all of our junctions. It is not a surprising behavior since the resistivity of an insulator increases with decreasing temperature.

Typical values for s in our junctions vary between 10 and 15 Å while ϕ is usually well above 3.5 V, reaching values near 6 eV. These high values are compatible with band gap estimations found in the literature. Measurements of single crystalline bulk Al_2O_3 samples show a band gap of 8.8 eV [123] whereas experiments in amorphous Al_2O_3 thin films yield a bottom threshold value of 6.2 eV for the

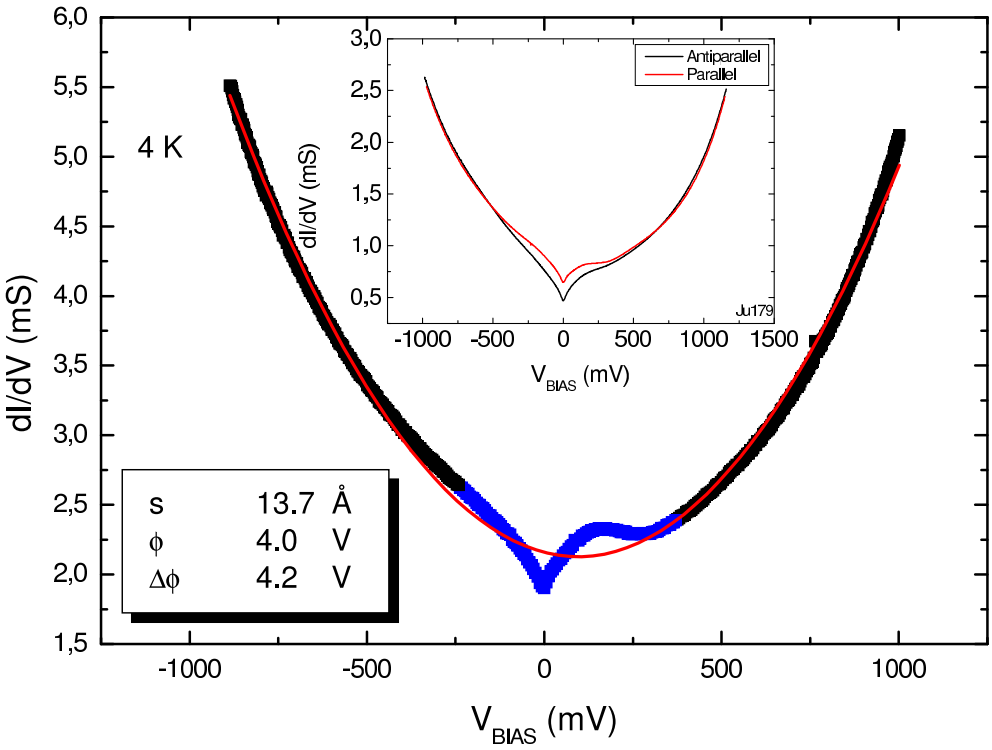

Figure 6.4: Differential conductivity dI/dV versus bias voltage for annealed Fe/CCFA/AlO_x/Co/CoO/Pt samples measured at 4 K. For negative voltages the electrons tunnel into $Co_2Cr_{0.6}Fe_{0.4}Al$. The red line represents a fit using Brinkman's model. Blue points are not used for the fit. The inset shows a comparison between the measurements for the antiparallel and parallel configuration.

gap [124]. On the other hand, the values of s may look to small when compared with the nominal thickness of 3 nm of the Al layer. It must be remembered again that the parameters are of the potential barrier and not of the physical oxide barrier. Additionally, the potential barrier is modeled with a trapezoidal shape. This situation, with infinitely sharp interfaces is not realistic. Let us consider a most general shape[2] for the barrier represented by the solid line in fig. 6.3, the fit for the potential using a trapezoidal shape is represented by the dashed line. The "tails" of the barrier are not included in the model, and therefore the parameter s should best be interpreted as the FWHM of the barrier. Indeed, the smaller value of s compared to the nominal thickness may be an indication of the good quality of the barrier since a concordance of both values would only be possible

[2]Here a symmetrical barrier is drawn. In a more general description a non-symmetrical barrier should be included.

with an oxidation of the metallic electrodes.

An example of dI/dV measurements for MTJ'S with annealed $Co_2Cr_{0.6}Fe_{0.4}Al$ electrodes is plotted in fig. 6.4. Some differences compared to as deposited samples are present. An additional wide structure is observed at a voltage of ∼150 mV. This structure is extremely weak or inexistent in as deposited samples but it is always present in annealed samples, with different strength depending on the sample. Since the major differences between both families of MTJ's are in the $Co_2Cr_{0.6}Fe_{0.4}Al$ surface (observation of well defined RHEED pattern, see for instance fig. 5.7), it may be concluded that this structure is related to the interface CCFA/barrier. However, alternative explanations are possible. The interpretation of this structure and of the zero bias anomaly will be discussed in Sections 6.2.1 and 6.2.3.

Another important detail in the dI/dV curves of annealed samples lays in the very high values of $\Delta\phi$. The value of $\Delta\phi$ obtained from the fit are as large or even larger than the averaged height ϕ, as for instance in fig. 6.4. This values may be a failure resulting from the increased overall asymmetry of the parabola due to the structure at 150 mV. This kind of features are not included in the model and therefore the values of $\Delta\phi$ may be overestimated.

The inset in fig. 6.4 shows the comparison between the parallel and the antiparallel configuration for a different annealed sample . In general, the structure at 150 mV is less pronounced for the antiparallel configuration.

From the measurements of dI/dV for both the parallel and antiparallel configuration, the TMR dependence on the bias voltage is extracted. This dependence is plotted in fig. 6.5. The top graph shows the case of a non-annealed sample with epitaxial $Co_2Cr_{0.6}Fe_{0.4}Al$ electrode deposited on Fe Buffer layer. The bottom one shows the case of a sample with bottom electrode annealed at 550 °C.

In both cases, a fast reduction of the TMR ratio with increasing bias voltage is observed. This fast decrease is related with the zero bias anomaly observed in the dI/dV curves. Again, this is a general behavior of MTJ's. It was already observed in the pioneering work of Jullière [4]. He observed that the TMR ratio felt to the half of its zero bias value already at V_{BIAS}= 3 mV. With improvements in the deposition and oxidation techniques, the voltages at which the TMR reduces to the half have been increased for conventional ferromagnets to values reaching 200 mV [125] and even 500 mV values have been reported by some groups [126, 127].

In our junctions, the TMR drop with the bias voltage is not symmetric. For

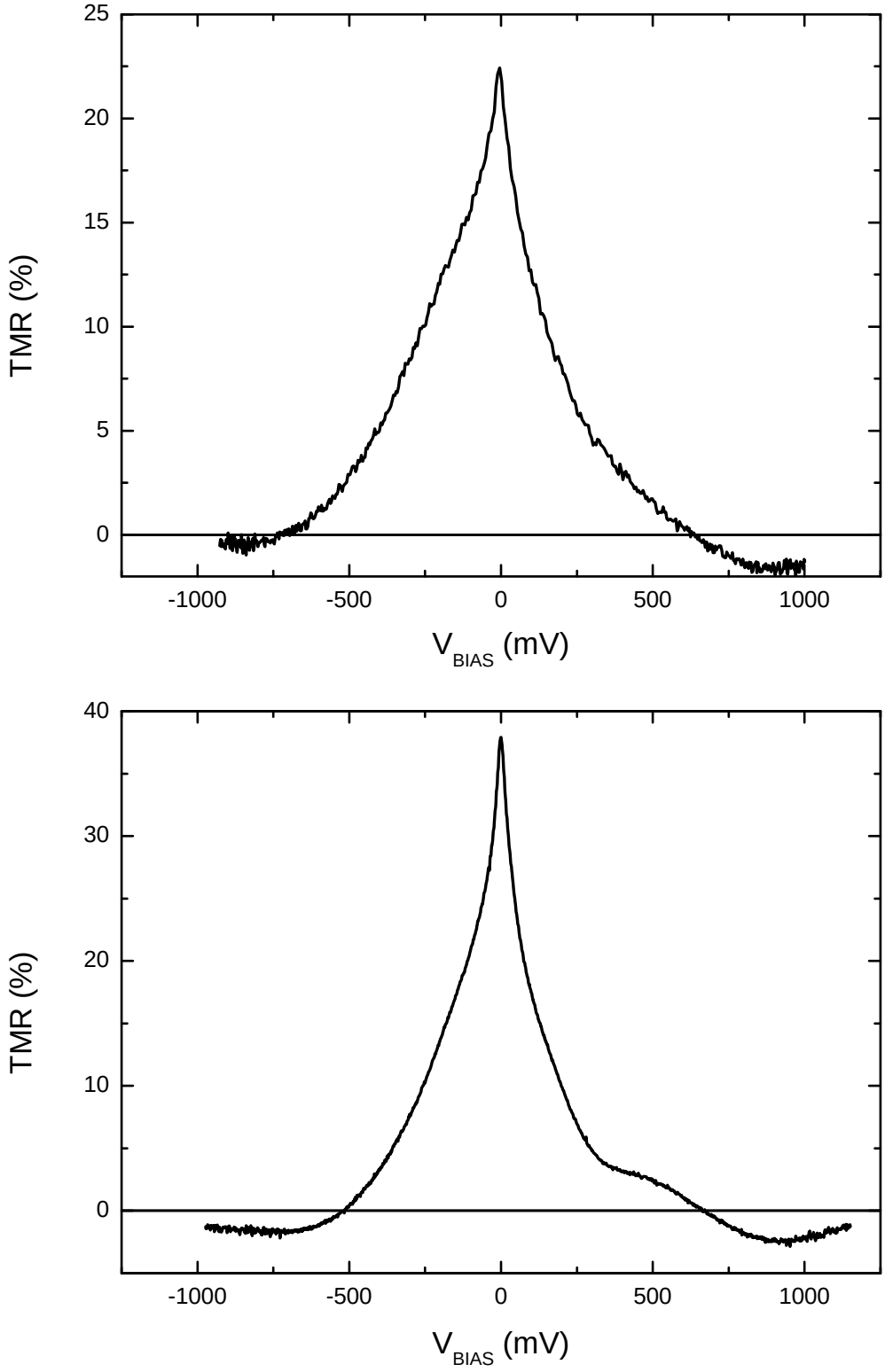

Figure 6.5: TMR dependence on the bias voltage for as deposited (top) and annealed (bottom) Fe/CCFA/AlO_x/Co/CoO/Pt samples measured at 4 K. For negative voltages the electrons tunnel into $Co_2Cr_{0.6}Fe_{0.4}Al$.

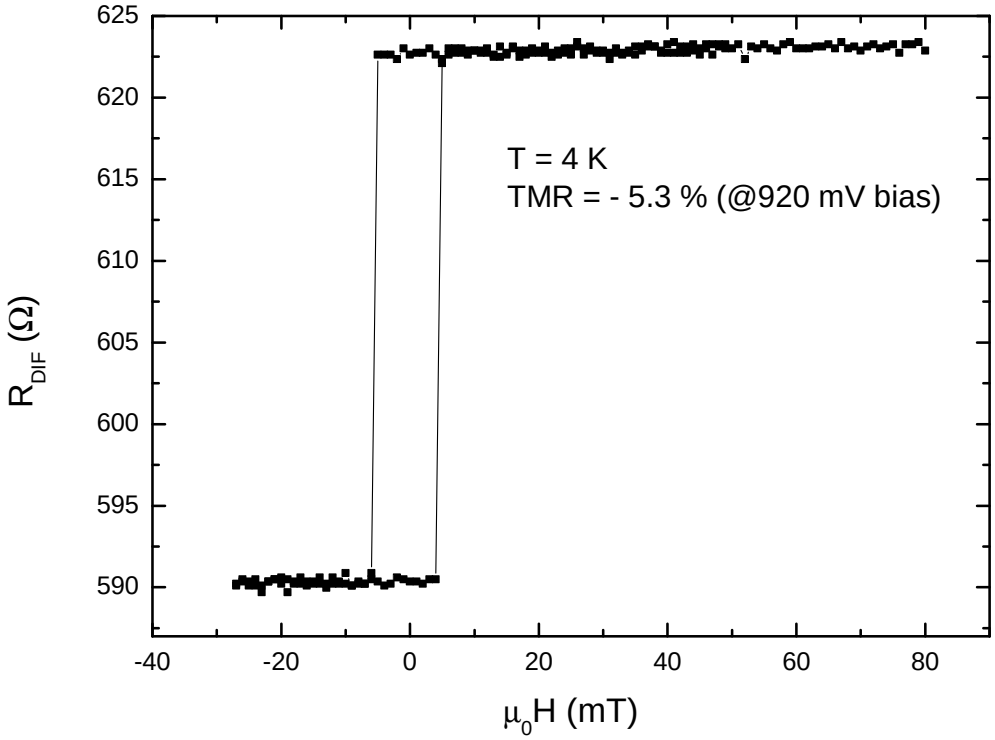

Figure 6.6: Negative TMR measured at 4 K and with 920 mV bias voltage for the same sample as the bottom panel of fig. 6.5.

samples with annealed CCFA films, the *half-TMR* voltage is 120 mV for negative bias voltages (electrons tunneling into CCFA) and 90 mV for positive bias (electrons tunneling in Co). For samples with non annealed electrodes, the values are smaller, 90 mV and 50 mV for negative and positive voltages, respectively. Concerning junctions containing at least one Heusler electrode, not many TMR(V_{BIAS}) measurements have been published. From the few papers we found, a general tendency to asymmetric curves is seen. For MTJ's with Co_2MnSi, half-TMR voltages of 175 and 100 mV are measured, depending of the sign of the bias [128]. For the same compound, another group reports values smaller than 100 mV [52]. For $Co_2Cr_{0.6}Fe_{0.4}Al$, no publications were found for junctions with Al_2O_3 barrier. For MTJ's with MgO barrier, half-TMR values of 420-530 mV are measured [92]. However, the use of a different barrier material does not allow a comparison in this last case.

A change in the sign of the differential TMR is also observed for high voltages (>500 mV). This negative TMR is also demonstrated with the measurement of the magnetoresistance curve at high bias voltages, as shown in fig. 6.6. This

graph corresponds to the same junction from which the curve in the bottom panel of fig. 6.5 was obtained. Though the change in sign is verified, a small discrepancy in the absolute value of the TMR is present. The TMR ratio obtained from the magnetoresistance curve is larger than the one from the TMR(V_{BIAS}) curve. The reason for the discrepancy is clear. Since the resistance of a junction changes by changing the magnetic configuration, the bias voltage is not the same in both configurations. Therefore, a bias voltage-generated additional change in the conductivity is measured in the TMR curve at large voltages

Let us define $\frac{\Delta G}{G_{AP}}(V_{BIAS})$ as the TMR value obtained from subtracting the dI/dV (V_{BIAS}) curves for the parallel and antiparallel configuration. In the same way, $\frac{\Delta R}{R_P}$ is defined as the TMR value obtained from the magnetoresistance curve plotted for instance in fig. 5.6. The previous considerations show that the curve $\frac{\Delta G}{G_{AP}}(V_{BIAS})$,$(G = \frac{dI}{dV})$, is not equivalent to the $\frac{\Delta R}{R_P}(V_{BIAS})$ as one could have expected. In order to compare results between different groups referring TMR(V_{BIAS}) dependences, one should take this point into account. In the literature, $\frac{\Delta G}{G_{AP}}(V_{BIAS})$ are almost always preferred since V_{BIAS} is good defined. When measuring $\frac{\Delta R}{R_P}$ the bias voltage is different in the parallel and antiparallel configuration with the consequent complications at the time to interpret the measurements and to compare them to band structure calculations. Additionally, $\frac{\Delta G}{G_{AP}}$ measurements are also favored due to their greater sensitivity.

Such changes in the sign of the TMR have been also found in other Heusler compounds as for instance Co_2MnSi [129]. In this case, the voltage needed to obtain a negative TMR is larger than 1000 mV. Also in tunneling junctions with conventional ferromagnets, negative TMR induced by bias voltage is observed [130]. The presence of such an effect in MTJ's is extremely interesting concerning applications. In Section 1.3, the possibility to use arrays of TMR elements for building morphware (programmable logic gate arrays) was appointed. With the option to switch from a normal to an inverse TMR with a voltage, we can convert AND and OR is NAND and NOR gates, with the consequent gain in flexibility of the circuit.

The most striking and interesting difference in the TMR(V_{BIAS}) curves between MTJ's with as deposited and annealed $Co_2Cr_{0.6}Fe_{0.4}Al$ electrodes is the shoulder observed in the positive bias region. This shoulder in present in all the annealed samples and appears simultaneously to the feature observed in the dI/dV curves.

6.2 Interpretation of the dI/dV (V_{BIAS}) and TMR(V_{BIAS}) measurements

The interpretation of the different observed structures in the dI/dV (V_{BIAS}) curves in not straightforward. In some points, strong discrepancies concerning the meaning of some features can be found in the literature. Here, I will try to comment on the validity of the different explanations.

In the simple model of Jullière, dI/dV for the a parallel alignment is proportional to $N_{1\uparrow}\,N_{1\uparrow} + N_{2\downarrow}\,N_{2\downarrow}$ while for the antiparallel case it is proportional to $N_{1\uparrow}\,N_{2\uparrow} + N_{1\downarrow}\,N_{2\downarrow}$. $N_{\uparrow(\downarrow)}$ represents the density of states for up (down) electrons in the two electrodes (1,2). It was already mentioned that Jullière's model produces coherent values for the spin polarisation which are also consistent with measurements using superconductor-normal metal junctions. Nevertheless, since tunneling is a local process at the interface regions, *a priori* it is not possible to assume that N represents the bulk DOS.

Moreover, inelastic scattering processes at the interfaces contribute also to the differential conductivity. The role of the barrier in modifying the overall conductivity must be taken into account.

6.2.1 Zero bias anomaly

The zero bias anomaly is stronger for lower temperatures, as observed in the example for polycrystalline samples in fig. 6.2. However, the main characteristic of the zero bias anomaly that stands out is its ubiquity. It has been observed in a very wide range of magnetic tunneling junctions containing a large number of combinations of materials as electrodes. In the same way, a related pronounced drop of the TMR with increasing bias voltage is reported. This fact points out that a very general mechanism must responsible of the effect. In this sense, inelastic scattering at the interfaces or barrier effects have been postulated frequently as a possible reason.

First theoretical works by Appelbaum [131] in 1961 assumed that electron scattering during tunneling generated by impurities in the barrier is the reason for the zero bias anomaly. However, this description results in a too strong dependence on the temperature in comparison with experiments. In recent theoretical developments by Sheng *et al.* impurities in the barrier are considered as the origin of the anomaly [132]. A model is developed in which the electrons tunnel inelas-

tically via magnetic impurities in the barrier accompanied by phonon emission. This model is able to simulate the zero bias anomalies. Scheng points out that, since there is a phonon emission in the Al_2O_3 barrier, an isotope effect should be visible.

Nevertheless, in the literature a certain consensus toward a different mechanism generating the anomaly was reached. The tunneling electrons suffer an inelastic scattering with magnons or phonons *at the interfaces* electrodes-barrier. This hypothesis has received theoretical [133, 134] and experimental support [134, 135, 136, 23, 137]. The experimental support was gained with the measurements of the so called inelastic electron tunneling (IET) spectra. These spectra show the dependence of the derivative of the differential conductivity (d^2I/dV^2) on the bias voltage. Such dependence shows sharp structures which can be identified as inelastic processes (excitation of magnonic or phononic modes). This kind of structures were observed in tunneling processes with ferromagnetic materials already in 1971 in Ni-NiO-Pb junctions. In their report, Tsui *et al.* [138] were able to correlate the observed structures in the IET spectrum with a calculated magnon density of states and with data from Raman spectroscopy. These points will be further discussed in Section 6.3, where d^2I/dV^2 measurements on our junctions will be presented.

Despite the previous considerations, alternative explanations of the zero bias anomaly must be considered. Davis *et al.* [139] extended the Slonczewski model[3] [140] and calculated the TMR(V_{BIAS}) curves for $Fe/Al_2O_3/Fe$ junctions. The results fits quite well the experimental data for this system. The height and the width of the barrier were used as variable parameters. However, they assumed

[3]In Slonczewski's model the TMR ratio is related to an effective spin polarisation P_{eff} by an expression similar to the one from Jullière:

$$TMR = \frac{2\,P_{eff}P'_{eff}}{1 - P_{eff}P'_{eff}}$$

The effective polarisation P_{eff} is related with the polarisation P of the DOS of the electrodes,

$$P_{eff} = P\,\frac{\kappa^2 - k_\uparrow k_\downarrow}{\kappa^2 + k_\uparrow k_\downarrow}$$

where $k_{\uparrow(\downarrow)}$ is the Fermi wave number for the spin up (down) bands and κ is the decay length of the evanescent wave function in the barrier. In Slonczewski's model the decay length is the unique since it is assumed that only a narrow distribution of electrons with energies near E_F and with near normal incidence to the barrier carry most of the current. As a difference with Jullière's model, the role of the barrier is taken into account by including the parameter κ.

tunneling from a single parabolic band and neglected any kind of band mixing due to diffusive scattering. Additionally, the cusp-like TMR(V_{BIAS}) curves observed in most systems (included our junctions) is not reproduced.

Very recently, Sakuraba *et al.* reported the observation of a zero bias anomaly in MTJ's with both upper and bottom electrodes consisting of crystalline Co_2MnSi [52]. They interpreted the anomaly as the observation of a half-metallic gap in the Heusler electrodes. However, alternative explanations are possible. The relatively large anomaly could be explained by an enhanced magnon generation at the interfaces. This fact is supported by additional experimental data provided by the authors in the same publication. The $Co_2MnSi/Al_2O_3/Co_2MnSi$ junctions of Sakuraba *et al.* exhibit and unusually large temperature dependence, the TMR ratio falls much faster than in Co_2MnSi/Al_2O_3 /CoFe or $CoFe/Al_2O_3/CoFe$ junctions. Since the decrease of the TMR with temperature has been explained also by magnon excitation at the interfaces [141], it is reasonable to think that the increased TMR temperature dependence and zero bias anomaly in this system has the same origin.

6.2.2 Change in the TMR sign

In order to check if the negative TMR at higher voltages is related with the density of states of CCFA, we compare with band structure calculations by G. Fecher [142]. There is indeed a change in the sign of the spin polarisation for both empty and occupied states for the whole family of compounds $Co_2Cr_{1-x}Fe_xAl$. The energies (or equivalently the voltage in the spectroscopic measurements) at which there is a change of sign in the polarisation are shown in fig. 6.7. The values are plotted for different Fe doping X. The thick black line represents the case of $Co_2Cr_{0.6}Fe_{0.4}Al$. The error bars in the graph represent only the uncertainty in finding the exact voltage in the available data at which the sign change takes place.

For the compound $Co_2Cr_{0.6}Fe_{0.4}Al$, the energies at which the spin polarisation becomes negative is 490±30 meV for the occupied states and 640±20 meV for the empty states. In our sign convention for the spectroscopic measurements, the bias voltage is negative when the electrons tunnel in $Co_2Cr_{0.6}Fe_{0.4}Al$, i.e. for positive bias we investigate the unoccupied states.

In the measurements, for negative bias (unoccupied states) the TMR changes sign at 520±30 mV. The given error is the typical data scattering from sample

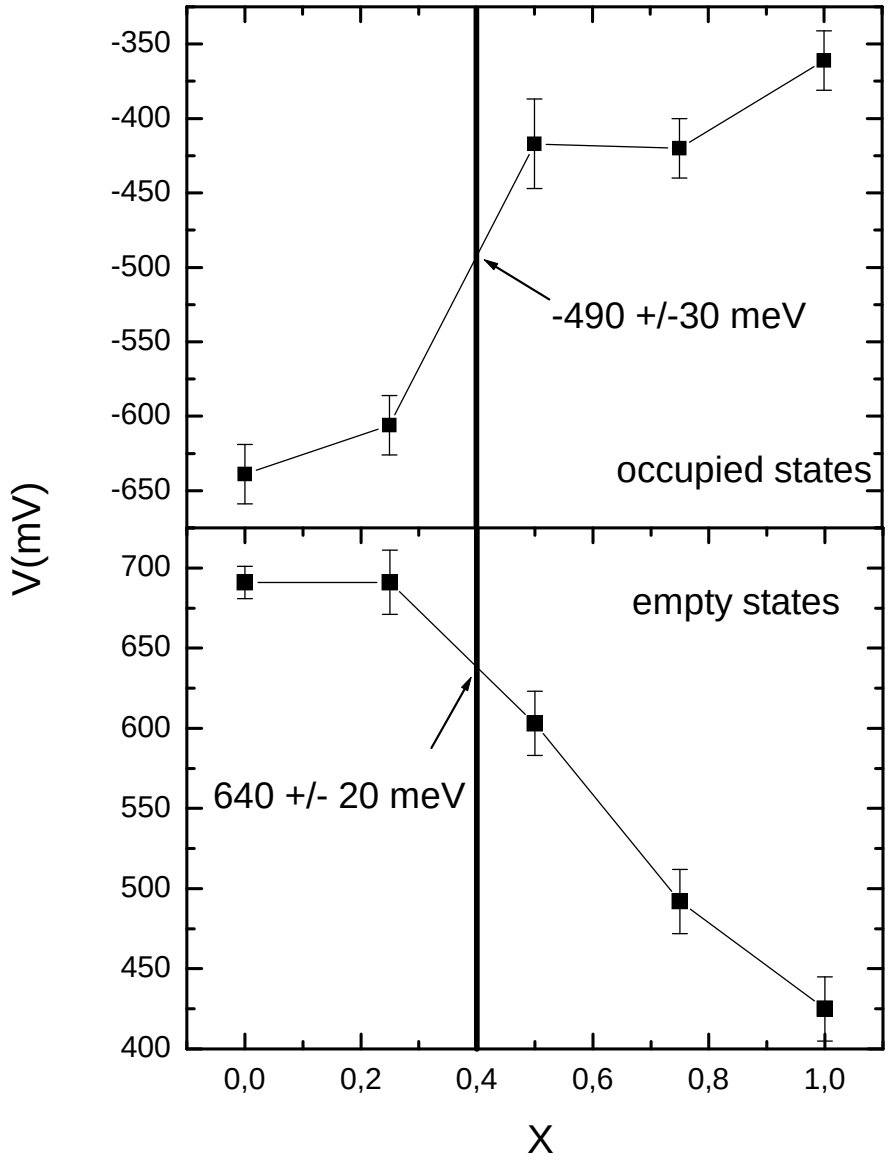

Figure 6.7: Predicted bias voltage values for a sign change in the spin polarisation of the alloy $Co_2Cr_{1-x}Fe_xAl$, for different Fe doping concentrations X. Top (bottom) panel shows the case for the occupied (empty) DOS. The plotted values are from band structure calculation by G. Fecher [142].

to sample. This value is smaller than the value provided by the band structure calculations.

For the positive bias side, the comparison is not straightforward due to the shoulder structure which may not be related to the CCFA density of states. The TMR changes its sign at 700±20 mV which is larger than the calculated 640±20 mV. An extrapolation of the experimental data excluding the shoulder provides values of ∼400 mV, which is again smaller than calculated.

It may be argued that, since there are certain indications of a Fe enrichment, the doping parameter X chosen for comparison must be higher than 0.4. However, in order to achieve a concordance between the measured and predicted voltages a X value near 0.7 should be taken. Such a strong iron enrichment appears as very improbable.

Thus, it is not possible to affirm that the origin of the negative TMR lays in the electronic structure of $Co_2Cr_{0.6}Fe_{0.4}Al$. Nevertheless, the DOS related explanation can not be completely discarded since the bulk calculations may not describe correctly the DOS at the interfaces.

On the other hand, alternative explanations are possible. Li *et al.* [143] extended the Slonczewski model [140] for high bias voltages. They modeled the DOS in the ferromagnets using the free-electron approximation, i.e. assuming that the two spin bands of the ferromagnet are parabolic. With additional inclusion of a trapezoidal shape for the barrier, they obtain a change in the sign of TMR at high voltages. Li *et al.* observed that the height of the barrier has a strong influence on the voltage at which the TMR sign change takes places. This voltages increases with the height of the barrier. This behavior seems to point out that the barrier properties, rather than the DOS of the electrodes, are dominating the TMR sign change. For this reason, just a rough qualitatively concordance between band structure calculations and experimental data is not a proof of the validity of the calculations or the interpretation of the experiment.

When a feature is observed in the spectroscopic measurements in a junction with dissimilar electrodes, it is always difficult to decide which material is responsible for it. In this sense it is interesting to observe the results for junctions consisting of Co as both top and bottom electrode.

Measurements of the dependence of the differential conductivity and of the TMR ratio on the bias voltage for $Co/Al_2O_3/Co$ tunneling junctions can be found in work published by LeClair *et al.* [144]. In this work, the effect of dusting Cu layers between the electrodes and the barrier is studied. Nevertheless, the

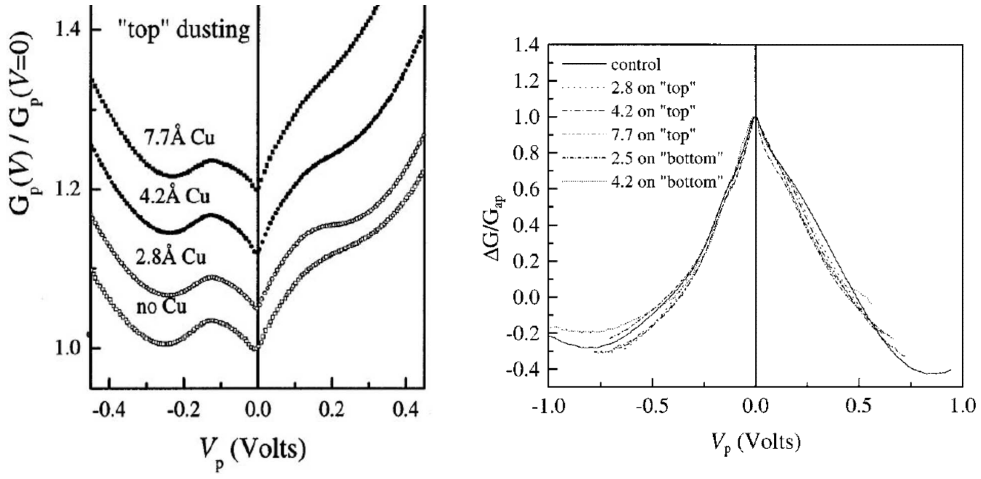

Figure 6.8: Measurements from [144] of the differential conductivity G=dI/dV (left) and of the TMR(V_{BIAS}) (right) for $Co/Al_2O_3/Co$ junctions with Cu dusting layers. The control Cu free junctions are also shown.

measurements are also shown for Co junctions without dusting. The results are reproduced in fig. 6.8. On the right panel the TMR(V_{BIAS}) curves are shown. A change of the sign of the TMR ratio is also recognized. The voltage at which this change takes places lays around 500 mV, which is comparable to the voltage at which the sign change is observed in our junctions. Due to this similarity, we can not conclude anymore that the CCFA electrode is responsible for the sign change of the TMR. The negative TMR could be understood as characteristic of the Co electrode or as a result of a more general barrier effect.

6.2.3 Additional structures

In this section the structure observed at ∼160 mV in the dI/dV measurements and the asymmetric shoulder in the TMR(V_{BIAS}) curves are discussed.

As mentioned before, both features appear concurrently in our junctions with epitaxial $Co_2Cr_{0.6}Fe_{0.4}Al$ electrodes with 2D RHEED patterns. But this behavior does not mean that both structures have the same origin. Let us refer again to the work of LeClair *et al.* [144]. The correspondent dI/dV(V_{BIAS}) and TMR(V_{BIAS}) for $Co/Al_2O_3/Co$ tunneling junctions are shown in fig. 6.8. The same structure is seen in the dI/dV measurements (fig. 6.8, left), indicating that the Co electrode is responsible for it. Note that the shoulder in the TMR(V_{BIAS}) is not present (fig. 6.8, right), indicating dissimilar origins for both phenomena.

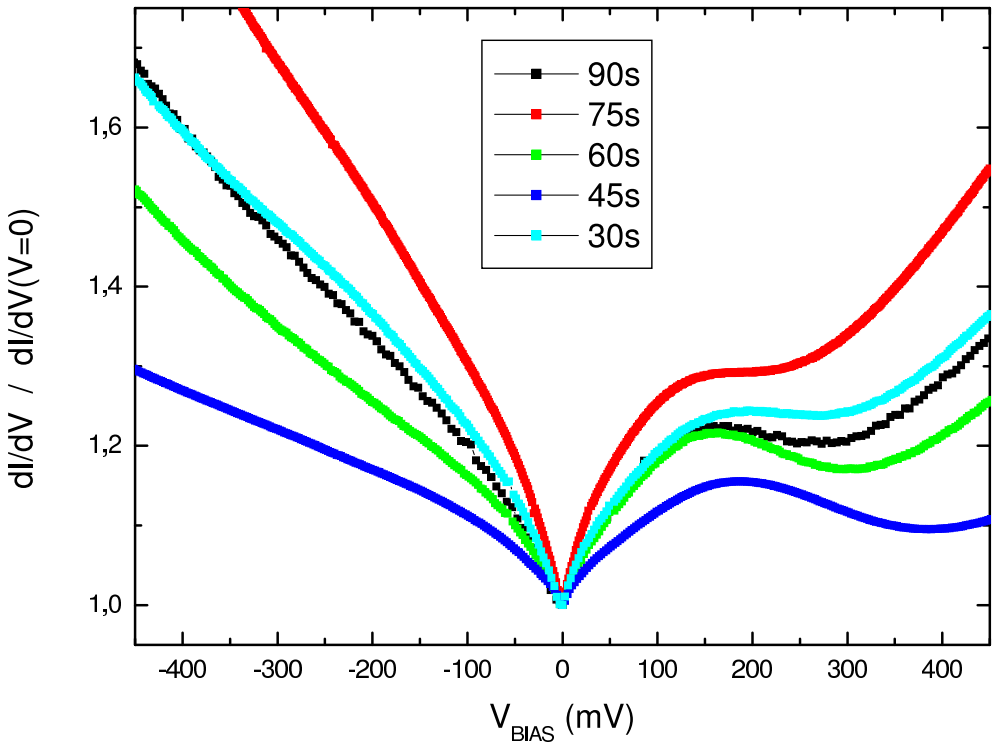

Figure 6.9: Differential conductivity (dI/dV) measurements for a sample series with varying oxidation times. The data is normalized to the value of dI/dV at zero bias. The $Co_2Cr_{0.6}Fe_{0.4}Al$ electrode was annealed at 550 °C for 5 min. The nominal barrier thickness is 3 nm and the oxidation took place in an Ar-O_2 mixture.

Structure in the dI/dV curves

Notwithstanding the Co origin, there is indeed a correlation between the surface characteristics of the $Co_2Cr_{0.6}Fe_{0.4}Al$ electrode and the structure at 160 mV in the dI/dV measurements since it is only observed in annealed samples with 2D RHEED patterns. This is not surprising, the different morphological and crystalline properties of the $Co_2Cr_{0.6}Fe_{0.4}Al$ surface may have an influence on the growth of the barrier and indirectly on the growth of the Co layer, modifying the Al_2O_3/Co interface electronic properties as well.

In a different paper from LeClair *et al.* [145], a comparison of the dI/dV curves for Co/Al_2O_3/Co between polycrystalline hcp and epitaxial fcc electrodes is shown. Again, the structure at 150 mV is seen, but only in junctions with epitaxial electrodes. In polycrystalline samples the structure disappears. This is different to our samples since we see the structure though the Co electrodes are polycrystalline. We assume that the $Co_2Cr_{0.6}Fe_{0.4}Al$ surface properties influences

only the first Co layers near to the barrier and they are responsible for the feature. Again, this shows how sensitive is tunneling to the interfaces properties.

With the duration of the oxidation process, the interfaces are also modified, specially the CCFA/Al_2O_3 one. Therefore, a change in the structure with the oxidation time is expected. In fig. 6.9, the dI/dV(V_{BIAS}) curves for annealed junctions with different oxidation times are plotted. In order to allow comparisons, the curves are normalized to the value of the conductivity at zero bias. Though certain differences are seen from sample to sample, no systematic behavior is recognizable. Nevertheless, the presence of the zero bias anomaly and the parabolic background, which changes also strongly with the oxidation conditions, does not allow a completely independent study of the feature at 150 mV.

Shoulder in the TMR (V_{BIAS}) curves

Concerning the shoulder in the TMR(V_{BIAS}) curves, this feature is not present in the Co/Al_2O_3/Co junctions. Therefore, it may be possible that in this case the CCFA electrode is responsible. At this point it should be remembered that the shoulder is situated at the positive bias region, i.e. it is associated with electrons tunneling into Co. In fig. 6.7 the estimated spin polarisation from band structure calculations of G. Fecher [142] is plotted. The cases for Fe doping concentration X=0.25 (top) and X=0.5 (bottom) are shown. $Co_2Cr_{0.6}Fe_{0.4}Al$ lies between this two cases with X=0.4.

The half-metallic gap is clearly visible in the calculations for both compounds. At higher voltages the gap closes and the spin polarisation drops. At this point is when a shoulder is recognizable in the occupied states polarisation. This shoulder is indicated by the arrows in fig. 6.10. The width of the shoulder changes with the Fe content. This structure is situated at the same energies than the shoulder in the TMR(V_{BIAS}) curve. In contrast to the negative TMR values or to the structure in the dI/dV curves, no alternative explanation could be found. Thus, this shoulder may indeed be a feature generated by the DOS of CCFA.

However, before a certain identification is possible, it would be helpful if calculations including the effect of the B2 disorder were available.

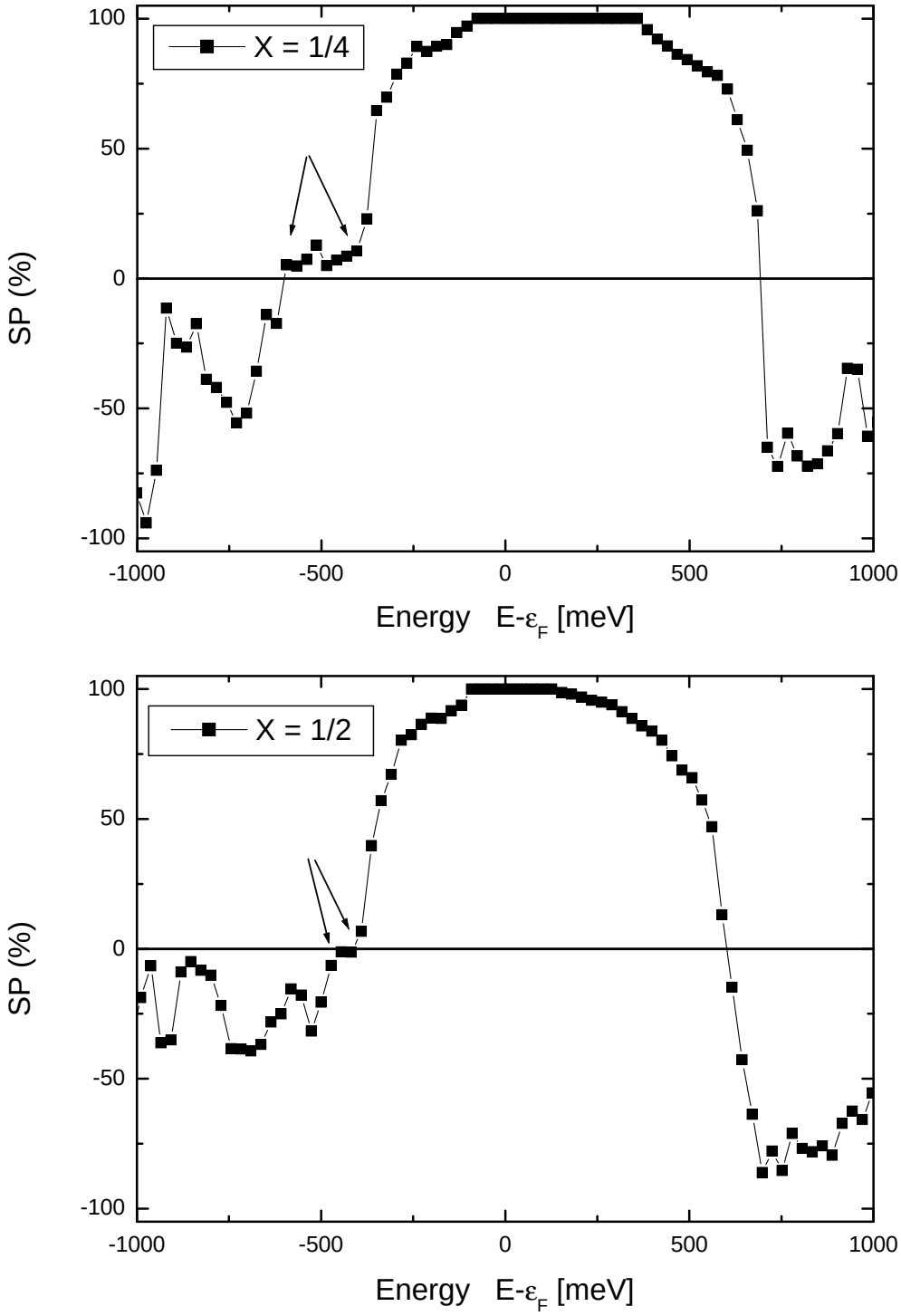

Figure 6.10: Estimated spin polarisation for $Co_2Cr_{1-x}Fe_xAl$ for the cases X=1/2 and X=1/4 from calculations by Fecher [142]. The arrows indicate the structure which is tentatively postulated as origin of the shoulder in the TMR(V_{BIAS}) curves.

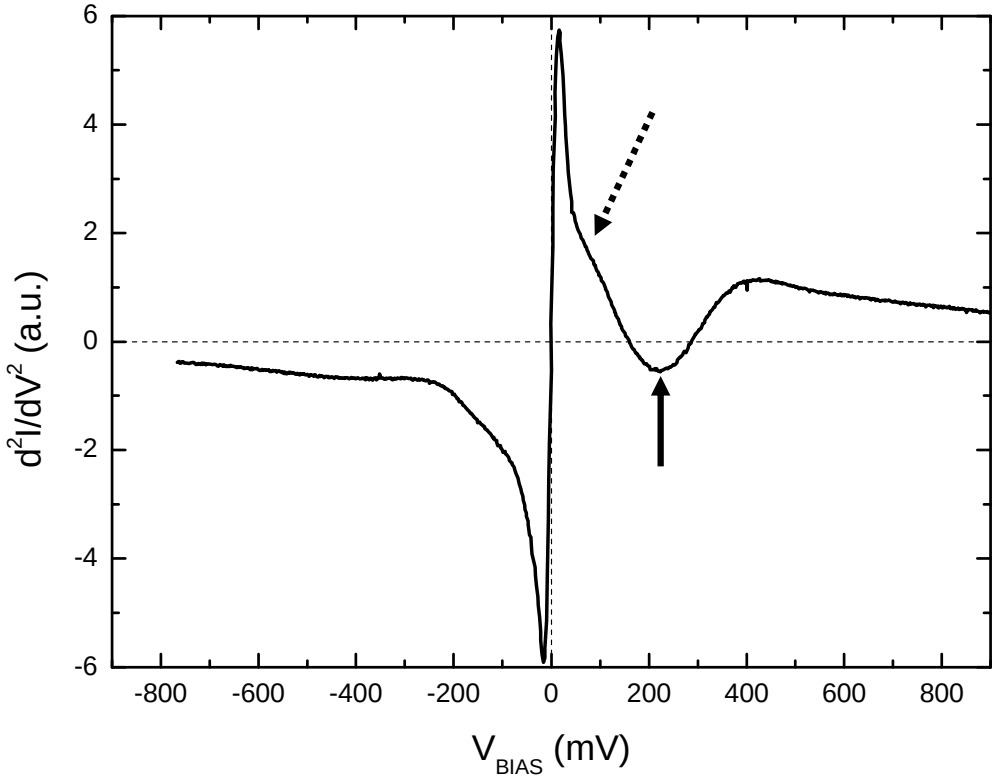

Figure 6.11: IET spectra measured at 4 K for a $Fe/Co_2Cr_{0.6}Fe_{0.4}Al/Al_2O_3/Co$ junction. The $Co_2Cr_{0.6}Fe_{0.4}Al$ electrode was annealed at 550 °C for 5 min. The nominal barrier thickness is 3 nm and the oxidation took place in an Ar-O_2 mixture. The sharp peaks at 16 mV are due to inelastic electron-magnon scattering processes during the tunneling process. The structure at ∼220 mV (solid arrow) is related to the Co counter electrode feature observed in the dI/dV measurements. An additional overlapping structure (dashed arrow) is also observed.

6.3 IET measurements

The measurement of the d^2I/dV^2 (V_{BIAS}) curve, also called inelastic electron tunneling (IET) spectrum in the literature, provides additional information regarding processes occurring at the interfaces FM/barrier. More precisely, as the name indicates, the IET spectra contain information about inelastic scattering processes implicating electron-phonon or electron-magnon interactions. Pioneering analysis of IET spectra in MTJ's were performed by Moodera *et al.* in $Co/Al_2O_3/NiFe$ junctions [23, 137].

Equivalently to the differential conductivity, two methods can be used to determine the d^2I/dV^2 (V_{BIAS}) curves. A differentiation of the dI/dV curves or a direct measurement. The first method has the advantage that no additional

measurement is needed. However, the last method results in spectra with reduced experimental noise. In this work, both methods were used.

Equation 6.1 shows that the measurement of the amplitude of the second harmonic with a frequency 2ω is directly proportional to d^2I/dV^2.

In fig. 6.11 an IET spectrum measured at 4 K is shown. This spectrum corresponds to a junction with a $Co_2Cr_{0.6}Fe_{0.4}Al$ electrode deposited on a Fe buffer layer and annealed at 550 °C for 5 min. The nominal barrier thickness is 3 nm. The TMR ratio for this junction is 40.2%. Two large sharp peaks are observed symmetrically around zero bias at a voltage ≈16 mV. An additional wide structure, indicated by the solid arrow, is observed at ∼220 mV. Furthermore, the sharp peaks at small voltages show a shoulder (dashed arrow) indicating an additional overlapping structure.

The sharp peaks at low voltages are related with the zero bias anomaly and have been attributed to inelastic magnon scattering [23, 46, 137, 134, 146] The theoretical description of magnons introduces a wavelength cutoff to avoid a divergence in the magnonic density of states at low energies [133]. This cutoff energy has a physical justification. It represents anisotropy effects and finite coherence length due to grain boundaries. There is additionally a maximal magnon energy E_M which is related with the Curie temperature of the ferromagnet and the spin S of the localized d electrons $E_M = 3k_BT_C/(2S+1)$. This energy lies typically below 200 meV and explains why the zero bias anomaly and the sharp peaks in the IET spectra appear at lower voltages.

Nevertheless, as pointed out by Schmalhorst *et al.* [46] or Han *et al.* [147], the position of the sharp peaks is not identical to the gap in the magnonic density of states but to the energy with maximum probability for magnon excitations E_{MP}. Some authors reported a change in the position of these peaks from the parallel to the antiparallel configuration [147]. Following their interpretation, this change is related to an asymmetry of E_{MP} with respect to the magnetic configuration of the junction. In their opinion, also the wavelength cutoff should change. However, other authors did not observe any asymmetry [46].

In fig. 6.12 (top), a comparison of the IET spectra for the parallel and antiparallel configurations of the same junction as shown in fig. 6.11 is presented. In both cases the peaks are situated at the same voltage. On the other hand, the wide structure situated at ∼220 mV is slightly weaker for the antiparallel configuration. We believe that this structure is related to the wide feature observed in the $dI/dV(V_{BIAS})$ curves, see fig. 6.4 and therefore is related to the Co counter

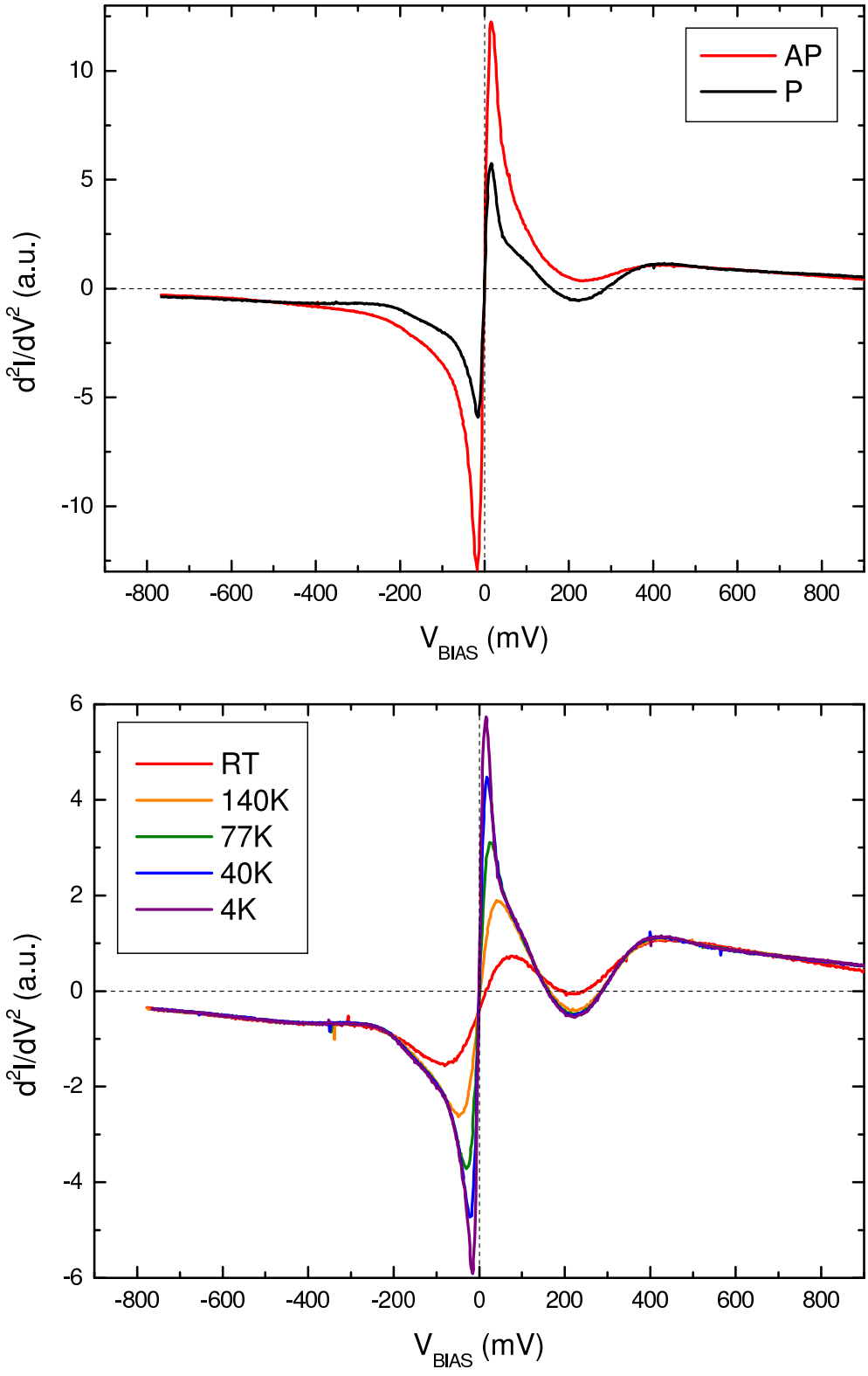

Figure 6.12: Top: Comparison of the IET spectra for the parallel and the antiparallel magnetization configuration. Bottom: IET spectra for the same junction measured at different temperatures. The broadening and the voltage shift of the peaks at low voltages are due to thermal smearing and to an increase of the low energy wavelength cutoff for magnons with increasing temperature. The structure at ∼220 mV is only modified by thermal smearing. For comparison, the different curves are normalized to the value at +500 mV. The nominal barrier thickness is 3 nm.

electrode.

The bottom panel in fig. 6.12 shows the IET spectra for the same junction measured at different temperatures for the parallel configuration. All the structures becomes less pronounced with increasing temperature. However, there are certain differences between the behavior of the peaks at low voltages and the feature at 220 mV. In the latter case, only a reduction of the height is observed, with no change in the width or voltage. On the contrary, the height change of the peaks at low voltages is accompanied by a shift to higher energies with increasing temperature and a widening of the peak. This behavior was attributed to thermal smearing and to an increase of the low energy wavelength cutoff for magnons with increasing temperature [133, 148].

The identification of the overlapping structure indicated by the dashed arrow in fig. 6.11 is also possible. Since the large magnon peaks at 16 mV are symmetric respect to V_{BIAS}=0, the subtraction of the negative bias side from the positive eliminates their contribution. In this way, the overlapping peak is visible. The results of this procedure for different temperatures is plotted in fig. 6.13. In order to be able to compare the curves, they have been normalized to the value at +500 mV. The curves are also displaced along the Y-axis for clarity.

A peak around 83 mV is observed. The peak intensity reduces with increasing temperature and it is almost lost at room temperature. Han *et al.* [146] studied the IET spectra for $Al_{1-x}Co_x/Al_{1-x}Co_x$-oxide/Al junctions and observed a peak with a x-dependent energy. This peak is identified as a phonon since it is still visible for x=0, i.e. $Al/Al_2O_3/Al$ junctions. The phonon peak for large Co concentrations (x=0.75) is situated at 84 mV and corresponds to an Al-O-Co strechting mode. This peak is slightly asymmetric with respect to the bias voltage and it is situated at 75 mV for the opposite voltage sign. We believe that the peak observed in our spectra has the same origin.

Due to this origin, changes of the interfaces properties by changing the oxidation conditions may influence its position. Unfortunately, only dI/dV data sets are available for samples series with different oxidation times. The differentiation of this data to obtain the IET spectrum result in an increased noise in comparison with a direct measurement. This is problematic in order to observe the behavior of the phonon structure at 85 mV since additionally a subtraction is needed.

Fig. 6.14 shows the subtraction of the negative bias voltage side from the positive bias voltage side of the IET spectra for junctions with different oxidation times. The nominal thickness of the barrier of all these samples is 2 nm. Please

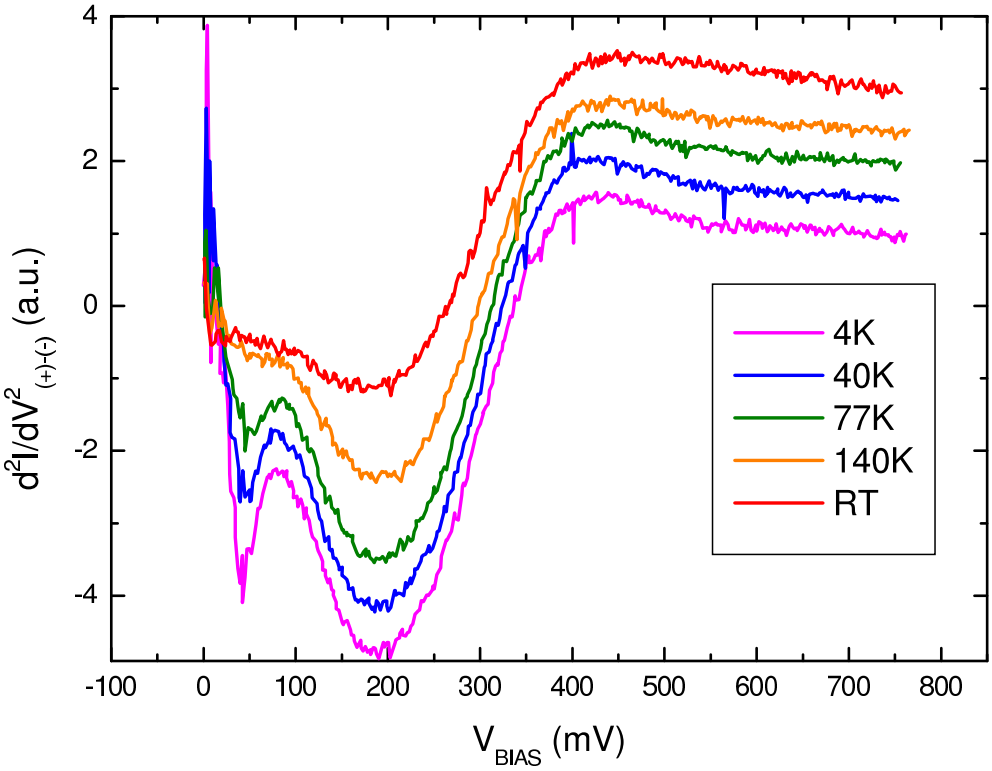

Figure 6.13: Subtraction of the negative bias voltage side from the positive bias voltage side of the IET spectra for different temperatures. The overlapping structure observed in the IET spectra (fig. 6.11) is now visible as a peak centered at ∼85 mV. This peak is tentatively identified as a phonon generated at the interface barrier/electrode (see text for explanation). The $Co_2Cr_{0.6}Fe_{0.4}Al$ electrode was annealed at 550 °C for 5 min. The nominal barrier thickness is 3 nm. The TMR ratio for this sample is 40.2%.

note that the barrier thickness for this series is different to the samples presented up to now in this section. This makes these samples more vulnerable to overoxidation. The behavior of the TMR ratio for this kind of samples was shown in fig. 5.9.

Though the increased noise level, a certain tendency is recognized. The phonon peak is situated at ∼85 mV for oxidation times of 30 and 45 s, this is the same position as in fig. 6.13. This position is marked with a dashed line. With increasing oxidation time the peak shifts to lower voltages, 75 mV for 60 s and roughly 70 mV for 75 s. For oxidation times of 90 s, the peak is extremely weak and its position can not be determined.

An interesting fact should be pointed out. As shown in fig. 5.9, for small oxidation times the TMR ratio approximates to 40% and falls with increasing

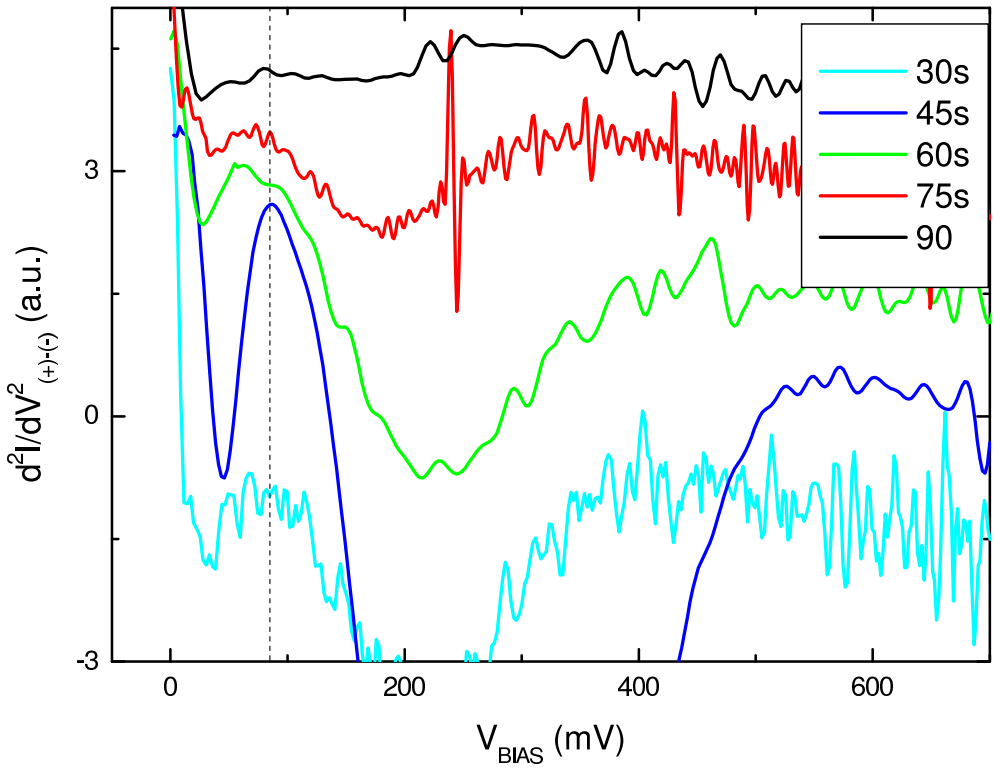

Figure 6.14: Difference of the negative bias voltage side from the positive bias voltage side of the IET spectra at 4 K for samples with different oxidation times. The dashed line is a guide to the eye and indicates $V_{BIAS} = 85$ mV. The increased noise level is a consequence of the non-direct measurement of d^2I/dV^2. The peak position shifts slightly toward lower voltages with increasing oxidation times. For oxidation times of 90 s this tendency can not be confirmed due to the small size of the peak. The $Co_2Cr_{0.6}Fe_{0.4}Al$ electrode was annealed at 550 °C for 5 min. The nominal barrier thickness is 2 nm.

oxidation time. When the TMR ratio approaches the same values as for samples with 3 nm barrier thickness, the phonon peak approaches also the same position. This can be an indication that under these conditions the interfaces of both kind of samples are similar.

As a conclusion, although there are difficulties concerning the interpretation of the IET measurements, important information about the interfaces can be gained from them. In future a more systematic study of these spectra should be done. In particular, information about the magnon properties (magnonic gap and E_{MP}) of the CCFA/barrier interface can be gained by the measurement of IET spectra of CCFA/Al_2O_3/Al junctions. In this way, the interference of the Co electrode is eliminated.

Summary

The present thesis studies the crystalline and magnetic properties of thin films of the theoretically predicted half metal $Co_2Cr_{0.6}Fe_{0.4}Al$. The films were implemented in magnetic tunneling junctions (MTJ's) and the tunneling magnetoresistance effect (TMR) was investigated. A maximal spin polarisation of 54% at 4 K was measured in tunneling junctions with epitaxial $Co_2Cr_{0.6}Fe_{0.4}Al$ electrodes and a correlation between crystalline properties, surface ordering and TMR ratios was found.

Epitaxial thin films of the alloy $Co_2Cr_{0.6}Fe_{0.4}Al$ with two alternative growth orientations were deposited. Metallic Cr and Fe buffer layers were used to induce (100)-oriented epitaxial growth at low temperatures (100 °C) on MgO(100) substrates. An annealing step at temperatures above 500 °C is used to improve the crystalline properties of the thin films. Alternatively, epitaxial thin films were obtained on $MgAl_2O_4$ (100) and Al_2O_3 $(11\bar{2}0)$ substrates without buffer layers. In this case an annealing step is needed to generate crystalline order. On Al_2O_3 substrates (110) orientation is achieved.

The films possess the B2 structure, i.e. considering the Heusler structure the Cr-Fe and Al positions are completely mixed. Band structure calculations show that this type of disorder is not detrimental to the spin polarisation.

The film surfaces are smooth as proved by *in situ* STM imaging which makes them suitable to deposit an insulating barrier for tunneling experiments. Since tunneling is very sensitive to the barrier/electrode interfaces, the existence of crystalline order at the film surfaces is of crucial importance. For samples deposited on buffers layers, surface crystalline order is higher for annealed films as observed by RHEED. In the case of samples deposited without buffer layer, no RHEED reflections are observed for as deposited films. In this case, the annealing step is needed to induce crystalline order at the surface.

The $Co_2Cr_{0.6}Fe_{0.4}Al$ films were used as bottom electrodes of MTJ's. Co was used as counter electrode and Al_2O_3 was chosen as barrier material. The use of

an amorphous barrier allows the applicability of the Jullière model. The junctions were exchange-biased with CoO. The deposited MTJ stacks were patterned lithographically in MESA structures.

A maximum TMR value of 41% was measured. From this value, a Jullière spin polarisation of 54% at 4 K is determined for $Co_2Cr_{0.6}Fe_{0.4}Al$. This value is similar to the 52% measured by Inomata *et al.* [95] in tunneling experiments. At 77 K the spin polarisation amounts to 48%. Investigating our films by spin resolved photoemission, Cinchetti *et al.* measured a spin polarisation of 45% at room temperature [117].

A strong dependence of the TMR values on the annealing temperature of the bottom $Co_2Cr_{0.6}Fe_{0.4}Al$ electrode was found. For annealing temperatures over 500 °C, an abrupt increase of the TMR ratio is observed reaching a maximum at 550 °C. Further increase of the annealing temperature results in a drop of the TMR ratio.

The increase of the TMR ratio with the annealing temperature could be correlated with an improvement of the surface properties as observed by RHEED. However, the drop of the TMR at higher annealing temperatures could not be correlated with RHEED. An STM study ruled out the possibility of an increased roughness to explain the decrease. X-ray absorption spectroscopy (XAS) provides evidence for a possible Fe enrichment of the $Co_2Cr_{0.6}Fe_{0.4}Al$ electrode due to annealing. This effect could be a result of interdiffusion from the Fe buffer layer used in these experiments.

A surface tailoring experiment was performed to prove the hypothesis of the Fe enrichment as reason for the TMR decrease at annealing temperatures above 550 °C. Very thin Cr layers (1-5 Å) were deposited on top of the $Co_2Cr_{0.6}Fe_{0.4}Al$ electrode before annealing. The results seems to support the hypothesis of a Fe enrichment. Independent of the conclusions of this study, surface tailoring experiments open a wide range of possibilities to modify the properties of the interfaces and eventually increase the TMR values.

Spectroscopic measurements were performed on the MTJ's presented in the present work. Structures in the dI/dV (V_{BIAS}) curves are attributed to electron-magnon scattering at the interfaces and to effects of the Co counter electrode. On the other hand, an asymmetric shoulder observed in the TMR (V_{BIAS}) curves is tentatively correlated with band structure calculations. Additionally, a sign change of the TMR is observed at voltages ∼500 mV.

With the measurement of inelastic electron tunneling (IET) spectra, informa-

tion about processes occurring at the interfaces electrode/barrier can be gained. The measurements in our junctions show sharp peaks at low voltages (16 mV) attributed mainly to electron-magnon inelastic scattering. An additional peak at 85 mV is tentatively attributed to an Al-O-Co phonon stretching mode.

Within this work, reliable experimental techniques to produce epitaxial CCFA thin films and to implement them in MTJ's were developed resulting in reproducible results. In the future, other electrode combinations with different counter electrodes should be investigated. Ferromagnetic counter electrodes with higher spin polarisation than Co should be used to increase the size of the TMR effect. Al electrodes could be used to measure IET spectra. In this way, the contribution of the Co electrode is eliminated and information about the magnonic density of states in $Co_2Cr_{0.6}Fe_{0.4}Al$ can be obtained. Additionally, with Al in the superconducting regime (Meservey-Tedrow junctions), an alternative way to estimate the spin polarisation is available. Concerning the exchange bias properties, FeMn could substitute CoO allowing the measurement of TMR ratio at increased temperatures.

Appendix A

A.1 Patterning of CCFA/AlO_X/Co/CoO/Pt mesa structures

Steps in *italic* are not strictly necessary, but highly recommendable to achieve high reproducibility and defect-free structures.

1. *Sample cleaning on the spinner, with isopropanol for 15 s at 300 rpm and then 15 s at 4000 rpm for drying. This will remove particles from silver clue and dust that may be on the film.*

2. Cover with positive photoresist ma-P 1215 (micro resist technology GmbH), drop on at 300 rpm 10 s and then 30 s at 3000 rpm.

3. 90 s on the hot plate at 100 °C .

4. 40 s UV exposure, mesa mask in contact.

5. Develop with maD-331, drop on without rotation and wait 45 s. Rinse with water for 15 s, 300 rpm and then 15 s, 4000 rpm for drying.

6. Ion etching for 16 min for a 50 nm thick counter electrode, rotating the sample (15-20 rpm) tilted 70^0 with respect to incident beam.

7. Sample cleaning with aceton in a ultrasonic bath, 1 min. The presence of particles must be checked with the microscope. If necessary repeat this step until the sample is free of particles.

8. *After cleaning in the ultrasonic bath, wash the sample with acetone on the spinner for 15 s, 300 rpm and then dry for 15 s, 4000 rpm.*

9. Cover with photoresist SU-8-2002. Then spin 5 s at 500 rpm (acceleration factor 9) and 30 s at 3000 rpm.

10. Softbake of the resist on the hot plate. The sample must be heated up to 95 °C in 8 min. Hold for 1.5 min and then take it from the plate and let it cool down.

11. 40 s UV exposure, window mask in contact.

12. Post-exposure bake on the hot plate. The sample must be heated up to 95 °C in 6 min. Hold for 1 min and then take it from the plate and let it cool down.

13. Develop with XPSU-8, 75 s. Rinse with isopropanol, 15 s, 300 rpm and dry for 15 s at 4000 rpm.

A.2 Sputtering and oxidation parameters

For magnetron sputtering, the configuration of the magnetic fields around the target has an influence on the deposition rate. This configuration depends on the thickness of the target and if the target is composed of several peaces or not. During this work, several different $Co_2Cr_{0.6}Fe_{0.4}Al$ targets were used and the deposition rate varied from one to the other. I present here the parameters for the last target ($\sim$3 mm thick, one piece).

Except for Al, the deposition rate was measured by the determination of the film thickness by x-ray reflectometry for several samples. This was not possible for Al because no Laue oscillations were observed. For this metall, an AFM was used to measure the step height at the edge of scratches on several thin films. Additionally, results from steps patterned by litography were consistents with the scratch methode.

For $Co_2Cr_{0.6}Fe_{0.4}Al$:	$p_{Ar} = 1.5^{-2}$ mbar
	I = 50 mA
	V$\approx$310 V
	Dep. rate = 28 nm/min
For Al:	$p_{Ar} = 2.0{\cdot}10^{-2}$ mbar
	I = 20 mA
	V$\approx$235 V
	Dep. rate = 4 nm/min
For Co:	$p_{Ar} = 1.8{\cdot}10^{-2}$ mbar
	I = 25 mA
	V$\approx$230 V
	Dep. rate = 3.6 nm/min
For Pt:	$p_{Ar} = 2.0{\cdot}10^{-2}$ mbar
	I = 40 mA
	V$\approx$? V
	Dep. rate = 22 nm/min

For oxidation with pure oxygen $P_{O_2} = 0.2$ mbar is used, for mixture Ar-O_2, the chamber is filled with Ar until $P_{Ar} = 0.1$ mbar and then with oxygen until

reaching 0.2 mbar. The current in the oxidation cathode is 10 mA. The voltage is over 500 V. During the operation the voltage is not stable and slowly drifts towards higher values.

Bibliography

[1] R. A. de Groot, F. M. Mueller, P. G. Engen and K. H. Buschow, *Phys. Rev. Lett.*, Vol. **50**, 2024, (1983).

[2] K. Schwarz, *J.Phys. F: Met. Phys.*, Vol. **16**, L211, (1986).

[3] K. Kobayashi, T. Kimura, H. Sawada, K. Terakura, and Y. Tokura, *Nature*, Vol. **395**, 677, (1998).

[4] M. Jullière, *Phys. Lett.*, Vol. **54A**, 225-226, (1975).

[5] V. Heine, *Phys. Review*, Vol. **138**, A1689, (1965).

[6] Ph. Mavropoulos, N. Papanikolaou and P. H. Dederichs, *Phys. Rev. Lett.*, Vol. **85**, 1088, (2000).

[7] P. H. Dederichs, Ph. Mavropoulos, O. Wunnicke, N. Papanikolaou, V. Bellini, R. Zeller, V. Drchal and J. Kudrnovský, *J. Magn. Magn. Materials*, Vol. **240**, 108, (2002).

[8] J. M. MacLaren, X.-G. Zahng, W. H. Butler and X. Wang,*Phys. Rev. B*, Vol. **59**, 5470, (1999).

[9] J. Mathon and A. Umerski, *Phys. Rev. B*, Vol. **63**, 220403, (2001).

[10] E. Yu. Tsymbal and D. G. Pettifor, *Phys. Rev. B*, Vol. **58**, 4323, (1998).

[11] S. Yuasa, T. Nagahama, A. Fukushima, Y. Suzuki, and K. Ando, *Nat. Mater.*, Vol. **3**, 868, (2004).

[12] S. Yuasa, A. Fukushima, T. Nagahama, K. Ando, and Y. Suzuki, *Jpn. J. Appl. Phys.*, Part 2 Vol. **43-4B**, L588, (2004).

[13] S. S. P. Parkin, C. Kaiser, A. Panchula, P. M. Rice, B. Hughes, M. Samant and S. Yang *Nat. Mater.*, Vol. **3**, 862, (2004).

[14] D. D. Djayaprawira, K. Tsunekawa, M. Nagai, H. Maehara, S. Yamagata, N. Watanabe, S. Yuasa, Y. Suzuki, and K. Ando, *Appl. Phys. Lett.*, Vol. **86**, 092502, (2005).

[15] T. Marukame, T. Ishikawa, S. Hakamata, K.-i. Matsuda, T. Uemura and Masafumi Yamamoto, *Appl. Phys. Lett.*, Vol. **90**, 012508, (2007).

[16] M. Yamamoto, T. Marukame, T. Ishikawa, K. Matsuda, T. Uemura and M. Arita, *J. Phys. D: Appl. Phys.*, Vol. **39**, 824, (2006).

[17] O. Wunnicke, Ph. Mavropoulos, R. Zeller, and P. H. Dederichs, *Phys. Rev. B*, Vol. **65**, 241306, (2002).

[18] P. M. Tedrow and R. Meservey, *Solid State Commun.*, Vol. **16**, 71, (1975).

[19] J. S. Moodera, M. E. Taylor and R. Meservey, *Phys. Rev. B*, Vol. **40**, 11980, (1989).

[20] J. J. Sun and P. P. Freitas, *J. Appl. Phys.*, Vol. **85**, 5264, (1999).

[21] P. LeClair, H. J. M. Swagten, J. T. Kohlhepp, R. J. M. van de Veerdonk and W. J. M. de Jonge, *Phys. Rev. Lett.*, Vol. **84**, 2933, (2000).

[22] J. A. Appelbaum and W. F. Brinkman, *Phys. Rev. B*, Vol. **2**, 907, (1970).

[23] J. S. Moodera, T. H. Kim, C. Tanaka and C. H. De Groot, *Phil. Mag. B*, Vol. **80**, 195, (2000).

[24] J. G. Simmons,, *J. Appl. Phys.*, Vol. **34**, 238, (1963).

[25] W. F. Brinkman, R. C. Dynes and J. M. Rowell, *J. Appl. Phys.*, Vol. **41**, 1915, (1970).

[26] See J. M. Rowell in *Tunneling phenomena in solids*, Chapter. **27**, edited by E. Burstein and S. Lundqvist, Plenum Press, New York, (1969).

[27] Z. G. Zhang, Z. Z. Zhang and P. P. Freitas, *J. Appl. Phys.*, Vol. **93**, 8552, (2003).

[28] K. Moon, Y. Chen and Y. Huai, *J. Appl. Phys.*, Vol. **91**, 7965, (2002).

[29] K. Kobayashi and H. Akimoto, *Fujitsu Sci.Tech. J.*, Vol. **42**, 139, (2006).

[30] For the press release of Samsung see:
http://www.samsung.com/Products/HardDiskDrive/news/
/HardDiskDrive_20050801_0000197917.htm
About Toshiba:
http://news.zdnet.com/2100-9584_22-6079664.html
Article of Sining Mao from Seagate at Solid State Technology:
http://sst.pennnet.com/articles/article_display.cfm?article_id=211234

[31] T. M. Maffitt, J. K. DeBrosse, J. A. Gabric, E. T. Gow, M. C. Lamorey, J. S. Parenteau, D. R. Willmott, M. A. Wood and W. J. Gallagher, *IBM J. Res. & Dev.*, Vol. **50**, No. 1, 25, (2006).

[32] J. Åkerman, *Science*, Vol. **308**, 508, (2005)

[33] Y. M. Huai, D Apalkov, Z. T. Diao, Y. F. Ding, A Panchula, M. Pakala, L. C. Wang and E. Chen, *Jpn. J. Appl. Phys.*, Vol. **45**, 5A, 3835, (2006).

[34] Y. M. Huai, M. Pakala, Z. T. Diao and Y. F. Ding, *IEEE Trans. Mag.*, Vol. **41**, (10), 2621, (2005).

[35] H. Meng, J. P. Wang, *IEEE Trans. Mag.*, Vol. **41**, (10), 2612, (2005).

[36] W. J. Gallagher and S. S. P. Parkin, *IBM J. Res. & Dev.*, Vol. **50**, No. 1, 5, (2006).

[37] Press release of Toshiba and NEC Corporation:
http://www.nec.co.jp/press/en/0602/0702.html

[38] Y. Zheng, Y. Wu, K. Li, J. Qiu, G. Han, Z. Guo,P. Luo, L. An, Z. Liu, L. Wang, S. Tan, B. Zong, B. Liu, *J. Nanoscience and Nanotech.*, Vol. **7**, (1), 117, (2007).

[39] Press release of Freescale Semiconductors:
http://media.freescale.com/phoenix.zhtml?c=196520&p=irol-newsArticle
&ID=880030

[40] A. Ney, C. Pampuch, R. Koch and K. H. Ploog, *Nature*, Vol. **425**, 485, (2003).

[41] W. C. Black and Bodhisattva Das, *J. Appl. Phys.*, Vol. **87**, 6674, (2000).

[42] J. Schotter, P. B. Kamp, A. Becker, A. Phler, D. Brinkmann, W. Schepper, H. Brückl and G. Reiss,, *IEEE Trans. Magn.*, Vol. **38**, 3365, (2002).

[43] M. Oogane, Y. Sakuraba, J. Nakata, H. Kubota, Y. Ando, A. Sakuma and T. Miyazaki, *J. Phys. D: Appl. Phys.*, Vol. **39**, 834-841, (2006).

[44] Y. Sakuraba, J. Nakata, M. Oogane, H. Kubota, Y. Ando, A. Sakuma and T. Miyazaki, *Jpn. J. Appl. Phys.*, Vol. **44**, No. 35, L1100, (2005).

[45] S. Kämmerer, A. Thomas, A. Hütten and G. Reiss, *Appl. Phys. Lett.*, Vol. **85**, 79, (2004).

[46] J. Schmalhorst, S. Kämmerer, G. Reiss and A. Hütten, *Appl. Phys. Lett.*, Vol. **86**, 052501, (2005).

[47] N. Tezuka, N. Ikeda, A. Miyazaki, S. Sugimoto, M. Kikuchi and K. Inomata, *Appl. Phys. Lett.*, Vol. **89**, 112514, (2006).

[48] Z. Gercsi, A. Rajanikanth, Y. K. Takahashi, K. Honob, M. Kikuchi, N. Tezuka and K. Inomata, *Appl. Phys. Lett.*, Vol. **89**, 082512, (2006).

[49] N. Tezuka, S. Okamura, A. Miyazaki, M. Kikuchi and K. Inomata, *J. Appl. Phys.*, Vol. **99**, 08T314, (2006).

[50] C. T. Tanaka, J. Nowak and J. S. Moodera, *J. Appl. Phys.*, Vol. **81**, 5515, (1997).

[51] C. T. Tanaka, J. Nowak and J. S. Moodera, *J. Appl. Phys.*, Vol. **86**, 6239, (1999).

[52] Y. Sakuraba, M. Hattori, M. Oogane, Y. Ando, H. Kato, A. Sakuma, T. Miyazaki and H. Kubota, *Appl. Phys. Lett.*, Vol. **88**, 192508, (2006).

[53] I. Galanakis, Ph. Mavropoulos, and P. H. Dederichs, *J. Phys. D: Appl. Phys.*, Vol. **39**, 765-775, (2006).

[54] I. Galanakis, P. H. Dederichs and N. Papanikolaou *Phys. Rev. B*, Vol. **66**, 134428, (2002).

[55] M. Zhanga, Z. Liua, H. Hua, G. Liua, Y. Cuia, J. Chena, G. Wua, X. Zhangb and G. Xiao, *J. Magn. Magn. Materials*, Vol. **277**, 130, (2004).

[56] I. Galanakis, P. H. Dederichs and N. Papanikolaou, *Phys. Rev. B*, Vol. **66**, 174429, (2002).

[57] G. H. Fecher, H. C. Kandpal, S. Wurmehl, J. Morais, H. Lin, H.-J. Elmers, G. Schönhense and C. Felser, *J. Phys.: Condens. Matter*, Vol. **17**, 7237, (2005).

[58] C. Felser, B. Heitkamp, F. Kronast, D. Schmitz, S. Cramm, H. A. Dürr, H.-J. Elmers, G. H. Fecher, S. Wurmehl, T. Block, D. Valdaitsev, S. A. Nepijko, A. Gloskovskii, G. Jakob, G. Schönhense and W. Eberhardt, *J. Phys.: Condens. Matter*, Vol. **15**, 7019, (2003).

[59] K. H. J. Buschow and P. G. van Engen, *J. Magn. Magn. Materials*, Vol. **25**, 90, (1981).

[60] Y. Miura, K. Nagao and M. Shirai, *Phys. Rev. B*, Vol. **69**, 144413, (2004).

[61] T. Block, C. Felser, G. Jakob, J. Ensling, B. Mühling, P. Gütlich and R. J. Cava, *J. of Solid State Chem.*, Vol. **176**, 646, (2003).

[62] T. Block, S. Wurmehl,C. Felser and J. Windeln, *Appl. Phys. Lett.*, Vol. **88**, 202504, (2006).

[63] Ph. Mavropoulos, K. Sato, R. Zeller and P. H. Dederichs, *Phys. Rev. B*, Vol. **69**, 054424, (2004).

[64] Ph. Mavropoulos, I. Galanakis, V. Popescu and P. H. Dederichs, *J. Phys.: Condens. Matter*, Vol. **16**, S5759, (2004).

[65] M. Sargolzaei, M. Richter, K. Koepernik I. Opahle, H. Eschrig and I. Chaplygin, *Phys. Rev. B*, Vol. **74**, 224410, (2006).

[66] P. J. Brown, K. U. Neumann, P. J. Webster and K. R. A. Ziebeck, *J. Phys.: Condens. Matter*, Vol. **12**, 1827, (2000).

[67] S. Wurmehl, G. H. Fecher, K. Kroth, F. Kronast, H. A. Dürr, Y. Takeda, Y. Saitoh, K. Kobayashi, H.-J. Lin, G. Schönhense and C. Felser, *J. Phys. D: Appl. Phys.*, Vol. **39**, 803-815, (2006).

[68] I. Galanakis, *J. Phys.: Condens. Matter*, Vol. **14**, 6329, (2002).

[69] A. N. Caruso, C. N. Borca, D. Ristoiu, J. P. Nozieres, P. A. Dowben, *Surf. Science*, Vol. **525**, L109, (2003).

[70] D. Ristoiu, J. P. Nozieres, C. N. Borca, B. Borca, P. A. Dowben, *Appl. Phys. Lett.*, Vol. **76**, 2349, (2000).

[71] A. F. Panchula, C. Kaiser, A. Kellock, S. S. P. Parkin, *Appl. Phys. Lett.*, Vol. **83**, 1812, (2003).

[72] J. Schmalhorst, S. Kämmerer, M. Sacher, G. Reiss, A. Hütten and A. Scholl, *Phys. Rev. B*, Vol. **70**, 024426, (2004).

[73] P. Mavropoulos, M. Ležaić, and S. Blügel, *Phys. Rev. B*, Vol. **72**, 174428, (2005).

[74] R. Skomski and P. A. Dowben, *Europhys. Lett.*, Vol. **58**, (4), 544 (2002).

[75] M. Ležaić, Ph. Mavropoulos, J. Enkovaara, G. Bihlmayer, and S. Blügel, *Phys. Rev. Lett.*, Vol. **97**, 026404, (2006).

[76] P. A. Dowben and R. Skomski, *J. Appl. Phys.*, Vol. **93**, 7948, (2003).

[77] Ch. Hordequin, E. Lelièvre-Berna, J. Pierre, *Physica B*, Vol. **234-236**, 602, (1997).

[78] C. N. Borca, T. Komesu, H.-K. Jeong, and P. A. Dowben, *Phys. Rev. B*, Vol. **64**, 052409, (2001).

[79] M. P. Delplancke-Ogletree, M. Ye, R. Winand, J. F. Marneffe and R. Deltour, *J. Mat. Research*, Vol. **14**, (5) 2133, (1999).

[80] J. Du, S. Gnanarajan and A. Bendavid, *Supercond. Sci. Technol.*, Vol. **18**, 1035, (2005).

[81] M. Murugesan, H. Obara, Y. Nakagawa, S. Kosaka and H. Yamasaki, *Supercond. Sci. Technol.*, Vol. **17**, 113, (2004).

[82] J. Nogués, I. K. Schuller, *J. Magn. Magn. Materials*, Vol. **192**, 203, (1999).

[83] J. C. S. Kools, *IEEE Trans. Magn.*, Vol. **32**,(4), 3165, (1996).

[84] R. Jungblut, R. Coehoorn, M. T. Johnson, J. aan de Stegge and A. Reinders, *J. Appl. Phys.*, Vol. **75**, 6659, (1994).

[85] C. Tsang, N. Heiman and Kenneth Lee, *J. Appl. Phys.*, Vol. **52**, 2471, (1981).

[86] G. Jakob, F. Casper, V. Beaumont, S. Falk, N. Auth, H.-J. Elmers, C. Felser and H. Adrian, *J. Magn. Magn. Materials*, Vol. **290-291**, 1104, (2005).

[87] D. B. Williams and C. B. Carter in *Transmission electron microscopy*, Plenum Press, New York, (1996).

[88] A. Garulli, A. Armigliato and M. Vanzi, *J. Microsc. Spectrosc. Electron.*, Vol. **10**,(2), 135, (1985).

[89] T. Block, C. Felser, G. Jakob, J. Ensling, B. Mühling, P. Gütlich and R. J. Cava, *J. Sol. Stat. Chem*, Vol. **176**,(2), 646, (2003).

[90] *Pearson's handbook of crystallographic data for intermetallic phases*, ASM International, (1996).

[91] Description and download of the program PowderCell in the web page of the *Bundesanstalt für Materialforschung und Prüfung Berlin*: http://www.bam.de/de/service/publikationen/powder_cell.htm

[92] M. Yamamoto, T. Marukame, T. Ishikawa, K. Matsuda, T. Uemura and M. Arita, *J. Phys. D: Appl. Phys.*, Vol. **39**, 824-833, (2006).

[93] K.-i. Matsuda, T. Kasahara, T. Marukame, T. Uemura, M. Yamamoto, *J. Crys. Growth*, Vol. **286**, 389, (2006).

[94] R. Kelekar, B. M. Clemens, *J. Appl. Phys.*, Vol. **96**, 540, (2004).

[95] K. Inomata, S. Okamura, A. Miyazaki, M. Kikuchi, N. Tezuka, M. Wojcik and E. Jedryka, *J. Phys. D: Appl. Phys.*, Vol. **39**, 816-823, (2006).

[96] *X-Ray diffraction in crystals, imperfect crystals and amorphous bodies*, Dover Publications, New York, (1994).

[97] H. Schneider, G. Jakob, M. Kallmayer, H.-J. Elmers, M. Cinchetti, B. Balke, S. Wurmehl, C. Felser, *Phys. Rev. B*, Vol. **74**, 174426, (2006).

[98] M. A. Butler, G. K. Wertheim and D. N. Buchanan, *Phys. Rev. B*, Vol. **5**, 990, (1972).

[99] U. Köbler, A. Hoser, J. Englich, A. Snezhko, M. Kawakami, M. Beyss and K. Fischer, *J. Phys. Soc. Japan*, Vol. **70**, 3089, (2001).

[100] D. Pan and D. Turnbull, *J. Appl. Phys.*, Vol. **45**, 1406, (1974).

[101] C. L. Chien and R. Hasegawa, *Phys. Rev. B*, Vol. **16**, 2115, (1977).

[102] J. D. Axe, G. Shirane, T. Mizoguchi and K. Yamauchi, *Phys. Rev. B*, Vol. **15**, 2763, (1977).

[103] U. Köbler, *J. Phys.: Condens. Matter*, Vol. **14**, 8861, (2002).

[104] A. Scherz, H. Wende and K. Baberschke, *Appl. Phys. A*, Vol. **78**, 843, (2004).

[105] M. Kallmayer, A. Conca, M. Jourdan, H. Schneider, G. Jakob, B. Balke, A. Gloskovskii and H.-J. Elmers, *J. Phys. D: Appl. Phys.*, Vol. **40**, 1539, (2007).

[106] M. Kallmayer, H. Schneider, G. Jakob, H.-J. Elmers, K. Kroth, H. C. Kandpal, U. Stumm and S. Cramm, *Appl. Phys. Lett.*, Vol. **88**, 072506, (2006).

[107] H.-J. Elmers, G. H. Fecher, D. Valdaitsev, S. A. Nepijko, A. Gloskovskii, G. Jakob and G. Schönhense, *Phys. Rev. B*, Vol. **67**, 104412, (2003).

[108] L. J. van der Pauw, *Philips. Res. Repts.*, Vol. **13**, 1-9, (1958).

[109] H. Schneider, Ch. Herbort, G. Jakob, H. Adrian, S. Wurmehl and C. Felser, *J. Phys. D: Appl. Phys.*, Vol. **40**, 1548, (2007).

[110] B. Raquet, M. Viret, E. Sondergard, O. Cespedes and R. Mamy, *Phys. Rev. B*, Vol. **66**, 024433, (2002).

[111] Z. M. Ziman, *Electrons and phonons*, Clarendon Press, (1963).

[112] W. Braun, *Applied RHEED*, Springer-Verlag Berlin Heidelberg, (1999) and references therein.

[113] P. J. Estrup, *Surf. Science*, Vol. **25**, 1, (1971).

[114] A. Conca, S. Falk, G. Jakob, M. Jourdan and H. Adrian, *J. Mag. Mag. Mat.*, Vol. **290-291**, 1127, (2005).

[115] R. J. M. van de Veerdonk, J. Nowak, R. Meservey, J. S. Moodera and W. J. M. de Jonge, *Appl. Phys. Lett.*, Vol. **71**, 2839, (1997).

[116] J. S. Moodera, L. R. Kinder, J. Nowak, P. LeClair and R. Meservey, *Appl. Phys. Lett.*, Vol. **69**, 708, (1996).

[117] M. Cinchetti, J-P Wüstenberg, M. Sánchez Albaneda, F. Steeb, A. Conca, M. Jourdan and M. Aeschlimann *J. Phys. D: Appl. Phys.*, Vol. **40**, 1544, (2007).

[118] N. Auth, G. Jakob, T. Block and C. Felser, *Phys. Rev. B*, Vol. **68**, 024403, (2003).

[119] S. V. Karthik, A. Rajanikanth, Y. K. Takahashi, T. Okhubo and K. Honoa, *Appl. Phys. Lett.*, Vol. **89**, 052505, (2006).

[120] Private communications.

[121] C. Shang, Y. C. Chen and K. Moon, *J. Appl. Physics*, Vol. **93**, 7017, (2003).

[122] B. Oliver, Q. He X. Tang and J. Nowak, *J. Appl. Physics*, Vol. **91**, 4348, (2002).

[123] R. H. French, *J. Am. Ceram. Soc.*, Vol. **73**,(3), 477, (1990).

[124] A. Ortiz, J. C. Alonso, V. Pankov, A. Huanosta, E. Andrade, *Thin Sol. Films*, Vol. **368**, 74, (2000).

[125] J. S. Moodera, L R. Kinder, T M. Wong and R. Meservey, *Phys. Rev. Lett.*, Vol. **74**, 3273, (1995).

[126] S. Yuasa, T. Sato, E. Tamura, Y. Suzuki, H. Yamamori, K. Ando and T. Katayama, *Europhys. Lett.*, Vol. **52**, 344, (2000).

[127] H. Boeve, E. Girgis, J. Schelten, J. De Boeck and G. Borghs, *Appl. Phys. Lett.*, Vol. **76**, 1048, (2000).

[128] A. Hütten, S. Kämmerer, J. Schmalhorst, A. Thomas, and G. Reiss, *Phys. Stat. Sol.*, Vol. **201**, (15) 3271, (2004).

[129] A. Thomas, D. Meyners, D. Ebke, N.-N. Liu, M. D. Sacher, J. Schmalhorst, G. Reiss, H. Ebert and A. Hütten, *Appl. Phys. Lett.*, Vol. **89**, 012502, (2006).

[130] P. LeClair, H. J. M. Swagten, J. T. Kohlhepp and W. J. M de Jonge, *Appl. Phys. Lett.*, Vol. **76**, 3783, (2000).

[131] J. A Appelbaum, *Phys. Rev.*, Vol. **154**, 633, (1967).

[132] L. Scheng, D. Y. Xing and D. N. Scheng, *Phys. Rev. B*, Vol. **70**, 094416, (2004).

[133] S. Zhang, P. M.Levy, A. C. Marley and S. S. P. Parkin, *Phys. Rev. Lett.*, Vol. **79**, 3744, (1997).

[134] C. Lü, M. W. Wu and X. F. Han, *Phys. Lett. A*, Vol. **319**, 205, (2003).

[135] J. Murai, Y. Ando, T. Daibou, K. Yaoita, H. F. Han and T. Miyazaki, *J. Mag. Mag. Mat.*, Vol. **226-230**, 922, (2001).

[136] J. Schmalhorst, S. Kämmerer, G. Reiss and A. Hütten, *Appl. Phys. Lett.*, Vol. **86**, 052501, (2005).

[137] J. S. Moodera, J. Nowak and R. J. M. van der Veerdonk, *Phys. Rev. Lett.*, Vol. **80**, 2941, (1998).

[138] D. C. Tsui, R. E. Dietz and L. R. Walker, *Phys. Rev. Lett.*, Vol. **27**, 1729, (1971).

[139] A. H. Davis and J. M. McLaren, *J. Appl. Phys.*, Vol. **87**, 5224, (2000).

[140] J. C. Slonczewski, *Phys. Rev. B*, Vol. **39**, 6995, (1989).

[141] C. H. Shang, J. Nowak, R. Jansen and J. S. Moodera, *Phys. Rev. B*, Vol. **58**, R2917, (1998).

[142] Private communications.
H. M. Kandpal, G. H. Fecher and C. Felser *J. Phys. D: Appl. Phys.*, Vol. **40**, 1507, (2007).

[143] F. Li, Z. Li, M. Xiao, J. Du, W. Xu, and A. Hu, *Phys. Rev. B*, Vol. **69**, 054410, (2004).

[144] P. LeClair, H. J. M. Swagten, J. T. Kohlhepp and W. J. M. de Jonge, *Appl. Phys. Lett.*, Vol. **76**, 3783, (2000).

[145] P. LeClair, J. T. Kohlpepp, C. H. van de Vin, H. Wieldraaijer, H. J. M. Swagten, W. J. M. de Jonge, A. H. Davis, J. M. MacLaren, J. S. Moodera and R. Jansen, *Phys. Rev. Lett.*, Vol. **88**, 107201, (2002).

[146] X-F. Han, J. Murai, Y. Ando, H. Kubota and T. Miyazaki, *Appl. Phys. Lett.*, Vol. **78**, 2533, (2001).

[147] X-F. Han, A. C. C. Yu, M. Oogane, J. Murai, T. Daibou and T. Miyazaki, *Phys. Rev. B*, Vol. **63**, 224404, (2001).

[148] J. R. Kirtley and D. J. Scalapino, *Phys. Rev. Lett.*, Vol. **65**, 798, (1990).